Gain and Loss Factor for Conical Horns, and Impact of Ground Plane Edge Diffractions on Radiation Patterns of Uncoated and Coated Circular Aperture Antennas

by

Nafati Abdasallam Aboserwal

A Dissertation Presented in Partial Fulfillment
of the Requirements for the Degree
Doctor of Philosophy

Approved October 2014 by the
Graduate Supervisory Committee:

Constantine A. Balanis, Chair
James T. Aberle
George Pan
Cihan Tepedelenlioglu

ARIZONA STATE UNIVERSITY

December 2014

ABSTRACT

Horn antennas have been used for over a hundred years. They have a wide variety of uses where they are a basic and popular microwave antenna for many practical applications, such as feed elements for communication reflector dishes on satellite or point-to-point relay antennas. They are also widely utilized as gain standards for calibration and gain measurement of other antennas.

The gain and loss factor of conical horns are revisited in this dissertation based on spherical and quadratic aperture phase distributions. The gain is compared with published classical data in an attempt to confirm their validity and accuracy and to determine whether they were derived based on spherical or quadratic aperture phase distributions. In this work, it is demonstrated that the gain of a conical horn antenna obtained by using a spherical phase distribution is in close agreement with published classical data. Moreover, more accurate expressions for the loss factor, to account for amplitude and phase tapers over the horn aperture, are derived. New formulas for the design of optimum gain conical horns, based on the more accurate spherical aperture phase distribution, are derived.

To better understand the impact of edge diffractions on aperture antenna performance, an extensive investigation of the edge diffractions impact is undertaken in this dissertation for commercial aperture antennas. The impact of finite uncoated and coated PEC ground plane edge diffractions on the amplitude patterns in the principal planes of circular apertures is intensively examined. Similarly, aperture edge diffractions of aperture antennas without ground planes are examined. Computational results obtained by the analytical model are compared with experimental and HFSS-simulated results for all cases studied.

In addition, the impact of the ground plane size, coating thickness, and relative permittivity of the dielectric layer on the radiation amplitude in the back region has been examined.

This investigation indicates that the edge diffractions do impact the main forward lobe pattern, especially in the E plane. Their most significant contribution appears in far side and back lobes. This work demonstrates that the finite edge contributors must be considered to obtain more accurate amplitude patterns of aperture antennas.

To My Great Grandparents Fatma and Maatog

for being my first teacher

To My Loving Parents Noria and Abdasallam

all I have and will accomplish are only possible due to their love and sacrifices

To My Lovely Wife Marwa

for her love, endless support and encouragement

To My Soul and My Life Taha and Salam

And to all those who supported me throughout these years

ACKNOWLEDGEMENTS

I am thankful to Allah Almighty, the Most Beneficent the Most Merciful, Who's Blessings have always given me strength and wisdom.

First and firstmost, I would like to express my sincere appreciation to my adviser Prof. Constantine Balanis for his excellent guidance and encouragement, support, valuable suggestions, and continuous inspiration. It has been my pleasure to be his student and work with him throughout my graduate study and research at the Arizona State University. His great assistance in manuscript preparation is deeply acknowledged. This work would not been possible without him. You are an admirable example for my academic career!

I also would like to thank to my committee members Prof. James Aberle, Prof. George Pan, and Prof. Cihan Tepedelenlioglu for their helpful comments and suggestions and constructive criticism. Special thanks to Mr. Craig Birtcher for his careful and timely reading of drafts and assistance in obtaining the experimental results.

I would like to express my appreciation to all of my labmates, Ahmet Durgun, Victor Kononov, Alix Rivera-Albino, Saud Alsaeed, Mikal Amiri, Wengang Chen, Sivaseetharaman Pandi, and Kaiyue Zhang, present and past, who I have worked with over the past four years.

I would like to thank my grandparents and parents for all the guidance and support they have provided throughout my life. It was their continues encouragement and motivation which kept me moving towards my goal. Thank you to my siblings for all your endless support. Especial thanks to my uncle Omran and his family for their supporting.

To my beloved wife Marwa, I express my heartfelt thanks and deepest gratitude for her patience, love, and understanding. My son Taha and my daughter Salam, who born during my study, were a source of happiness and enjoyment. You are the wind beneath my wings.

TABLE OF CONTENTS

LIST OF TABLES

LIST OF FIGURES

Figure Page

Figure Page

Figure Page

Figure Page

CHAPTER 1

INTRODUCTION

For conical horn antennas, the radiation characteristics (amplitude patterns, gain, loss factor) strongly depend on the amplitude and phase distributions of the field over the horn aperture. The reduction in gain due to the amplitude and phase tapers across the horn aperture is represented by the aperture efficiency, which is the product of the taper efficiency and phase efficiency. The taper efficiency represents the uniformity of the amplitude distribution of the field over the horn aperture, while the phase efficiency represents the phase uniformity of the field over the horn aperture. The main work in this dissertation concentrates on the impact of the amplitude and phase distributions of the field over the horn aperture on the gain of the antenna and its amplitude patterns.

Gain is one of the most important figure-of-merit of a conical horn antenna. It is well established that the gain of a conical horn is strongly affected by the phase distributions of the field over the horn aperture. The phase distribution can be modeled by tracing the path trajectories the waves follow from a virtual apex, near the junction of the waveguide-to-the-horn transition, to the horn aperture. The difference between this length and that from the virtual apex to the aperture center is the *path length term* [1].

Unfortunately, the gain of conical horn antennas, despite their popularity and wide range of applications, has not received the same attention compared to other antennas, especially the pyramidal horn. Gray and Schelkunoff [2] developed a set of classic curves on the gain of conical horns, which are included in the literature [1], [3]. While these results have been used as a reference in many books and papers, it has not been clearly documented how they were obtained. Also, it is not obvious whether the reported graphs were derived based on spherical or quadratic aperture phase distributions. This issue is addressed in this dissertation and a direct calculation of gain and loss factor is conducted with exact and approximate expressions for the path length terms.

In general, amplitude patterns of aperture antennas are influenced by aperture edge diffractions, or diffractions from the edges of (uncoated and coated) ground planes where they are mounted. In addition to investigating the effect of the aperture edge diffractions on the amplitude patterns of a conical horn without a ground plane, the impact of uncoated and coated ground plane edge diffractions on the amplitude patterns in the principal planes of commercial aperture antennas is also examined in this dissertation.

1.1. Objectives

In this dissertation, there are three main objectives. In the first objective, an improved analytical formulation for the radiation characteristics of conical horn antennas is introduced. A conical horn gain, employing TE_{11}-mode circular waveguide excitation, is calculated by using exact and approximate path length terms, then the gain is compared to that obtained by the modal solution which models the horn as a finite conical waveguide. In addition, expressions for more accurate loss factors, to account for amplitude and phase tapers over the conical horn aperture, are derived which improve the prediction of the conical horn gain. New formulas for the design of optimum gain conical horns, based on the more accurate spherical aperture phase distribution, are derived and reported, and guidelines are provided for their use.

For the second objective, the impact of finite PEC ground plane edge diffractions on the amplitude patterns of circular aperture antennas (conical horn and circular waveguide antennas) is investigated. To accomplish this task, a method is introduced to calculate accurately the far-zone amplitude patterns in the E and H planes, including those in the far side and back lobe regions, of an aperture antenna by applying Geometrical Optics (GO) and the Uniform Theory of Diffraction (UTD). The electric field distribution over the antenna aperture is obtained by a modal method (considering the aperture phase distribution of the conical horn antennas), and then it is employed to calculate the geometrical optics field using the aperture integration method assuming an infinite ground plane. The UTD is then applied to evaluate the diffraction from the ground plane edges. Far-zone amplitude patterns in the E and H planes are numerically obtained by the vectorial summation of the GO and UTD fields. Validity of the analysis is established by satisfactory agreement between the calculated and measured data and those simulated by HFSS. In addition, for a conical horn without a ground plane, the impact of the aperture's edge diffractions is investigated following the same procedure.

The third objective is to study the impact of finite coated ground plane edge diffractions on the amplitude patterns of circular aperture antennas. A model based upon the uniform theory of diffraction for an impedance wedge and the geometrical optics method is presented to calculate the amplitude patterns of a circular aperture antenna mounted on square and circular finite PEC ground planes that are coated with a lossy dielectric. The diffraction of electromagnetic waves for impedance wedges (half plane with two face impedances in our work) is investigated. The GO fields obtained by the spectral domain method and the diffracted fields for a dielectric-covered PEC ground plane are vectorially combined to determine far-zone amplitude patterns in the E and H planes. The model is validated by comparisons with experimental results and those simulated by HFSS.

1.2. Summary of the Chapters that Follow

The remainder of this document is organized as follows:

- *Chapter 2*: *Conical Horn Antenna: Gain, Loss Factor, and Optimum Design*. The first part of this chapter is devoted to a literature review of the conical horn antenna. Then, the phase distribution and the path length terms are investigated. After modeling the aperture fields of the conical horn, calculations of the gain and loss factor are conducted using the spherical and quadratic phase distributions over the horn aperture. Finally, expressions for more accurate loss factors, to account for amplitude and phase tapering over the conical horn aperture, are derived, and new formulas for the design of optimum gain conical horns, based on the more accurate spherical aperture phase distribution, are derived and reported.

- *Chapter 3*: *Uncoated Aperture Antennas*. This chapter deals with the impact of the PEC ground plane edge diffractions and the aperture edge diffractions on the amplitude patterns in the principal planes of the aperture antennas. A brief review of the geometrical optics method is presented. Then, the uniform theory of diffraction, to calculate the fields diffracted by the edges of the ground planes and aperture, is introduced. Lastly, the analytical results are validated by comparisons with measurements and HFSS simulations.

- *Chapter 4*: *Coated Aperture Antennas*. This chapter focuses on the diffraction by a wedge with different surface impedances. Because the aperture is covered with a dielectric layer, the impact of this layer is considered. The impact of the finite coated ground plane edge diffractions on the E- and H-plane amplitude patterns of the circular aperture antennas is investigated. Also, comparisons with measurements and HFSS simulations are provided. Moreover, the amplitude pattern level at $\theta = 180^\circ$ for different coating thickness, relative permittivity, and ground plane size has been examined in this chapter.

- *Chapter 5*: *Maliuzhinets Function and its Properties*. In this chapter, a literature review of the Maliuzhinets Function (MF) is presented. Then, an exact closed-form solution is obtained to evaluate a known integral representation of the MF. The $tanh - sinh\ quadrature$ rule is employed to successfully calculate the integral in the Maliuzhinets function, and the highly accurate numerical computation for MF is obtained over the entire complex z plane and for any wedge factor n, which defines the interior angle $[(2-n)\pi]$ of the wedge. Finally, for special wedge angles, the new formulation is numerically verified by comparing it with results obtained by numerical integration of the Maliuzhinets function.

- *Chapter 6*: *Conclusions and Recommendations*. All of the work presented in this study is summarized in this chapter. It also provides recommendations for future work.

CHAPTER 2

CONICAL HORN ANTENNA: GAIN, LOSS FACTOR, AND OPTIMUM DESIGN

2.1. Introduction

Aperture antennas, including horns, waveguides, slots, reflectors, and lenses, are most commonly used at microwave frequencies where they are used for radiating microwave signals into space and receiving microwave signals from space. These antennas work as a transition region between the free space and the guiding structure (waveguide). They are practical for space applications, where they can conveniently be flush mounted on the surface of the spacecraft or aircraft without affecting its aerodynamic profile, which is very critical in high-speed applications. They are also used as feed elements for large radio astronomy, communication dishes, and satellite tracking. Their openings are typically covered with a dielectric material to protect them from environmental conditions [1], [4]. Because of versatility, ease of excitation, high gain, and mechanical simplicity, aperture antennas have become one of the important microwave antennas.

As is well known, the end of a circular waveguide is essentially flared out to form a typical conical horn. This provides better matching in a broad frequency band where reflections are reduced. However, the flaring is more expensive and difficult to engineer. Aperture phase error, due to flaring, makes the uniform-phase aperture results invalid for the horn aperture. Therefore, the aperture phase error over the horn aperture needs to be involved in calculating the radiation characteristics of conical horn antennas.

To better understand the impact of aperture amplitude and phase tapers on the conical horn antenna performance, improved analytical formulations for the radiation characteristics of a conical horn are introduced. This analysis includes gain, aperture phase errors, loss factors for aperture amplitude and phase tapering, and amplitude patterns.

New expressions for the loss factor and the gain of conical horn antennas have been developed based on spherical aperture phase distributions. The gain of a conical horn antenna, using the spherical instead of the quadratic aperture phase distribution, is:

- Mainly the same for large axial length horns $(L > 60\lambda)$ or small peak aperture phase errors $(S < 0.4\lambda)$.
- Higher, by as much as 0.84 dB, for intermediate axial length horns $(10\lambda < L < 20\lambda)$ and intermediate peak aperture phase errors $(0.4\lambda < S < 0.9\lambda)$.
- Higher for large values of the peak aperture phase errors $(S > 0.9\lambda)$.

In addition, improved formulas for the design of optimum gain horn antennas are proposed. These formulas do not approximate the path length term. They provide more accurate horn designs for a given optimum gain, and they are highly useful for the design of conical horns.

2.2. Conical Horn Antenna

A conical horn is a truncated section of a right circular conical waveguide, and it is usually connected to a circular waveguide or a rectangular waveguide which is gradually transitioned into the circular waveguide [2]. Horns can be excited in any polarization or combination of polarization depending on dimensions of the feeding waveguide and the desired performance. It is a basic and popular microwave antenna for many practical applications because it provides high gain, low return loss, and wide bandwidth. Also, it is widely utilized as a gain standard for calibration and gain measurement [5].

The conical horn can be fed by a waveguide in mono- or multi-mode operation. Referring to the mode propagating within the wave guide feeding the horn, the conical horn is classified as a mono- or multi-mode horn. For the mono-mode horn, the dimensions of the feeding waveguide are sufficiently small so that only one mode (the dominant mode) propagates within the waveguide and then transits to the horn through the throat. The multi-mode horn is fed by a large dimension waveguide where more than one mode is allowed to propagate within the waveguide.

In the literature, a number of papers have addressed the E- and H-plane radiation characteristics, gain, and loss factors of sectoral and pyramidal horns [6-9]. It is well established that the radiation characteristics of a horn strongly depend on the amplitude and phase distributions over the horn aperture [1], [9]. The phase distribution can be modeled by tracing the path trajectories the waves follow from a virtual apex, near the junction of the waveguide-to-the-horn transition, to the horn aperture. The difference between this length and that from the virtual apex to the aperture center is the *path length term*. The exact and approximate path length terms were used to find the radiation characteristics for three horns (E- and H-plane sectoral, and pyramidal) [1], [9].

For the sectoral and pyramidal horns, closed form expressions, in terms of sine and cosine Fresnel integrals, for the radiation characteristics (amplitude patterns and gain) were obtained by using the quadratic phase term [1]. By introducing a spherical phase term (a more accurate term), instead of the quadratic phase term, the calculation of the gain of a pyramidal horn antenna was numerically obtained in [9]. It was concluded in [9] that the gain of the the pyramidal horn, using the spherical phase term instead of the quadratic, was:

- Basically the same for large apertures (A or $B > 50\lambda$) or small peak aperture phase errors (S or $T < 0.2\lambda$).
- Always higher for the intermediate aperture sizes ($5\lambda < A$ or $B < 8\lambda$) or intermediate peak aperture phase errors ($0.2\lambda < S$ or $T < 0.6\lambda$).
- Lower for large peak aperture phase errors (S or $T > 0.6\lambda$).

For the definitions of A, B, S, and T, refer to [9].

Unfortunately, the gain and amplitude patterns of the conical horn antenna, despite its popularity and wide range of applications, has not received the same attention compared to the others, especially the pyramidal horn. Gray and Schelkunoff developed a set of classic curves on the gain of a conical horn which were included in a figure in [2]. While these results have been used as a reference in many books and papers, it has not been clearly documented how they were obtained. Also, it is not obvious whether the reported graphs were derived based on spherical or quadratic phase distribution [1], [2]. This chapter addresses this issue. In addition, a direct calculation of the far-zone electric and magnetic field components, gain, and loss factors are calculated with exact and approximate expressions for the path length terms. In our calculation, the antennas are assumed to be lossless (no conduction or dielectric losses), and thus the directivity and gain are identical.

2.2.1. *Phase Distribution and Path Length Term*

Geometrically, it is illustrated that the phase distribution over the aperture of a horn is not uniform. Referring to Fig. 2.1, assume that at the imaginary apex of the horn there exists a source radiating spherical waves. The constant phase fronts are spherical as the waves travel toward the horn aperture. The phase over the aperture is different since the spherical waves travel different paths from the apex to the aperture. Referring to Fig. 2.1, the difference in the path of travel $\delta(\rho')$ can be written as

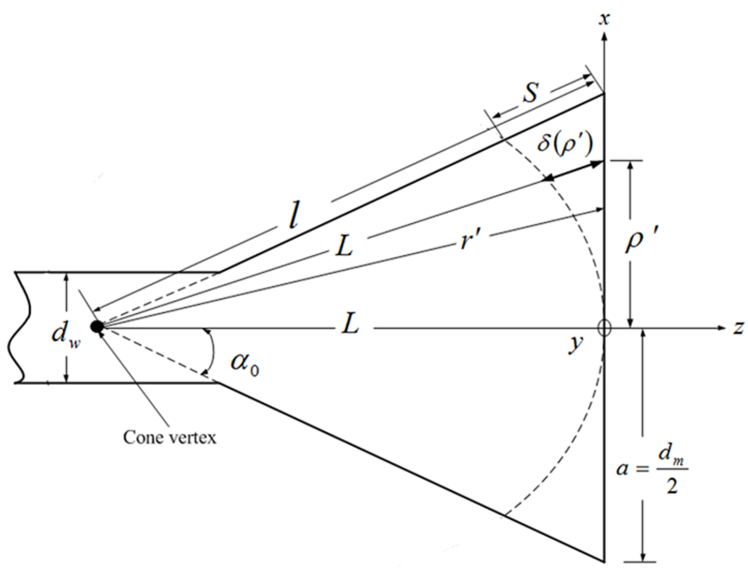

Fig. 2.1. Geometry for Determining Path Length Term [1], [5].

$$\delta(\rho') = -L + L\sqrt{1+\left(\frac{\rho'}{L}\right)^2} \tag{2.1}$$

which is referred to as *the spherical phase term*, which can be reduced to *the quadratic phase term* by using the binomial expansion and retaining only the first two terms; that is

$$\delta_a(\rho') \approx -L + L\left[1+0.5\left(\frac{\rho'}{L}\right)^2\right] = \frac{(\rho')^2}{2L} \tag{2.2}$$

The *peak* aperture phase error, denoted by S, is related to the path length term $\delta(\rho')$, at the edge of the aperture, by

$$S = \delta\left(\rho' = \frac{d_m}{2}\right) = -L + L\sqrt{1 + 0.25\left(\frac{d_m}{L}\right)^2} \tag{2.3}$$

an approximate value of it at the edge, based on (2.2), is

$$S_a = \delta_a\left(\rho' = \frac{d_m}{2}\right) = \frac{(d_m)^2}{8L} \tag{2.4}$$

The exact ϕ and the approximate ϕ_a phase lags (in degrees) are related, respectively, to the spherical and quadratic path length terms by

$$\phi = \frac{360}{\lambda}\ \delta(\rho') \tag{2.5}$$

$$\phi_a = \frac{360}{\lambda}\ \delta_a(\rho') \tag{2.6}$$

The exact peak phase lag at the edge of the aperture is

$$\phi_p = \frac{360}{\lambda}\ \delta(\rho')\Big|_{\rho' = \frac{d_m}{2}} \tag{2.7}$$

and its approximate value is

$$\phi_{ap} = \frac{360}{\lambda}\ \delta_a(\rho')\Big|_{\rho' = \frac{d_m}{2}} \tag{2.8}$$

The aperture phase difference due to the exact and approximate path lengths can be expressed as

$$\Delta\phi = \phi_a - \phi = \frac{360}{\lambda}\left[\delta_a(\rho') - \delta(\rho')\right] \tag{2.9}$$

Fig. 2.2 presents the aperture phase difference $\Delta\phi$ of (2.9) due to the binomial series approximation. The aperture phase difference $\Delta\phi$ is plotted versus the normalized aperture coordinate ρ'/d_m for different peak aperture phase errors S of (2.3) at the edge of the aperture. As shown, the aperture phase difference is decreasing when moving toward the aperture center and when the peak aperture phase error decreases. From Fig. 2.2, it can be seen that the maximum error due to the binomial series approximation is 32.90° for a peak aperture phase error of $S = 0.8\lambda$ and an aperture diameter of $d_m = 5\lambda$.

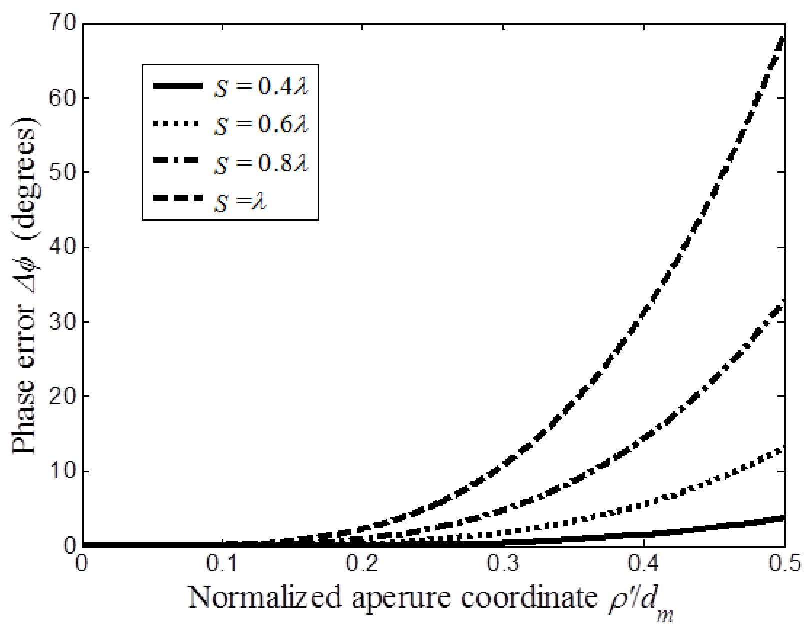

Fig. 2.2. Aperture Phase Error Due to Binomial Series Approximation $(d_m = 5\lambda)$.

The approximate peak aperture phase error S_a is always greater than or equal to the exact one, as illustrated in Fig. 2.3, and the difference increases as S_a increases for fixed aperture d_m. For example, when S_a increases from 0.8λ to 1.2λ for $d_m = 4\lambda$, Fig. 2.3 shows that the corresponding difference between S_a and S will increase from 0.1λ to 0.26λ. The relation between the exact (S) and approximate (S_a) expressions of the peak aperture

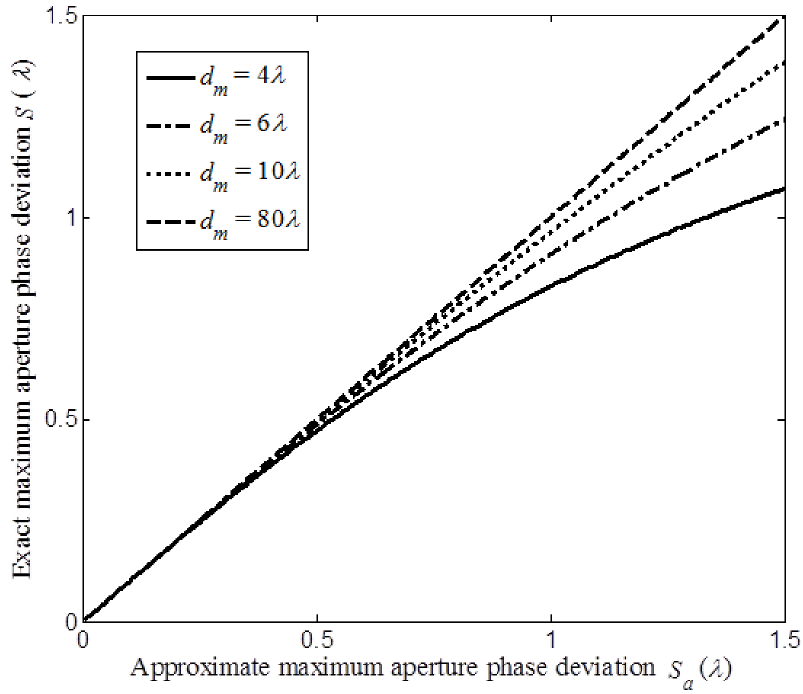

Fig. 2.3. Relationship of Approximate and Exact Peak Phase Deviation Parameters.

phase error of the same horn can be given by

$$S = (d_m)^2 \frac{1}{8S_a}\left(\sqrt{\left[1+\left(\frac{1}{d_m}\right)^2 16(S_a)^2\right]}-1\right) \tag{2.10}$$

The approximate peak aperture phase error is equal to the exact one for large apertures d_m, and nearly equal for small peak aperture phase errors $S < 0.4\lambda$. The data in Fig. 2.3 indicate that as the aperture size in wavelengths decreases, S_a increases for a given S.

2.2.2. *Conical Horn Aperture Fields*

The expressions of the fields over the aperture of the horn are similar to those of a TE_{11} mode for a circular waveguide with an aperture radius a. The only difference is the complex exponential term which represents the phase distributions (spherical or quadratic) over the horn aperture.

An analytical study on the radiation characteristics of a conical horn requires accurate amplitude and phase expressions for the fields over the horn aperture. For this purpose, one can use either the dominant TE_{11} mode of a circular waveguide or a modal solution based on a truncated conical waveguide.

The first approach, based on the TE_{11} mode, assumes that this mode continues to propagate within the horn in the form of a cylindrical Bessel function with a spherical or quadratic phase distribution, rather than a uniform plane wavefront along the symmetry axis. In this approximation, the fields behave as if they were generated by a point source at the virtual apex of the cone. Consider the conical horn which is connected to a cylindrical waveg-

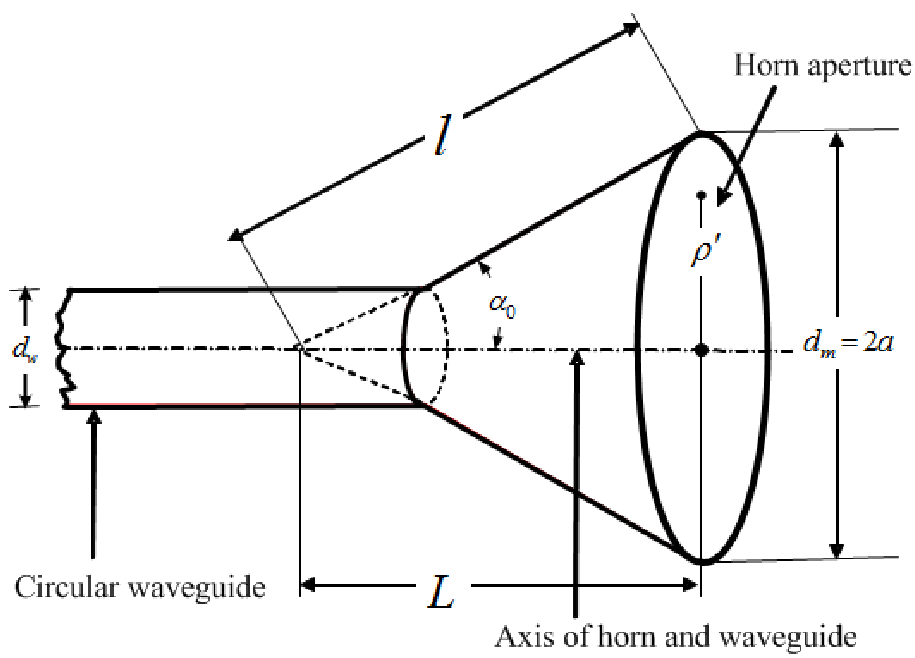

Fig. 2.4. Geometry of Conical Horn [4].

uide, as illustrated in Fig. 2.4, operating at the dominant TE_{11} mode. The electric field components over its aperture can be represented by

$$E_\rho = \frac{E_0}{\rho'} J_1\left(\chi'_{11}\frac{\rho'}{a}\right)\sin(\phi')\, e^{-jk\delta(\rho')} \quad \rho' \leq a \tag{2.11}$$

$$E_\phi = E_0\, J_1'\left(\chi'_{11}\frac{\rho'}{a}\right)\cos(\phi')\, e^{-jk\delta(\rho')} \quad \rho' \leq a \tag{2.12}$$

where $k = 2\pi/\lambda$, $\chi'_{11} = 1.8412$, E_0 is the normalized amplitude of incident electric field, $J_m(x)$ is the Bessel function of first kind of order m, $J_m'(x)$ is the first derivative of $J_m(x)$ with respect to the entire argument x, and the other primes (ρ', ϕ') indicate cylindrical coordinates of the equivalent excitation source over the antenna aperture. For the conical horn, there are two degrees of freedom that impact its performance: the axial length L, and the aperture diameter of the horn d_m. Some references may use the flare angle, which is related to L and d_m.

The second approach is based on the assumption that the conical horn can be treated as a conical waveguide whose field components are deduced from Maxwell's equations, using electric and magnetic vector potentials. It is possible to approximate the aperture field of a finite/truncated conical horn antenna from the fields within an infinite conical waveguide.

Consider the same conical horn, as illustrated in Fig. 2.4, operating at the dominant TE_{11} mode. Its aperture electric field components, using the modal solution of the conical waveguide [10], are represented by

$$E_\theta = \frac{E_0}{\sin(\theta')} J_1\left(\chi'_{11}\frac{\theta'}{\alpha_0}\right)\sin(\phi')\, \frac{H^{(2)}_{v+0.5}(kr')}{\sqrt{r'}} \tag{2.13}$$

$$E_\phi = E_0\frac{\chi'_{11}}{\alpha_0} J_1'\left(\chi_{11}\frac{\theta'}{\alpha_0}\right)\cos(\phi')\, \frac{H^{(2)}_{v+0.5}(kr')}{\sqrt{r'}} \tag{2.14}$$

where α_0 is the semi-flare angle of the cone; $H_m^{(2)}(x)$ is the Hankel function of second kind of order m; r', ϕ', θ' are the standard spherical coordinates with the origin at the vertex of the cone; v is the eigenvalue of the TE$_{11}$ mode inside the conical waveguide, or

$$v = -0.5 + \sqrt{0.25 + \left(\frac{\chi'_{11}}{\alpha_0}\right)^2} \tag{2.15}$$

Although the field components, in both approaches, have different mathematical expressions over the aperture, amplitude and phase distributions of these components are nearly the same, especially for small flare angles.

The fields radiated by the horn can be obtained by utilizing the field equivalence principle [11]. In this case, the conical horn is not mounted on a ground plane. Therefore, the electric and magnetic equivalent current densities ($\mathbf{J}_s$, $\mathbf{M}_s$) across the aperture have to be considered [1], [11]. Assuming the spherical aperture phase distribution, the total electromagnetic fields radiated by the horn aperture in the far-field region, due to electric and magnetic sources, are calculated by using the Aperture Integration method (AI), and they can be written as [1], [11]. These equivalent sources produce the same fields as the original sources in the region outside of the horn aperture.

$$E_\theta = j\frac{E_0 k_\rho k}{4r}\, e^{-jkr}\,(1+\cos\theta)\,\sin\phi\; L_\theta \tag{2.16}$$

$$E_\phi = j\frac{E_0 k_\rho k}{4r}\, e^{-jkr}\,(1+\cos\theta)\,\cos\phi\; L_\phi \tag{2.17}$$

where

$$L_\theta = \int_0^a \left[\rho' J_0\left(k_\rho \rho'\right) J_0\left(k\rho' \sin\theta\right) - \rho' J_2\left(k_\rho \rho'\right) J_2\left(k\rho' \sin\theta\right)\right] e^{-jk\delta(\rho')}\, d\rho' \tag{2.18}$$

$$L_{\phi}=\int_{0}^{a}\Big[\rho' J_0\left(k_{\rho}\rho'\right)J_0\left(k\rho'\sin\theta\right)+\rho' J_2\left(k_{\rho}\rho'\right)J_2\left(k\rho'\sin\theta\right)\Big]e^{-jk\delta(\rho')}\,d\rho' \tag{2.19}$$

$$k_{\rho}=\frac{\chi'_{11}}{a} \tag{2.20}$$

and $\delta(\rho')$ is presented by (2.1).

For the second approach, the similar procedure is followed by using the Aperture Integration method to find the far-zone radiated fields. The only differences are the terms related to the integration part where they are given by

$$L_{\theta}=\int_{0}^{a}\Big[\rho' J_0\left(k_{\rho}\rho'\right)J_0\left(k\rho'\sin\theta\right)-\rho' J_2\left(k_{\rho}\rho'\right)J_2\left(k\rho'\sin\theta\right)\Big]f(\rho')\,d\rho' \tag{2.21}$$

$$L_{\phi}=\int_{0}^{a}\Big[\rho' J_0\left(k_{\rho}\rho'\right)J_0\left(k\rho'\sin\theta\right)+\rho' J_2\left(k_{\rho}\rho'\right)J_2\left(k\rho'\sin\theta\right)\Big]f(\rho')\,d\rho' \tag{2.22}$$

where

$$f(\rho')=\frac{H^{(2)}_{\nu+0.5}\left(k\sqrt{L^2+(\rho')^2}\right)}{\sqrt{L^2+(\rho')^2}} \tag{2.23}$$

2.2.3. *Gain*

The conical horn gain, for a given length, increases with increasing flare angle until it reaches a maximum, beyond which it starts to decrease because of the large phase variations over the aperture. The maximum gain of a lossless horn can be calculated using

$$G=4\pi\,\frac{U_{max}}{P_{rad}} \tag{2.24}$$

where P_{rad} is the total radiated power calculated by simply integrating the average power density over the horn aperture A_a as follows

$$P_{rad}=\frac{1}{2}\iint\limits_{A_a}\mathrm{Re}\Big(\mathrm{E}'\times\mathrm{H}'^{*}\Big)\,d\rho' \tag{2.25}$$

$$P_{rad} = \frac{|E_0|^2 \pi}{2\eta} \int_0^a \left[\left(J_1 \left(k_\rho \rho' \right) \right)^2 / \rho' + \rho' \left(J_1' \left(k_\rho \rho' \right) \right)^2 \right] d\rho' \tag{2.26}$$

and U_{max} is the maximum radiation intensity directed along the z-axis ($\theta = 0°$). It is calculated using the far-zone electric field components of the horn antenna, and it is given by

$$U_{max} = U(\theta,\phi)\big|_{max} = \frac{r^2}{2\eta} \left|\mathrm{E}\right|^2_{max} = \frac{r^2}{2\eta} \left(\left|E_\theta\right|^2_{max} + \left|E_\phi\right|^2_{max} \right) \tag{2.27}$$

$$U_{max} = \frac{|E_0|^2 k^2 k_\rho^2}{8\eta} \left| \int_0^a \rho' J_0 \left(k_\rho \rho' \right) e^{-jk\delta(\rho')} \, d\rho' \right|^2 \tag{2.28}$$

Since the integrand in (2.18)-(2.22), (2.26), and (2.28) contains advanced functions, a closed-form analytical expression cannot be attained. Hence, Levin's integration algorithm [12-14] was used to find the far-zone E- and H-plane amplitude patterns, displayed, respectively, in Figs. 2.5 and 2.6, and gain which is shown in Fig. 2.7.

The data in these figures indicate that when the flare angle is small, the amplitude patterns in the E and H planes of a conical horn, obtained using the Spherical Phase Distributions (SPD), are in excellent agreement with the values calculated by using the Quadratic Phase Distributions (QPD) or the Modal Solution (MS). However, for large flare angles, the amplitude patterns in the E and H planes, obtained by using the spherical aperture phase distribution are not in good agreement with those calculated using the quadratic aperture phase distribution and the modal solution. In addition, it is shown that the amplitude patterns in the E and H planes of a conical horn antenna, by using the quadratic aperture phase distribution and the modal solution, are in better agreement. For the modal solution, it is possible to approximate the aperture field of a finite/truncated conical horn antenna from the field of an infinite conical waveguide. The wavefronts of the aperture fields of the

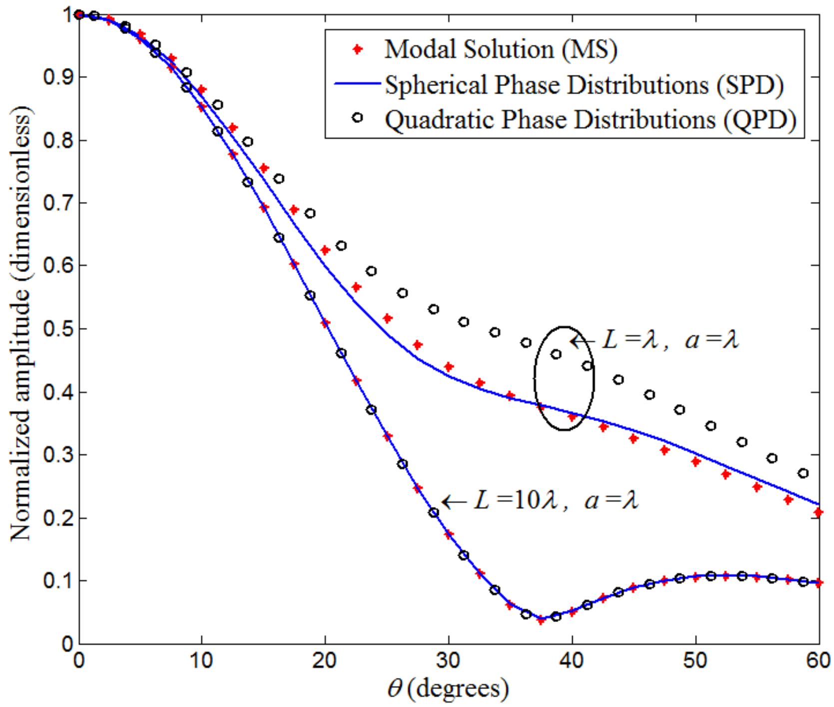

Fig. 2.5. Simulated Far-Zone E-Plane Amplitude Patterns of a Conical Horn Antenna by Using Spherical and Quadratic Aperture Phase Distributions, and Modal Solution.

infinite conical waveguide are nearly spherical. However, the fields have different wavefronts when the infinite conical waveguide is truncated. Although such wavefronts are not analytically separable at finite cone lengths, based on our calculations the truncated modal solution wavefronts are in better agreement with the quadratic instead of the spherical phase wavefronts.

Fig. 2.7 illustrates also that for a conical horn with a given axial length L, the gain increases as the aperture diameter d_m increases up to a certain optimum value. Beyond the optimum value, the gain begins to decrease because large phase variations at the aperture begin to occur. This follows the same trend exhibited for the pyramidal horn [1]. As indi-

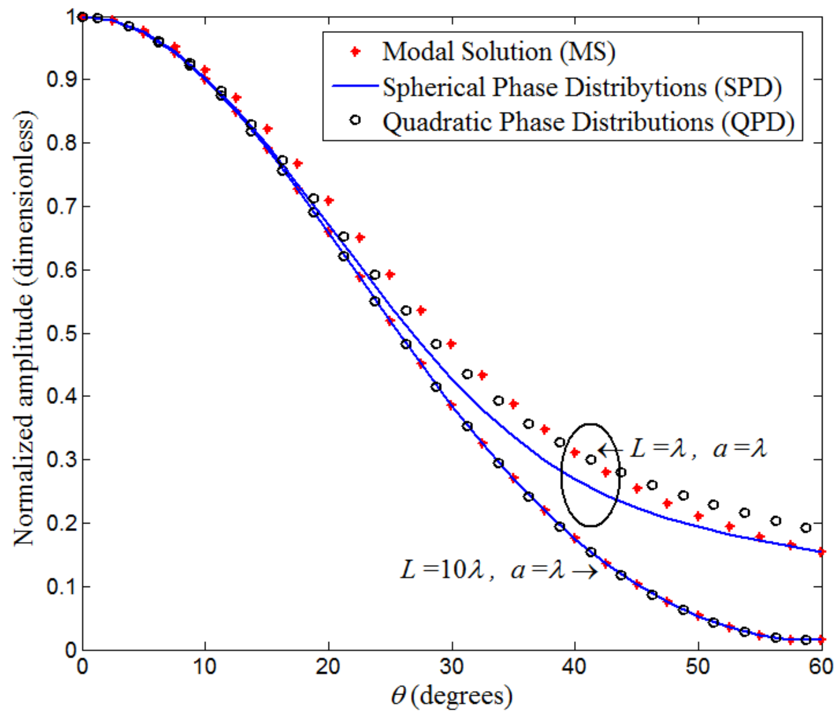

Fig. 2.6. Simulated Far-Zone H-Plane Amplitude Patterns of a Conical Horn Antenna by Using Spherical and Quadratic Aperture Phase Distributions, and Modal Solution.

cated in Fig. 2.7, the gain values obtained using the spherical aperture phase distribution are, as would have been expected and based also on the results of [9], in closer agreement with the Gray and Schelkunoff results than those obtained using the quadratic aperture phase distribution.

The computed gains, using spherical and quadratic aperture phase distributions and HFSS simulations, are listed in Table 2.1 for different horn geometries. The waveguides used have the same diameter $d_w = 0.333\lambda$. The results show good agreement between HFSS-simulated data and data obtained using the spherical aperture phase distribution. The assumed dimensions in this table give different results using the quadratic and spher-

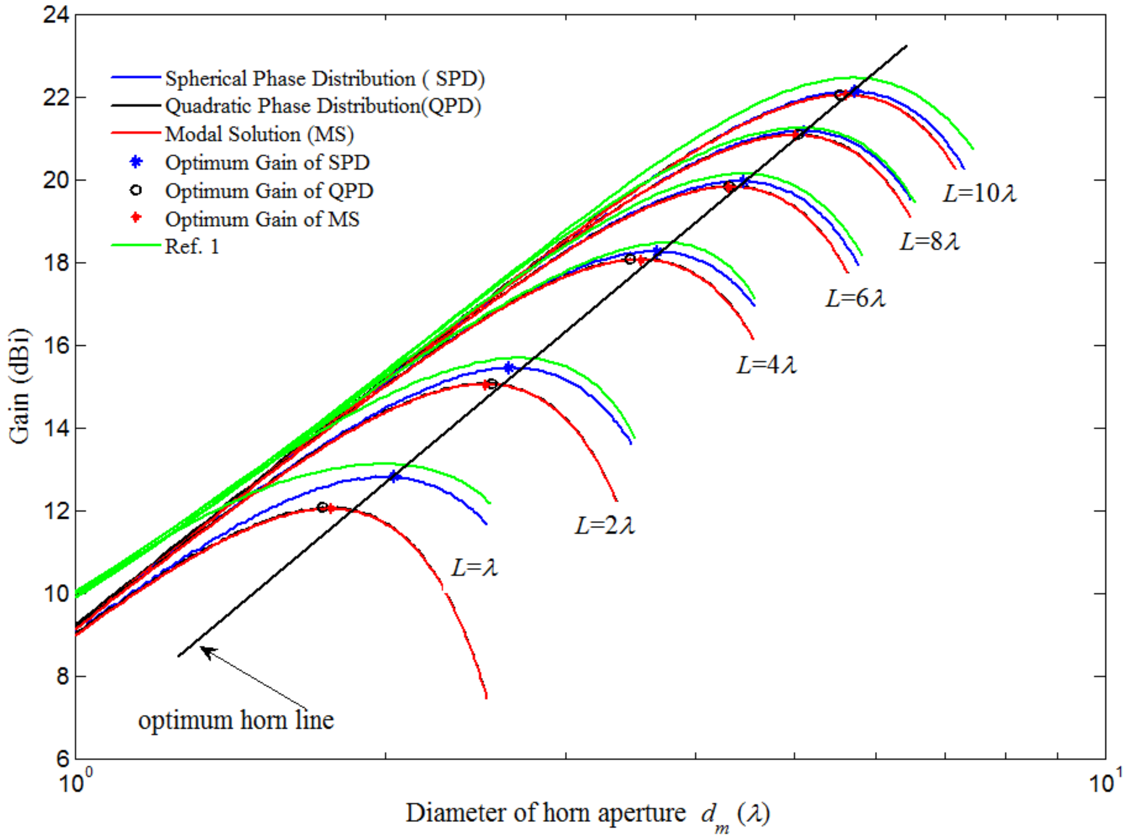

Fig. 2.7. Simulated Gain of a Conical Horn Antenna as a Function of Aperture Diameter and for Different Axial Horn lengths.

ical aperture phase distributions. This agreement is further evidence on the validity of the spherical aperture phase distribution adopted in this work.

Table 2.1. Simulated and Calculated Gain of Conical Horns

$L(\lambda)$	$d_m(\lambda)$	G_{HFSS}(dBi)	G_{QPD}(dBi)	G_{SPD}(dBi)
1.0	3.0	7.95	3.49	7.653
2.0	3.0	15.03	14.19	15.13
2.8	4.1	14.7	12.79	14.55
3.1	3.6	16.99	16.44	16.97
3.5	3.4	17.98	17.46	17.67

2.2.4. *Optimum Horn*

The conical horn dimensions which correspond to a maximum gain, lead to optimum gain designs. The optimum design line is indicated by the *black solid straight line* in Fig. 2.7. Referring to Fig. 2.7, as the optimum gain increases, the optimum dimensions are in excellent agreement for the spherical and quadratic aperture phase distributions. By using curve fitting of the data obtained numerically, based on the spherical aperture phase distribution, improved equations were developed for optimum design. By fitting data, representing the optimal gains and axial lengths, to a linear model using least-squares techniques, a new equation is introduced.

$$G_{opt} \approx 15.9749\,(L/\lambda) + 1.7209 \tag{2.29}$$

For the relationship between the optimal gain and optimal diameter, the second-order polynomial regression was useful for fitting a model, resulting in

$$G_{opt} \approx 5.1572\,(d_m/\lambda)^2 - 0.6451\,(d_m/\lambda) + 1.3645 \tag{2.30}$$

Similarly, the relationship between the optimal axial lengths and diameters was modeled using a second-order polynomial regression leading to

$$L \approx 0.3232\,(d_m/\lambda)^2 - 0.0475\,(d_m/\lambda) + 0.0052 \tag{2.31}$$

The data in Fig. 2.8, as well as (2.29)-(2.31), can be used to design optimum gain horns. By specifying the optimum gain (in dB) and using these equations, the optimum dimensions (in wavelengths) of a conical horn can be determined. For optimum axial lengths and

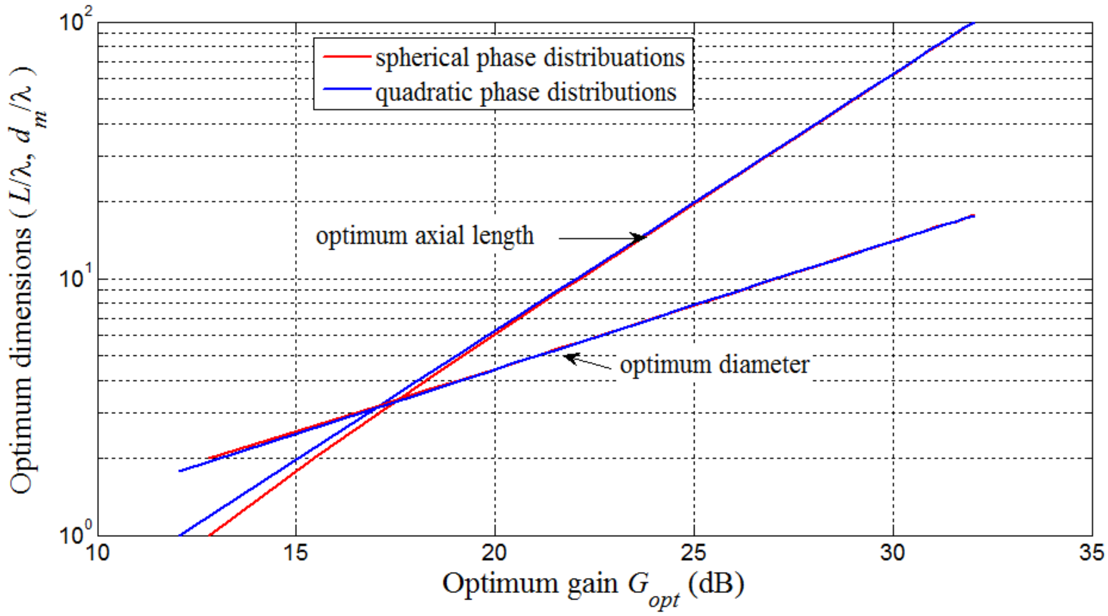

Fig. 2.8. Optimum Design of the Conical Horn Antenna Based on Spherical and Quadratic Aperture Phase Distributions.

diameters, (2.29)-(2.31) match the data obtained by using spherical or quadratic aperture phase distributions when the optimum gain is equal to or larger than 20 dB. From Fig. 2.8, it can be seen that the spherical and quadratic aperture phase distributions result in different optimum axial lengths when the gain is less than about 20 dB.

2.2.5. *Aperture Efficiency*

The aperture efficiency represents the reduction in gain due to the amplitude and phase tapers across the horn aperture. Here, the TE_{11} mode, which is the dominant mode of a circular waveguide, has a non-uniform amplitude distribution that results in an amplitude taper efficiency ε_t of 0.836 [1]. The aperture phase (ε_p) and amplitude (ε_t) tapers are represented by L_p and L_t, respectively, and they are related to the aperture efficiency (ε_{ap})

and the loss factor by [1]

$$LF(s) = -10\log_{10}(\varepsilon_{ap}) = -10\log_{10}(\varepsilon_t\varepsilon_p) = L_t + L_p \tag{2.32}$$

where

$$\varepsilon_{ap} = \varepsilon_t\varepsilon_p \tag{2.33}$$

$$L_t = -10\log_{10}(\varepsilon_t) = -10\log_{10}(0.836) = 0.778\,\text{dB} \tag{2.34}$$

$$L_p(s) = -10\log(\varepsilon_p) \tag{2.35}$$

The aperture efficiency is the product of the taper efficiency and phase efficiency [1]. The taper efficiency represents the uniformity of the amplitude distribution of the field over the horn aperture, while the phase efficiency represents the phase uniformity of the field over the horn aperture. The gain (in dB) is related to the aperture area and aperture efficiency by

$$G(\text{dB}) = 10\log_{10}\left[\varepsilon_{ap}\frac{4\pi}{\lambda^2}\left(\pi a^2\right)\right] = 10\log_{10}\left(\frac{C}{\lambda}\right)^2 - LF(s) \tag{2.36}$$

$$s = \frac{d_m^2}{8l\lambda} \tag{2.37}$$

where s is the maximum phase deviation, a is the radius of the horn at the aperture, C is the aperture circumference, and LF (in dB) is the loss factor that accounts for the reduction in gain due to the aperture efficiency. The first term in (2.36) represents the gain of a circular aperture with uniform distribution, whereas the second term, represented by (2.34) and (2.35), are correction factors to account for the loss in gain due to the amplitude and phase tapers, respectively.

It is difficult to find an exact expression for the loss factor, hence the gain. However, using numerical integration and curve fitting, new equations were developed for the loss factor and gain. The data which represent the loss factor were fitted with a third-order polynomial. The obtained expressions were compared with other expressions that are readily available in the literature. The available closed-form approximations for the conical horn loss factor, and hence the gain, were examined. It turns out that the first approximation in [1] and [15] is not consistent with the conical horn gain pattern for aperture phase deviation $s \geq 0.5\lambda$, whereas the second approximation in [5] is not consistent with the conical horn gain pattern for an aperture phase deviation $s \geq 0.5\lambda$ and an axial length $L \leq 3\lambda$. For the first approximation, a polynomial expression for LF (in dB) is given in [1], [15]

$$LF(s) \approx 0.8 - 1.71s + 26.25s^2 - 17.97s^3 \tag{2.38}$$

The second approximation proposed in [5] improves the loss factor and gain prediction at large axial lengths ($L > 3\lambda$). Here the loss factor is represented by:

$$LF(s) \approx 0.75 + 0.66s + 9.4s^2 + 6.8s^3 \tag{2.39}$$

In this work, improved expressions are derived for the gain and loss factor for a conical horn. From the data obtained numerically, it is difficult to get one equation for all dimensions. Therefore, two equations were derived; one when L is equal to or smaller than 3λ and the other when L is larger than 3λ. These equations improve the accuracy of the predicted loss factor (in dB) and gain values.

$$LF(s) \approx 0.5030 + 5.1123s - 7.1138s^2 + 23.1401s^3 \quad L \leq 3\lambda \tag{2.40}$$

$$L_p(s) \approx -0.275 + 5.1123s - 7.1138s^2 + 23.1401s^3 \quad L \leq 3\lambda \tag{2.41}$$

$$LF(s) \approx 0.7853 - 0.3976s + 13.112s^2 + 3.901s^3 \quad L > 3\lambda \tag{2.42}$$

$$L_p(s) \approx -0.3976s + 13.112s^2 + 3.901s^3 \quad L > 3\lambda \tag{2.43}$$

The conformity of (2.32) used with (2.38)-(2.43) for the loss factor and gain is examined

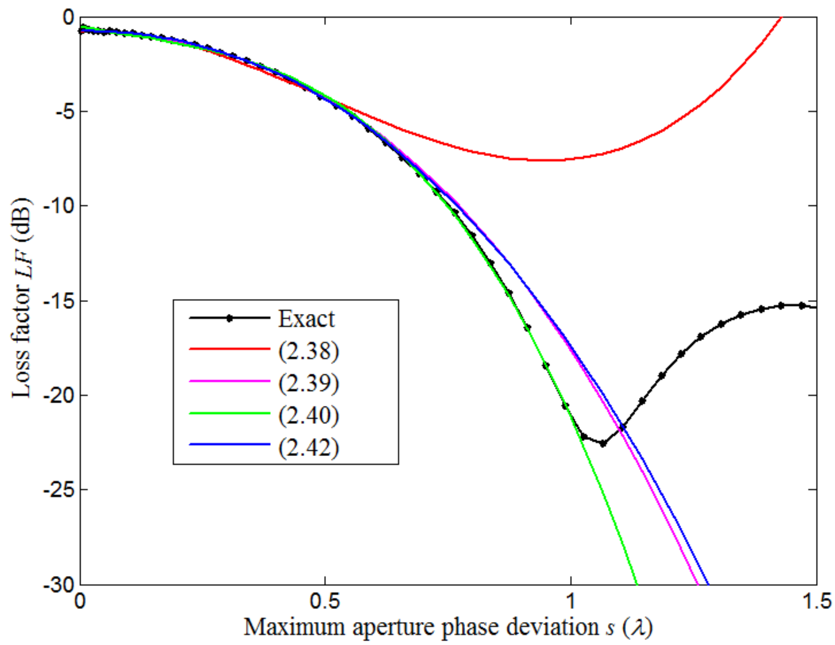

Fig. 2.9. Conical Horn Loss Factor as a Function of Maximum Aperture Phase Deviation ($L = 1.5\lambda$).

in Figs. 2.9 and 2.11 for a small axial length ($L = 1.5\lambda$) and in Figs. 2.10 and 2.12 for a large axial length ($L = 50\lambda$), where the loss factor and gain of a conical horn antenna are plotted as a function of the maximum aperture phase deviation.

It is apparent that the new expressions, (2.40) and (2.42), predict the loss factor and gain more accurately, unlike (2.38) and (2.39) where the first approximation is not consistent with the conical horn gain pattern for a maximum aperture phase deviation more than 0.5λ.

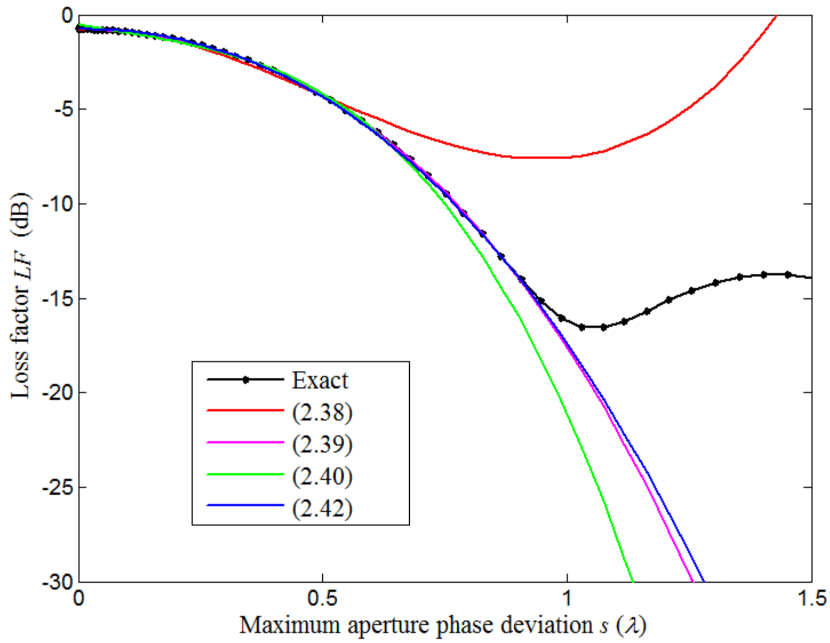

Fig. 2.10. Conical Horn Loss Factor as a Function of Maximum Aperture Phase Deviation $(L = 50\lambda)$.

The second approximation proposed in [5] improves the gain prediction for large axial lengths $(L > 3\lambda)$, but gives inaccurate predictions for small axial lengths $(L \le 3\lambda)$. From (2.43), it is seen that when $s = 0$, the loss is equal to zero because L is large enough to generate spherical waves at the aperture, but for small L, the loss is nonzero when $s = 0$ because the assumption of a virtual point source is no longer valid for small L. It is obvious that the new expressions are fairly accurate for predicting the loss factor; hence the gain of the conical horn antennas, and these expressions are restricted to a maximum aperture phase deviation of about 1λ.

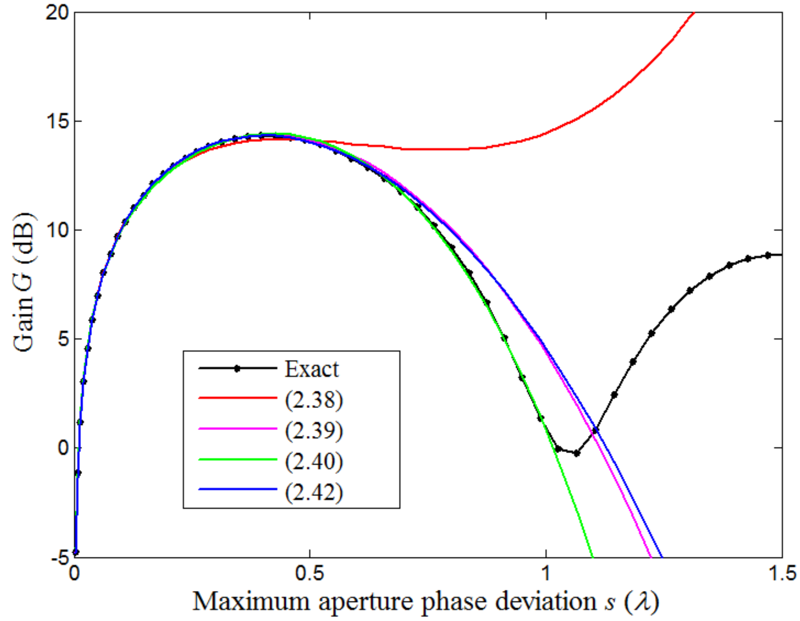

Fig. 2.11. Conical Horn Gain as a Function of Maximum Aperture Phase Deviation ($L = 1.5\lambda$).

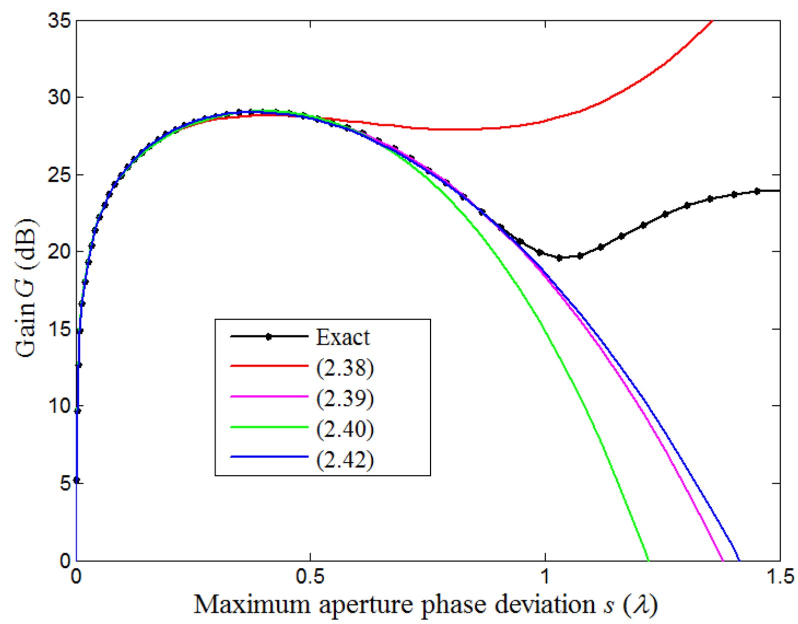

Fig. 2.12. Conical Horn Gain as a Function of Maximum Aperture Phase Deviation ($L = 50\lambda$).

CHAPTER 3

UNCOATED APERTURE ANTENNAS

In many applications, uncoated aperture antennas are used either in free space or mounted on ground planes. In both cases, the aperture edge or the ground plane edge affects the radiation characteristics of the antenna because of the scattering from these edges. The geometry of the edge (straight or curved), the size of the ground plane, and the aperture dimension have an impact on the intensity of the diffraction in the region around the antenna. In some applications, the aperture antennas are not mounted on ground planes, utilized as a gain standard for calibration and gain measurements, where the diffractions of the aperture edge need to be investigated. For aviation applications, aperture antennas are integrated into the surface of the spacecraft or aircraft. Then the diffractions coming from the ground plane edges need to be examined to predict accurately the radiation characteristics of the antenna.

3.1. Geometrical Optics

One of the most versatile and useful ray-based high-frequency techniques is the Geometrical Optics (GO) [11], [16]. The geometrical optics ray field consists of direct, refracted, and reflected rays. When an infinite scatterer is illuminated by a high-frequency radiating source, the GO accurately predicts the total field (direct and reflected) at any observation point. But, the GO fails to account for impact that results when the scatterer is finite. It is well known that electromagnetic waves are physically continuous, in magnitude and phase, in time and space domains. However, the geometrical optics has limitations where the GO yields fields that are discontinuous across the shadow boundaries created by the geometry of the problem. GO is insufficient to describe completely the scattered field in practical applications due to the inaccuracies inherent to GO near the shadow boundaries and in the shadow zone. The GO predicts zero fields in the shadow zone. This prediction does not physically exist. To overcome some of the deficiencies of geometrical optics, the Geometrical Theory of Diffraction (GTD) and Uniform Theory of Diffraction (UTD) were introduced [17-22]. The GTD/UTD is a ray method enhancing the GO by incorporating diffracting rays to geometrical optics [23].

The GO fields radiated from aperture antennas are determined from a knowledge of the fields (magnitude and phase) over the aperture of the antenna. The aperture fields become the sources of the fields radiated at far observation points. This is a variation of the Huygens-Fresnel principle, which states "each point on a primary wavefront can be considered to be a new source of a secondary spherical wave and that a secondary wavefront can be constructed as the envelope of these secondary spherical waves" [1], [11].

To find far-zone radiation characteristics of an aperture antenna, the equivalence principle, in terms of equivalent current densities $\mathbf{J}_s$ and $\mathbf{M}_s$, can be utilized to represent the fields at the aperture of the antenna. When the antenna is not mounted on an infinite ground plane, an approximate equivalent is utilized in terms of both $\mathbf{J}_s$ and $\mathbf{M}_s$ [11]. An exact equivalent is formed utilizing only $\mathbf{M}_s$ expressed in terms of the tangential electric fields at the aperture mounted on an infinite ground plane [11].

Most aperture antennas are excited by waveguides. For the conical horn antenna, a circular waveguide is used as a feed. To find the aperture field of the horn, the dominant mode fields in the waveguide are projected forward to become an approximate of this field, and then they can be used in an equivalent principle. An analytical study on the radiation characteristics of a conical horn, either unmounted or mounted on a ground plane, requires accurate amplitude and phase expressions for the fields over the aperture. A spherical phase term, representing the spherical phase variations over the aperture, is added to the waveguide-derived fields such as the aperture fields have emanated from a virtual vertex located in the waveguide at the point of intersection of the horn walls.

The total fields in space at a given observation point are a combination of the components of GO and GTD/UTD. Depending on the geometry of the problem, GTD/UTD can provide other diffraction mechanisms (slope diffraction, equivalent current contribution) to increase the prediction accuracy. The total field in space at a given observation point around the wedge can be represented by

$$\mathbf{E}_{\mathbf{Total}} = \mathbf{E}_{\mathbf{Direct}} + \mathbf{E}_{\mathbf{Reflected}} + \mathbf{E}_{\mathbf{Diffracted}}$$

$$\mathbf{E}_{\mathbf{Total}} = \mathbf{E}_{\mathbf{GO}} + \mathbf{E}_{\mathbf{GTD/UTD}}$$

where GO represents the direct and reflected field contributions and GTD/UTD represents the diffracted field contributions. By summing vectorially the GO and GTD/UTD contributions, the total field is computed at a given observation point.

Since the GTD/UTD is an extension of geometrical optics to describe diffraction phenomena, the geometrical optics analysis of a conical horn in both cases, unmounted and mounted on a ground plane, will be briefly reviewed. In addition, the geometrical optics analysis of a circular waveguide mounted on a ground plane will be derived using some advanced functions and identities.

3.1.1. *Free Space Solution of Conical Horn Antennas*

Based on the previous section, we assume the TE_{11} mode in the circular waveguide continues to propagate within the horn in the form of a cylindrical Bessel function with a spherical phase distribution, rather than a uniform plane wavefront along the symmetry axis of the antenna, as shown in Fig. 2.4. The conical horn, with an aperture radius a, is connected to a circular waveguide, and the electric field components over its aperture can be represented by

$$E_\rho = \frac{E_0}{\rho'} J_1\left(\chi'_{11}\frac{\rho'}{a}\right)\sin(\phi')\, e^{-jk\delta(\rho')} \quad \rho' \leq a \tag{3.1}$$

$$E_\phi = E_0\, J_1'\left(\chi'_{11}\frac{\rho'}{a}\right)\cos(\phi')\, e^{-jk\delta(\rho')} \quad \rho' \leq a \tag{3.2}$$

where $k = 2\pi/\lambda$, $\chi'_{11} = 1.8412$, $' = \frac{\partial}{\partial\rho'}$, and $\delta(\rho')$ is the path difference term representing the fields' spherical phasefronts, and it is represented by (2.1).

In this case, the conical horn is not mounted on a ground plane. Therefore, the electric and magnetic equivalent current densities across the horn aperture have to be considered [1], [11]. The total electromagnetic fields radiated by the horn aperture in the far-field region, due to electric and magnetic sources, are calculated by using the Aperture Integration method (AI), and they can be written as [1], [11]

$$E_\theta = j\frac{E_0 k_\rho k}{4r}\, e^{-jkr}\,(1+\cos\theta)\,\sin\phi\; L_\theta \tag{3.3}$$

$$E_\phi = j\frac{E_0 k_\rho k}{4r}\, e^{-jkr}\,(1+\cos\theta)\,\cos\phi\; L_\phi \tag{3.4}$$

where

$$L_\theta = \int_0^a \left[\rho' J_0\left(k_\rho\rho'\right) J_0\left(k\rho'\sin\theta\right) - \rho' J_2\left(k_\rho\rho'\right) J_2\left(k\rho'\sin\theta\right)\right] e^{-jk\delta(\rho')}\, d\rho' \tag{3.5}$$

$$L_\phi = \int_0^a \left[\rho' J_0\left(k_\rho \rho'\right) J_0\left(k\rho' \sin\theta\right) + \rho' J_2\left(k_\rho \rho'\right) J_2\left(k\rho' \sin\theta\right)\right] e^{-jk\delta(\rho')}\, d\rho' \qquad (3.6)$$

These components represent the field radiated in the forward direction of $0 \leq \theta \leq \frac{\pi}{2}$. Also zero radiation is assumed in the back region (shadow zone).

3.1.2. *Infinite Ground Plane Solution of Conical Horn Antennas*

In this case, a circular aperture of a conical horn antenna is mounted on an infinitely thin perfectly electric conducting ground plane. The fields over the aperture of the horn are those of a TE_{11} mode for a circular waveguide. The only difference is the inclusion of a complex exponential term which represents the spherical phase distribution over the aperture.

To find the radiation characteristics of a conical horn mounted on PEC ground plane, the equivalence principle, in terms of an equivalent magnetic current density $\mathbf{M}_s$, can be utilized to represent the fields at the aperture of the horn. Because of the boundary condition, only the magnetic equivalent current density is nonzero over the aperture [1], [11]. By using the aperture integration method, the far-zone fields of the conical horn antenna mounted on an infinite ground plane are given by

$$E_\theta = j\frac{E_0 k_\rho k}{2r}\, e^{-jkr}\, \sin\phi\, L_\theta \qquad (3.7)$$

$$E_\phi = j\frac{E_0 k_\rho k}{2r}\, e^{-jkr} \cos\theta\, \cos\phi\, L_\phi \qquad (3.8)$$

where L_θ and L_ϕ are presented, respectively, by (3.5) and (3.6).

Equations (3.7)-(3.8) represent the three-dimensional distributions of the far-zone fields radiated by a conical horn antenna mounted on an infinite PEC ground plane, in the forward direction of $0 \leq \theta \leq \frac{\pi}{2}$.

3.1.3. *Infinite Ground Plane Solution of Circular Waveguide Antennas*

The geometry of a circular aperture of radius a, mounted on an infinite ground plane, is shown in Fig. 3.1. The coordinate system is located at the center of the aperture. The cylindrical coordinate system is the most convenient to represent the fields at the aperture and to perform the integration due to the circular aperture's configuration.

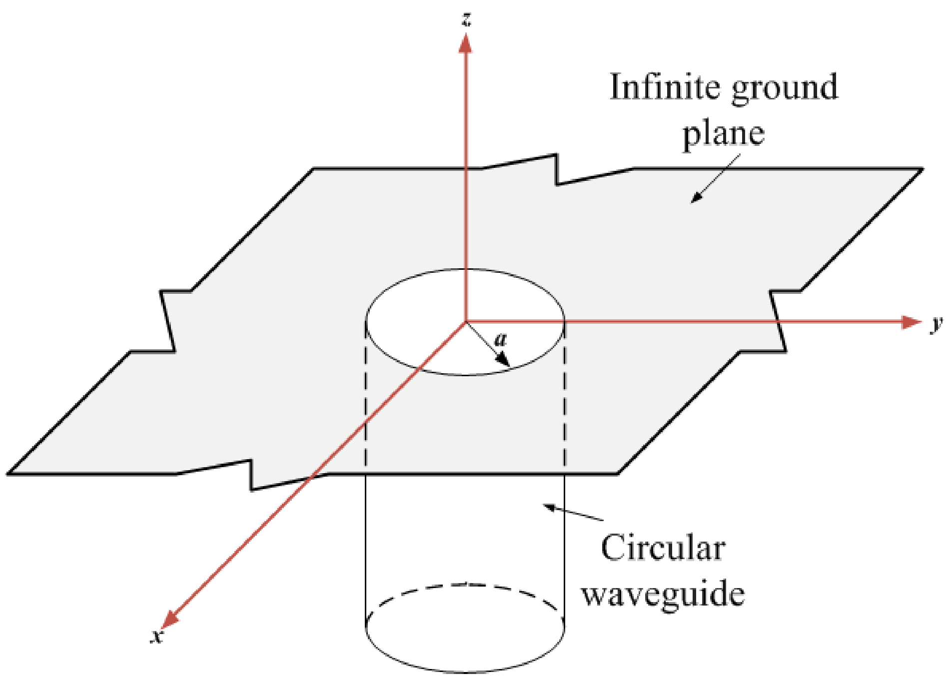

Fig. 3.1. Geometry of a Circular Waveguide Mounted on an Infinite Ground Plane.

The electric field components over the aperture are assumed to be the TE_{11}-mode fields of the circular waveguide and are expressed as

$$E_\rho = \frac{E_0}{\rho'} J_1\left(\chi_{11}\frac{\rho'}{a}\right)\sin(\phi') \qquad \rho' \leq a \tag{3.9}$$

$$E_\phi = E_0 J_1'\left(\chi_{11}\frac{\rho'}{a}\right)\cos(\phi') \qquad \rho' \leq a \tag{3.10}$$

These fields are assumed to be known and are produced by the circular waveguide which feeds the aperture antenna mounted on the ground plane. Here the exponential term, included for the conical horn, is not considered because the flare angle is zero. The problem is to determine the radiated fields at far observation points. The fields radiated by the aperture can be computed by using the fields equivalence principle [1] which states that the aperture fields may be replaced by equivalent electric and magnetic surface currents whose radiated fields can then be calculated using the techniques of Sec. 12.2 of [1]. Using the equivalence principle, the equivalent electric and magnetic surface currents, respectively, are:

$$\underline{J}_s = 0 \qquad \text{everywhere} \tag{3.11}$$

$$\underline{M}_s = -2\hat{n}\times\underline{E}_a \qquad \rho' \leq a \tag{3.12}$$

where $\hat{n}$ is a unit vector normal to the surface and on the side of the radiated fields, and $\underline{E}_a$ is the total electric field over the aperture S. Since the electric surface current is zero due to the infinite ground plane, the potential vectors are expressed as follows:

$$\underline{A} = \frac{\mu_0}{4\pi}\iint_S \underline{J}_s \frac{e^{-jkR}}{R} dS' = 0 \tag{3.13}$$

$$\underline{F} = \frac{\varepsilon_0}{4\pi} \iint_S \underline{M}_s \frac{e^{-jkR}}{R} dS' \neq 0 \tag{3.14}$$

where S is the area of the aperture and R represents the distance from any point in the source (aperture) to the observation point.

As shown in section 12.3 of [1], for the far-field observations R can most commonly be approximated by

$$R \simeq r - r' \cos\psi \quad \text{for phase variations} \tag{3.15}$$

$$R \simeq r \quad \text{for amplitude variations} \tag{3.16}$$

where ψ is the angle between the vectors $\hat{r}$ and $\hat{r}'$, as shown in Figure 12.16 of [1]. Using this far-field approximation, the vector potential $\underline{F}$, defined for the magnetic source $\underline{M}_s$, can be expressed as

$$\underline{F} = \frac{\varepsilon_0}{4\pi} \iint_S \underline{M}_s \frac{e^{-jkR}}{R} dS' \simeq \varepsilon_0 \frac{e^{-jkr}}{4\pi r} (\hat{\theta} L_\theta + \hat{\phi} L_\phi) \tag{3.17}$$

where

$$L_\theta = \iint_S [M_\rho \cos\theta \cos(\phi - \phi') + M_\phi \cos\theta \sin(\phi - \phi') - M_z \sin\theta]\ e^{jkr' \cos\psi} ds' \tag{3.18}$$

$$L_\phi = \iint_S [-M_\rho \sin(\phi - \phi') + M_\phi \cos(\phi - \phi')]\ e^{jkr' \cos\psi} ds' \tag{3.19}$$

from (3.12), we have

$$\underline{M}_s = \hat{\rho} M_\rho + \hat{\phi} M_\phi \quad \rho' \leq a \tag{3.20}$$

where $M_\rho = 2E_\phi$, and $M_\phi = -2E_\rho$

Since M_z is zero, the expression in (3.18) can be simplified. Thus, θ and ϕ components of the $\underline{L}$ vectors for the far-field radiation reduce to

$$L_\theta = \cos\theta \iint_S [M_\rho \cos(\phi-\phi') + M_\phi \sin(\phi-\phi')]\ e^{jk\rho'\sin\theta\cos(\phi-\phi')}\rho' d\rho' d\phi' \tag{3.21}$$

$$L_\phi = \iint_S [-M_\rho \sin(\phi-\phi') + M_\phi \cos(\phi-\phi')]\ e^{jk\rho'\sin\theta\cos(\phi-\phi')}\rho' d\rho' d\phi' \tag{3.22}$$

where

$$r'\cos\psi = \rho'\sin\theta\cos(\phi-\phi') \tag{3.23}$$

After substituting the tangential magnetic sources (M_ρ and M_ϕ) into (3.21) and (3.22), they reduce to

$$L_\theta = 2E_0\cos\theta \int_0^a \left[-J_1\left(\chi_{11}\frac{\rho'}{a}\right) I_{\theta 1} + \rho' J_1'\left(\chi_{11}\frac{\rho'}{a}\right) I_{\theta 2}\right] d\rho' \tag{3.24}$$

$$L_\phi = -2E_0 \int_0^a \left[J_1\left(\chi_{11}\frac{\rho'}{a}\right) I_{\phi 1} + \rho' J_1'\left(\chi_{11}\frac{\rho'}{a}\right) I_{\phi 2}\right] d\rho' \tag{3.25}$$

where

$$I_{\theta 1} = \int_{-\pi}^{\pi} \sin\phi' \sin(\phi-\phi')\ e^{jk\rho'\sin\theta\cos(\phi-\phi')} d\phi' \tag{3.26}$$

$$I_{\theta 2} = \int_{-\pi}^{\pi} \cos\phi' \cos(\phi-\phi')\ e^{jk\rho'\sin\theta\cos(\phi-\phi')} d\phi' \tag{3.27}$$

$$I_{\phi 1} = \int_{-\pi}^{\pi} \sin\phi' \cos(\phi-\phi')\ e^{jk\rho'\sin\theta\cos(\phi-\phi')} d\phi' \tag{3.28}$$

$$I_{\phi 2} = \int_{-\pi}^{\pi} \cos\phi' \sin(\phi-\phi')\ e^{jk\rho'\sin\theta\cos(\phi-\phi')} d\phi' \tag{3.29}$$

To solve the complex integrations above, the exponent needs to be expanded in terms of Bessel functions and trigonometric functions [24] as follows:

$$e^{jk\rho'\sin\theta\cos(\phi-\phi')} = J_0(k\rho'\sin\theta) + 2\sum_{n=1}^{\infty} j^n J_n(k\rho'\sin\theta)\cos n(\phi-\phi') \tag{3.30}$$

As a result, (3.26)-(3.29) are simplified to

$$I_{\theta 1} = -\pi \cos\phi (J_0(k\rho' \sin\theta) + J_2(k\rho' \sin\theta)) \tag{3.31}$$

$$I_{\theta 2} = +\pi \cos\phi (J_0(k\rho' \sin\theta) - J_2(k\rho' \sin\theta)) \tag{3.32}$$

$$I_{\phi 1} = +\pi \sin\phi (J_0(k\rho' \sin\theta) - J_2(k\rho' \sin\theta)) \tag{3.33}$$

$$I_{\phi 2} = +\pi \sin\phi (J_0(k\rho' \sin\theta) + J_2(k\rho' \sin\theta)) \tag{3.34}$$

After substituting (3.31)-(3.34) into (3.24)-(3.25) and assuming that $\beta = k \sin\theta$ and $\alpha = \frac{\chi'_{11}}{a}$, they simplify to

$$\begin{aligned} L_\theta = k_0 \cos\theta \cos\phi \int_0^a \Big(&\left[J_1\left(\alpha\rho'\right) + \rho' J_1'\left(\alpha\rho'\right)\right] J_0(\beta\rho') \\ &+ \left[J_1\left(\alpha\rho'\right) - \rho' J_1'\left(\alpha\rho'\right)\right] J_2(\beta\rho')\Big) d\rho' \end{aligned} \tag{3.35}$$

$$\begin{aligned} L_\phi = -k_0 \sin\phi \int_0^a \Big(&\left[J_1\left(\alpha\rho'\right) + \rho' J_1'\left(\alpha\rho'\right)\right] J_0(\beta\rho') \\ &- \left[J_1\left(\alpha\rho'\right) - \rho' J_1'\left(\alpha\rho'\right)\right] J_2(\beta\rho')\Big) d\rho' \end{aligned} \tag{3.36}$$

where $k_0 = 2\pi E_0$

Useful identities relating Bessel functions and their derivatives [24] are given by

$$J_{n-1}(x) = \frac{n}{x} J_{n-1}(x) + \frac{\mathrm{d}J_n(x)}{\mathrm{d}x} \tag{3.37}$$

$$J_{n+1}(x) = \frac{n}{x} J_{n-1}(x) - \frac{\mathrm{d}J_n(x)}{\mathrm{d}x} \tag{3.38}$$

substituting (3.37) and (3.38) into (3.35) and (3.36), we have

$$L_\theta = k_0\, \alpha \cos\theta \cos\phi \int_0^a \rho' \Big[J_0(\alpha\rho') J_0(\beta\rho') + J_2(\alpha\rho') J_2(\beta\rho') \Big] d\rho' \tag{3.39}$$

$$L_\phi = -k_0\,\alpha \sin\phi \int_0^a \rho' \Big[J_0(\alpha\rho')J_0(\beta\rho') - J_2(\alpha\rho')J_2(\beta\rho')\Big] d\rho' \tag{3.40}$$

These are evaluated with the help of the Lommel integral formula [24]

$$\int_0^{\rho'} \rho' J_n\left(\alpha\rho'\right) J_n(\beta\rho') d\rho' = \frac{\rho'}{\alpha^2-\beta^2}\left[J_n(\alpha\rho')\frac{dJ_n(\beta\rho')}{d\rho'} - J_n(\beta\rho')\frac{dJ_n(\alpha\rho')}{d\rho'}\right] \tag{3.41}$$

Using this formula for $n = 0$ and $n = 2$, we have

$$\gamma_0 = \int_0^a \rho' J_0\left(\alpha\rho'\right) J_0(\beta\rho') d\rho' = \frac{a}{\alpha^2-\beta^2}\left[\alpha J_1(\alpha a)J_0(\beta a) - \beta J_1(\beta a)J_0(\alpha a)\right] \tag{3.42}$$

$$\gamma_2 = \int_0^a \rho' J_2\left(\alpha\rho'\right) J_2(\beta\rho') d\rho' = \frac{a}{\alpha^2-\beta^2}\left[\beta J_2(\alpha a)J_1(\beta a) - \alpha J_2(\beta a)J_1(\alpha a)\right] \tag{3.43}$$

and then (3.39) and (3.40) reduce to

$$L_\theta = k_0 \cos\theta\cos\phi(\gamma_0 + \gamma_2) \tag{3.44}$$

$$L_\phi = -k_0 \sin\phi(\gamma_0 - \gamma_2) \tag{3.45}$$

which reduce to

$$L_\theta = \frac{2a\alpha^2 k_0}{\alpha^2-\beta^2}\cos\theta\cos\phi\Big(J_1(\alpha a)J_1'(\beta a)\Big) \tag{3.46}$$

$$L_\phi = -\frac{2k_0}{\beta}\sin\phi\Big(J_1(\alpha a)J_1(\beta a)\Big) \tag{3.47}$$

Finally, the far-zone fields radiated by the circular waveguide antenna can be written as

$$E_\theta = \frac{jkaE_0 e^{-jkr}}{r}\sin\phi\, J_1(\chi_{11})\frac{J_1(ka\sin\theta)}{ka\sin\theta} \tag{3.48}$$

$$E_\phi = \frac{jkaE_0 e^{-jkr}}{r}\cos\theta\cos\phi\, J_1(\chi_{11})\frac{J_1'(ka\sin\theta)}{1-(\frac{ka\sin\theta}{\chi_{11}})^2} \tag{3.49}$$

3.2. Geometrical Theory of Diffraction for an Edge on a Perfectly Conducting Surface

As is well known, geometrical optics has some limitations because it does not predict the fields in the shadow region. Also, GO is inaccurate in the vicinity of the shadow boundaries. The GO predicts zero diffracted fields everywhere and zero direct and reflected fields in the shadow region. Therefore, the Geometrical Theory of Diffraction (GTD) is required to overcome these deficiencies. The GTD supplements and enhances geometrical optics by adding contributions due to edge diffractions at perfectly conducting edges. The introduction of the Geometrical Theory of Diffraction (GTD) by Keller [17-18] and its modified version, the Uniform Theory of Diffraction (UTD) introduced by Kouyoumjian and Pathak [19-22], have proved to be very valuable in solving antenna problems that otherwise may have been intractable. However unlike GTD, UTD accurately predicts the diffracted field along the incident and reflection shadow boundaries. The application of this theory on a $\lambda/4$ monopole mounted on infinitely thin, perfectly conducting, finite square and circular ground planes has been examined in [11]. Also, the thickness of the ground plane affects radiation patterns. This effect has been studied both theoretically and experimentally in [25], where the amplitude patterns of a $\lambda/4$ monopole mounted on thick finite circular and square ground planes are presented. The uniform theory of diffraction was used in [26] to calculate the edge diffracted fields from the finite ground plane of a microstrip antenna. In this study, a model of combining the slot theory [27], [28] and the method of uniform theory of diffraction [23] to account for the finite ground plane edge diffractions in both E- and H-plane calculations. In addition, the radiation patterns of an infinitesimal monopole mounted on the tip of a perfectly conducting, finite length cone was calculated using diffraction techniques where the amplitude patterns were obtained from the superposition of the field radiated directly from the infinitesimal dipole mounted on the tip of a perfectly conducting infinite length con and the field diffracted from the edge of the finite length cone [29].

The aperture edge effect on the amplitude patterns in the E and H planes of a conical horn antenna without a ground plane has been reported in the literature. The modal solution was used to obtain the fields within the horn, and then UTD was applied to evaluate the diffraction from the aperture edge assuming the incident fields propagate from a virtual apex along the slant radius [30], [31]. In [30], the measured patterns have not been extended below -40 dB in the H plane because of the limited dynamic range of the receiver used. The validity of calculation and measurements was restricted to regions over which validation was achieved in [31]. Therefore, it is really not known how well the calculated and measured patterns agree beyond the limit of the experimental dynamic range.

In this chapter, the GTD analysis of the far-zone E-plane and H-plane amplitude patterns of circular aperture antennas, unmounted or mounted on finite square and circular ground planes, is presented. The study enables one to accurately predict the far-zone E- and H-plane amplitude patterns over the main beam, near and far sidelobes, and backlobes.

The analysis of the edge diffraction of the ground plane on the amplitude patterns of conical horn and circular waveguide antennas mounted at the center of finite square and circular ground planes is presented. The fields of conical horn and circular waveguide antennas mounted on an infinite ground plane or the field of a conical horn antenna without a ground plane, which are well known, are supplemented, respectively, by the fields diffracted at the edges of the ground plane and the antenna aperture. The UTD is utilized to calculate the diffracted field components.

The circular edge of the circular ground plane and the antenna aperture has a caustic along its axis, and the GTD/UTD predicts an infinite field there, which physically does not exist. This deficiency can be overcome by the use of equivalent edge currents [32]. This method extends GTD/UTD to any direction, and uses the equivalent currents as the source of the diffracted field. The fictitious currents, both electric and magnetic, flowing along the edge, produce a finite field value at the caustic region using the line integral technique of these currents around the circular rim. These currents do not really exist at the discontinuity edge, but they are a mathematical aid to accurately predict the diffracted field at and near the axial caustics. Away from the axial caustic region, the regular GTD/UTD leads to a prescription of the total diffracted field as the sum of contributions from a pair of the diametrically opposed flush points.

3.2.1. *Diffracted Field Solution*

The total field can be calculated by summing the GO fields and the fields diffracted from the edge of the ground plane, or from the antenna aperture's edges for the antennas that are not mounted on a ground plane. According to the uniform theory of diffraction

[11], the diffracted field can be expressed as

$$\overline{E}^{d} = \overline{E}^{i}(Q_d) \cdot \overline{\overline{D}} \sqrt{\frac{\rho_c}{s(\rho_c + s)}} \exp(-jks) \tag{3.50}$$

where $\overline{E}^{i}(Q_d)$ is the electric field incident at a point Q_d on the edge, $\overline{\overline{D}}$ is the dyadic diffraction coefficient $\overline{\overline{D}} = -\hat{\beta}_0' \hat{\beta}_0 D_s - \hat{\phi}' \hat{\phi} D_h$, where D_s and D_h are, respectively, the soft and hard diffraction coefficients. ρ_c is the distance between the caustic at the edge and the second caustic of the diffracted ray. The unit vectors $\hat{\beta}_0', \hat{\beta}_0, \hat{\phi}', \hat{\phi}$, together with ρ_c, are illustrated in Figure 13-31 of [11]. ρ_c is given by

$$\frac{1}{\rho_c} = \frac{1}{\rho_e^i} - \frac{\hat{n}.(\hat{s}' - \hat{s})}{\rho_g \sin^2 \beta_0'} \tag{3.51}$$

where ρ_e^i is the radius of curvature of the incident wavefront at Q_d taken in the plane containing the incident ray and the unit vector tangent to the edge at Q_d; ρ_g is the radius of curvature of the edge at Q_d; $\hat{n}$ is the unit normal to the edge directed away from the center of curvature; β_0' is the angle between the incident ray and the tangent to the edge at Q_d; and $\hat{s}'$, $\hat{s}$ are, respectively, unit vectors in the direction of incidence and diffraction. The soft and hard polarization diffraction coefficients are represented by

$$\begin{aligned} D^{s,h} = \frac{-e^{-j\pi/4}}{2n\sqrt{2\pi k}\sin\beta_0'} \Bigg(\left\{ \cot\left[\frac{\pi+\xi^-}{2n}\right] F[kL^i g^+(\xi^-)] + \cot\left[\frac{\pi-\xi^-}{2n}\right] F[kL^i g^-(\xi^-)] \right\} \\ \mp \left\{ \cot\left[\frac{\pi+\xi^+}{2n}\right] F[kL^{rn} g^+(\xi^+)] + \cot\left[\frac{\pi-\xi^+}{2n}\right] F[kL^{ro} g^-(\xi^+)] \right\} \Bigg) \end{aligned} \tag{3.52}$$

where $F(x)$ is the Fresenel integral, given by

$$F(x) = 2j\sqrt{x}\, e^{jx} \int_{\sqrt{x}}^{\infty} e^{-jt^2} dt \tag{3.53}$$

$g^{\pm}(\xi) = 1 + \cos(2n\pi N^{\pm} - \xi)$, $\xi^{\pm} = \phi \pm \phi'$; $N^{\pm}$ is the positive or negative integer or zero which most nearly satisfies

$2n\pi N^{+} - \xi = +\pi$

$2n\pi N^{-} - \xi = -\pi$

n is a wedge factor given by $\gamma = (2-n)\pi$, where γ is the interior angle between the 0 face and n face of the wedge. For the present problem, $n = 2$ where the wedge has $0°$ interior angle. For the definitions of distance parameters (L^i, L^{rn}, and L^{ro}), refer to [11]. Because the intersecting surfaces forming the edges are plane surfaces, the distance parameters are equal, that is,

$$L^i = L^{ro} = L^{rn} = L \tag{3.54}$$

For far-field observations, L is given by

$$L \approx s' \qquad s \gg s' \tag{3.55}$$

where s' is the source distance to the diffracting points in the E and H planes.

3.2.2. *Edge Diffraction of Conical Horns in Free Space*

The incident field at points Q_{d1} and Q_{d2}, as shown in Fig. 3.2, is found from (3.3) and (3.4) after substituting $\theta = \pi/2$ and $r = a$; a is the radius of the horn aperture. ρ_{c1} and ρ_{c2} are determined from (3.51), and they are written as

$$\rho_{c1} = \frac{a}{\sin\theta} \quad , \quad \rho_{c2} = -\frac{a}{\sin\theta} \tag{3.56}$$

The distance parameter of (3.54) is:

$$L_1 = L_2 = a \tag{3.57}$$

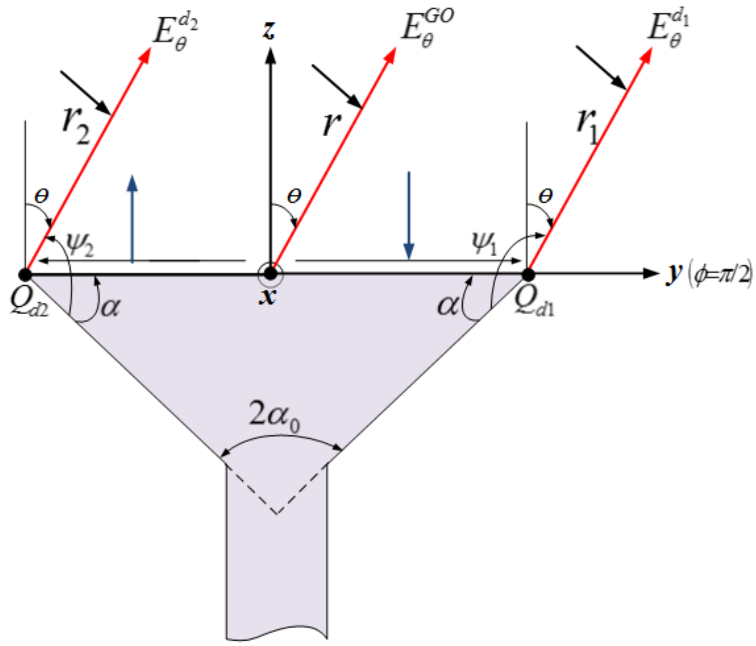

Fig. 3.2. Two-Dimensional Ray Analysis for Radiation Pattern Calculations.

The diffracted field components from diffracting points Q_{d1} and Q_{d2} are:

$$E_\theta^{d_1} = E_\theta^i\left(a, \frac{\pi}{2}, \frac{\pi}{2}\right) D^h\left(L_1, \psi_1, \alpha, \frac{\pi}{2}, 2\right) \sqrt{\rho_{c1}}\, \frac{e^{-jkr_1}}{r_1} \tag{3.58}$$

$$E_\theta^{d_2} = E_\theta^i\left(a, \frac{\pi}{2}, \frac{\pi}{2}\right) D^h\left(L_2, \psi_2, \alpha, \frac{\pi}{2}, 2\right) \sqrt{\rho_{c2}}\, \frac{e^{-jkr_2}}{r_2} \tag{3.59}$$

for the E-plane amplitude radiation pattern, and

$$E_\phi^{d_1} = E_\phi^i\left(a, \frac{\pi}{2}, 0\right) D^s\left(L_1, \psi_1, \alpha, \frac{\pi}{2}, 2\right) \sqrt{\rho_{c1}}\, \frac{e^{-jkr_1}}{r_1} \tag{3.60}$$

$$E_\phi^{d_2} = E_\phi^i\left(a, \frac{\pi}{2}, 0\right) D^s\left(L_2, \psi_2, \alpha, \frac{\pi}{2}, 2\right) \sqrt{\rho_{c2}}\, \frac{e^{-jkr_2}}{r_2} \tag{3.61}$$

for the H-plane amplitude radiation pattern.

where

$$\psi_1 = \frac{\pi}{2} + \theta + \alpha \qquad (0 \le \theta \le \pi) \tag{3.62}$$

$$\psi_2 = \begin{cases} \frac{\pi}{2} + \alpha - \theta & (0 \leq \theta \leq \frac{\pi}{2}) \\ \frac{5\pi}{2} + \alpha - \theta & (\frac{\pi}{2} < \theta \leq \pi) \end{cases} \tag{3.63}$$

For far-field observations

$$r_1 \simeq r - a\cos\left(\frac{\pi}{2} - \theta\right) = r - a\sin\theta \tag{3.64}$$

$$r_2 \simeq r + a\cos\left(\frac{\pi}{2} - \theta\right) = r + a\sin\theta \tag{3.65}$$

for phase terms, and

$$r_1 \simeq r_2 \simeq r \tag{3.66}$$

for amplitude terms.

Therefore the diffracted fields from the diffracting points Q_{d1} and Q_{d2} reduce to

$$E_\theta^{d_1} = E_\theta^i\left(a, \frac{\pi}{2}, \frac{\pi}{2}\right) D^h\left(L_1, \psi_1, \alpha, \frac{\pi}{2}, 2\right) \sqrt{\rho_{c1}}\, e^{+ja\sin\theta}\, \frac{e^{-jkr}}{r} \tag{3.67}$$

$$E_\theta^{d_2} = E_\theta^i\left(a, \frac{\pi}{2}, \frac{\pi}{2}\right) D^h\left(L_2, \psi_2, \alpha, \frac{\pi}{2}, 2\right) \sqrt{\rho_{c2}}\, e^{-ja\sin\theta}\, \frac{e^{-jkr}}{r} \tag{3.68}$$

for the far-zone E-plane amplitude radiation pattern, and

$$E_\phi^{d_1} = E_\phi^i\left(a, \frac{\pi}{2}, 0\right) D^s\left(L_1, \psi_1, \alpha, \frac{\pi}{2}, 2\right) \sqrt{\rho_{c1}}\, e^{+ja\sin\theta}\, \frac{e^{-jkr}}{r} \tag{3.69}$$

$$E_\phi^{d_2} = E_\phi^i\left(a, \frac{\pi}{2}, 0\right) D^s\left(L_2, \psi_2, \alpha, \frac{\pi}{2}, 2\right) \sqrt{\rho_{c2}}\, e^{-ja\sin\theta}\, \frac{e^{-jkr}}{r} \tag{3.70}$$

for the far-zone H-plane amplitude radiation pattern.

Due to the circular symmetry of the aperture's edge, the edge behaves as a continuous ring radiator which leads to the formation of a caustic. Therefore, a caustic correction is needed for angles at and near the axis of the antenna. The UTD can be used to correct for this caustic. Ryan and Peters [31] showed that UTD equivalent currents can be used to correct for this caustic. Using this method, equivalent magnetic and electric currents are created along the edge of the aperture. Then radiation integrals are used to obtain fields due to these currents, which correct the diffracted fields at and near the symmetry axis of the antenna. The electric and magnetic equivalent currents take the form of

$$I_{\phi}^{e} = -\frac{\sqrt{8\pi k}}{\eta k} e^{-j\pi/4} D^{s} E_{\phi}^{i}(Q_d) \tag{3.71}$$

$$I_{\phi}^{m} = -\frac{\sqrt{8\pi k}}{k} e^{-j\pi/4} D^{h} E_{\theta}^{i}(Q_d) \tag{3.72}$$

The fields radiated by each of the equivalent currents can be obtained using techniques of Chapter 5 of [1]. Thus the radiated field for a loop carrying an electric current I^e are given by

$$E_{\theta}^{e} = -\frac{j\omega\mu a}{4\pi r} \cos\theta e^{-jkr} \int_0^{2\pi} I^e(\phi') \sin(\phi-\phi') e^{jka\cos(\phi-\phi')\sin\theta} d\phi' \tag{3.73}$$

$$E_{\phi}^{e} = -\frac{j\omega\mu a}{4\pi r} e^{-jkr} \int_0^{2\pi} I^e(\phi') \cos(\phi-\phi') e^{jka\cos(\phi-\phi')\sin\theta} d\phi' \tag{3.74}$$

The duality theorem can be applied to obtain the fields radiated by a magnetic current I^m , rather than an electric current I^e, with the result being

$$E_{\theta}^{m} = -\eta \frac{j\omega\varepsilon a}{4\pi r} e^{-jkr} \int_0^{2\pi} I^m(\phi') \cos(\phi-\phi') e^{jka\cos(\phi-\phi')\sin\theta} d\phi' \tag{3.75}$$

$$E_{\phi}^{m} = \eta \frac{j\omega\varepsilon a}{4\pi r} \cos\theta e^{-jkr} \int_0^{2\pi} I^m(\phi') \sin(\phi-\phi') e^{jka\cos(\phi-\phi')\sin\theta} d\phi' \tag{3.76}$$

Now, by numerically integrating (3.75)-(3.76), corrected diffracted fields are obtained at and near the caustic.

3.2.3. *Edge Diffraction of Aperture Antennas Mounted on Finite Ground Planes*

In this section, two geometries, circular aperture antennas mounted on circular and square ground planes, are treated similarly, and they are calculated analytically following the same procedure as described previously in the free space case. Far-zone E-plane and H-plane amplitude patterns are calculated for the circular and square ground planes. Also, it should be noted that since the incident field is at grazing incidence, the total GO field is multiplied by a factor of 1/2 [1], [11]. The incident field at points Q_{d1} and Q_{d2}, as shown in Fig. 3.3, is found from (3.7) and (3.8) for the conical horn antenna and from (3.48) and (3.49) for the circular waveguide after substituting $\theta = \pi/2$ and $r = d$; d is the radius of the circular ground plane or the half width of the square ground plane. ρ_{c1} and ρ_{c2} are found from (3.51). For a circular aperture antenna mounted on a circular ground plane:

$$\rho_{c1} = \frac{d}{\sin\theta} \tag{3.77}$$

$$\rho_{c2} = -\frac{d}{\sin\theta} \tag{3.78}$$

and for the square ground plane:

$$\rho_{c1} = \rho_{c2} = d \tag{3.79}$$

The distance parameter L of (3.54) is the same for both the circular and square ground planes:

$$L_1 = L_2 = d \tag{3.80}$$

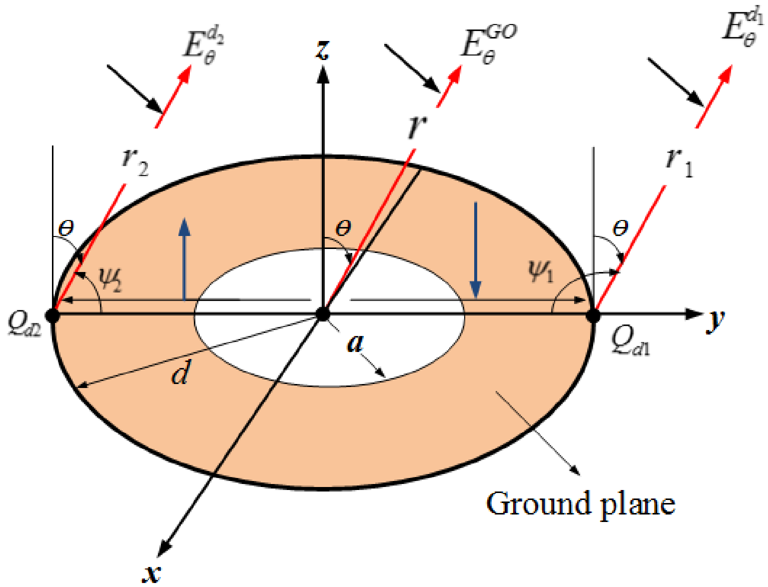

(a) Circular ground plane.

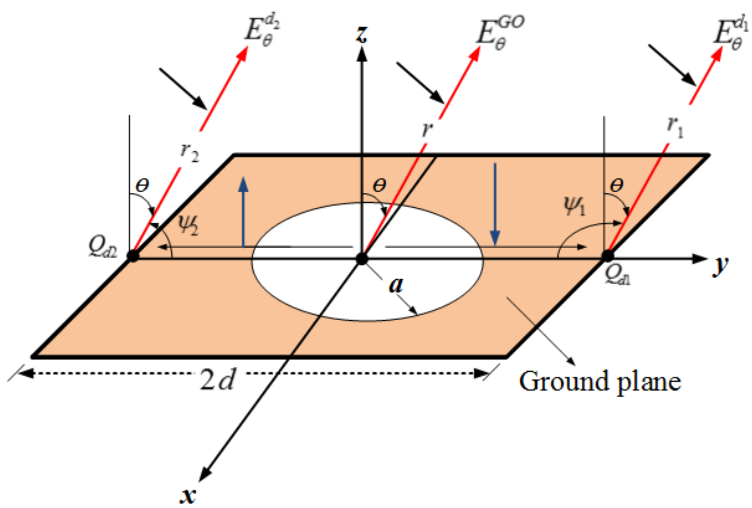

(b) Square ground plane.

Fig. 3.3. Diffraction Mechanism by Edges of Ground Planes.

The diffracted field components from diffracting points Q_{d1} and Q_{d2} , for either the square or the circular ground planes, are:

$$E_\theta^{d_1} = \frac{1}{2} E_\theta^i \left(d, \frac{\pi}{2}, \frac{\pi}{2} \right) D^h \left(L_1, \psi_1, 0, \frac{\pi}{2}, 2 \right) \sqrt{\rho_{c1}} \frac{e^{-jkr_1}}{r_1} \tag{3.81}$$

$$E_\theta^{d_2} = \frac{1}{2}E_\theta^i\left(d, \frac{\pi}{2}, \frac{\pi}{2}\right)D^h\left(L_2, \psi_2, 0, \frac{\pi}{2}, 2\right)\sqrt{\rho_{c2}}\,\frac{e^{-jkr_2}}{r_2} \tag{3.82}$$

for the E-plane diffracted field, and

$$E_\phi^{d_1} = \frac{1}{2}E_\phi^i\left(d, \frac{\pi}{2}, 0\right)D^s\left(L_1, \psi_1, 0, \frac{\pi}{2}, 2\right)\sqrt{\rho_{c1}}\,\frac{e^{-jkr_1}}{r_1} \tag{3.83}$$

$$E_\phi^{d_2} = \frac{1}{2}E_\phi^i\left(d, \frac{\pi}{2}, 0\right)D^s\left(L_2, \psi_2, 0, \frac{\pi}{2}, 2\right)\sqrt{\rho_{c2}}\,\frac{e^{-jkr_2}}{r_2} \tag{3.84}$$

for the H-plane diffracted field.

where

$$\psi_1 = \frac{\pi}{2} + \theta \qquad (0 \leq \theta \leq \pi) \tag{3.85}$$

$$\psi_2 = \begin{cases} \frac{\pi}{2} - \theta & (0 \leq \theta \leq \frac{\pi}{2}) \\ \frac{5\pi}{2} - \theta & (\frac{\pi}{2} < \theta \leq \pi) \end{cases} \tag{3.86}$$

For far-field observations

$$r_1 \simeq r - d\cos\left(\frac{\pi}{2} - \theta\right) = r - d\sin\theta \tag{3.87}$$

$$r_2 \simeq r + d\cos\left(\frac{\pi}{2} - \theta\right) = r + d\sin\theta \tag{3.88}$$

for phase terms, and

$$r_1 \simeq r_2 \simeq r \tag{3.89}$$

for amplitude terms.

Then the diffracted fields from the diffracting points Q_{d1} and Q_{d2} reduce to

$$E_\theta^{d_1} = \frac{1}{2}E_\theta^i\left(d, \frac{\pi}{2}, \frac{\pi}{2}\right)D^h\left(L_1, \psi_1, 0, \frac{\pi}{2}, 2\right)\sqrt{\rho_{c1}}\,e^{+jd\sin\theta}\,\frac{e^{-jkr}}{r} \tag{3.90}$$

$$E_\theta^{d_2} = \frac{1}{2}E_\theta^i\left(d, \frac{\pi}{2}, \frac{\pi}{2}\right)D^h\left(L_2, \psi_2, 0, \frac{\pi}{2}, 2\right)\sqrt{\rho_{c2}}\,e^{-jd\sin\theta}\,\frac{e^{-jkr}}{r} \tag{3.91}$$

for the far-zone E plane, and

$$E_{\phi}^{d_1} = \frac{1}{2} E_{\phi}^{i}\left(d, \frac{\pi}{2}, 0\right) D^{s}\left(L_1, \psi_1, 0, \frac{\pi}{2}, 2\right) \sqrt{\rho_{c1}}\, e^{+jd\sin\theta}\, \frac{e^{-jkr}}{r} \tag{3.92}$$

$$E_{\phi}^{d_2} = \frac{1}{2} E_{\phi}^{i}\left(d, \frac{\pi}{2}, 0\right) D^{s}\left(L_2, \psi_2, 0, \frac{\pi}{2}, 2\right) \sqrt{\rho_{c2}}\, e^{-jd\sin\theta}\, \frac{e^{-jkr}}{r} \tag{3.93}$$

for the far-zone H plane.

So far, the diffraction effects are accounted for by using only the diffraction which depends on the incident field. However, this indicates that the diffracted field would be zero if the incident field is zero. Physically, the diffracted fields do not go to zero. Thus a second-order diffraction, due to the rapid change of GO field near the edge, can be incorporated into the analysis. In the H plane for the circular and square ground planes, for grazing incidence, higher order term in the asymptotic solution must be considered. Otherwise, the diffracted fields are zero, which leads to large discontinuities in the pattern. The first-order diffracted fields are zero because the electric field on the surface of a conducting wedge vanishes for a grazing incident wave. Therefore, the slope diffracted fields, second-order diffracted fields, from the diffraction points are given by [11]

$$E_{\theta}^{slope} = \frac{1}{jk}\left[\frac{\partial E_{\theta}^{i}(Q_d)}{\partial n}\right]\left(\frac{\partial D^{h}}{\partial \phi'}\right)\sqrt{\frac{\rho_c}{s(\rho_c + s)}}\, e^{-jks} \tag{3.94}$$

$$E_{\phi}^{slope} = \frac{1}{jk}\left[\frac{\partial E_{\phi}^{i}(Q_d)}{\partial n}\right]\left(\frac{\partial D^{s}}{\partial \phi'}\right)\sqrt{\frac{\rho_c}{s(\rho_c + s)}}\, e^{-jks} \tag{3.95}$$

where

$$\left.\frac{\partial E_{\theta}^{i}}{\partial n}\right|_{Q_d} = \hat{n}.\nabla E_{\theta}^{i}\Big|_{Q_d} = -\frac{1}{s'}\left.\frac{\partial E_{\theta}^{i}}{\partial \phi'}\right|_{Q_d} = \text{slope of incident field for hard polarization.}$$

$$\left.\frac{\partial E^i_\phi}{\partial n}\right|_{Q_d} = \hat{n}.\nabla E^i_\phi\Big|_{Q_d} = -\frac{1}{s'}\left.\frac{\partial E^i_\phi}{\partial \phi'}\right|_{Q_d} = \text{slope of incident field for soft polarization.}$$

$\hat{n}$ is unit normal in ϕ' direction.

s' is the distance from the aperture center to the diffraction point.

$\frac{\partial D^{h,s}}{\partial \phi'}$ = slope diffraction coefficient for hard and soft polarization, respectively, given by

$$\begin{aligned}D^{s,h}_{slope} = \frac{-e^{-j\pi/4}}{2n^2\sqrt{2\pi k}\sin\beta_0'}\Bigg(\Bigg\{ & \csc^2\left[\frac{\pi+\xi^-}{2n}\right]F_s[kLg^+(\xi^-)] \\ & -\csc^2\left[\frac{\pi-\xi^-}{2n}\right]F_s[kLg^-(\xi^-)]\Bigg\} \\ & \pm\Bigg\{\csc^2\left[\frac{\pi+\xi^+}{2n}\right]F_s[kLg^+(\xi^+)] \\ & -\csc^2\left[\frac{\pi-\xi^+}{2n}\right]F_s[kLg^-(\xi^+)]\Bigg\}\Bigg) \end{aligned} \quad (3.96)$$

where

$$F_s(x) = 2jx[1-F(x)] \quad (3.97)$$

and $F(x)$ is presented by (3.53).

For circular ground planes, as mentioned before, the edge behaves as a continuous ring radiator which in turn leads to the formation of a caustic, where the diffracted fields are infinity. Therefore, a caustic correction is needed for angles at and near the axis of the antenna. Equivalent magnetic and electric currents are created along the edge of the circular ground plane by using this method. Then, radiation integrals are used to obtain fields due to these currents which correct the diffracted fields at and near the axial caustic. The electric and magnetic equivalent currents are calculated by using (3.73)-(3.76).

The electric current is zero because the ϕ component of the incident electric field (GO field) is zero at the edge. Therefore, the radiated field due to the electric current is zero. The corrected diffracted fields in the E and H planes due to a magnetic current around the ground edge are obtained at and near the caustic by solving numerically (3.75)-(3.76).

For the square ground plane, the slope diffraction does not significantly improve the radiation pattern in the backlobe region of the H-plane amplitude radiation pattern. However, one needs to include the contributions from the E-plane edge diffractions because the E-plane edge diffraction has a much greater magnitude than that of the H-plane edge diffraction. This contribution can be calculated by using an equivalent currents method that was described previously.

3.3. Validation

All the measurements were performed in the ElectroMagnetic Anechoic Chamber (EMAC) facility at Arizona State University. Computer programs were written in Matlab to calculate the normalized far-zone field amplitude patterns in the E and H planes for all the cases examined in this work. In addition, HFSS simulations were performed.

3.3.1. *Conical Horn Antennas in Free Space*

The far-zone E- and H-plane amplitude patterns of conical horns of arbitrary flare angles, excited by the TE_{11}-mode circular waveguide, are obtained by employing geometrical optics and the uniform theory of diffraction methods. Validity of the amplitude pattern analysis over the main beam, the near and far sidelobes, and back lobe presented in previous sections has been verified by calculating the far-zone E- and H-plane amplitude patterns of commercial X- and C-band conical horns. The analytical results are compared with measurements and HFSS simulations. The resulting patterns, over a dynamic range of 80 dB, are shown in Figs. 3.4-3.7.

The agreement between theory, experiment, and HFSS simulation is good in the E and H planes for the X- and C-band horns, having a total flare angle of 35° and 23°and an axial length $L = 7.148\lambda$ and $L = 3.724\lambda$, respectively, as shown in Figs. 3.4-3.7. Although the complex back structure of the antenna is not considered in the UTD analysis, a fairly good agrement is found between the amplitude patterns over the main beam, near and far sidelobes, and back lobe.

For the measurements, a waveguide (rectangular-to-circular waveguide transition) and an adaptor were used to connect the conical horns to a coaxial RF cable. In the diffraction modeling of the horn using the UTD, the feed structures shown in Fig. 3.8, due to their complex geometries, were not taken into account. However, these structures become integral parts of the overall structure and significantly distort the pattern, especially in the back region. Including these structures in the UTD modeling is not an easy task, and they create more computational problems and deficiencies which cannot easily be simulated with UTD. Therefore, to calculate their impact on the radiation characteristics of the conical horns, HFSS was used to simulate the back feeding structures. As indicated in Figs. 3.4-3.7, very good agreement was attained between the measurements and HFSS simulations which incorporate the complex feeding structures. This demonstrates that the back feed structures are responsible for the deviations between the measurements and UTD results.

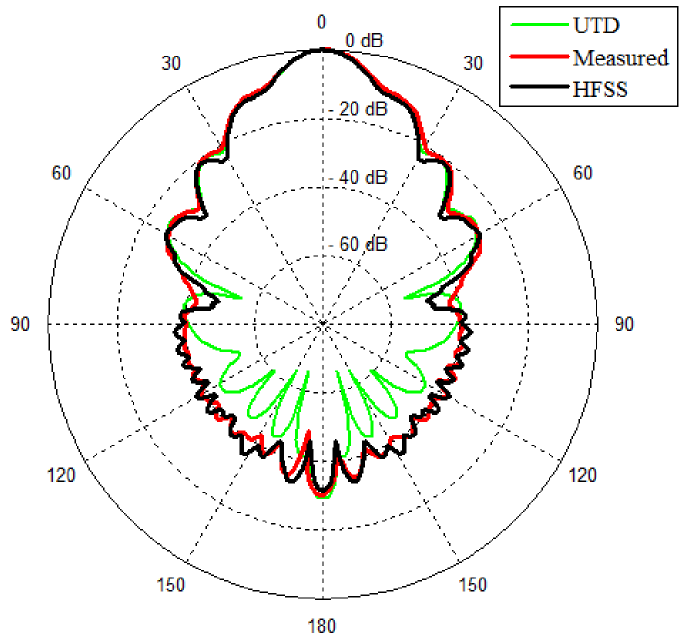

Fig. 3.4. Far-Zone E-Plane Amplitude Patterns of an X-Band Conical Horn Antenna at 10.3 GHz ($L = 7.148\lambda$, $2\alpha_0 = 35°$).

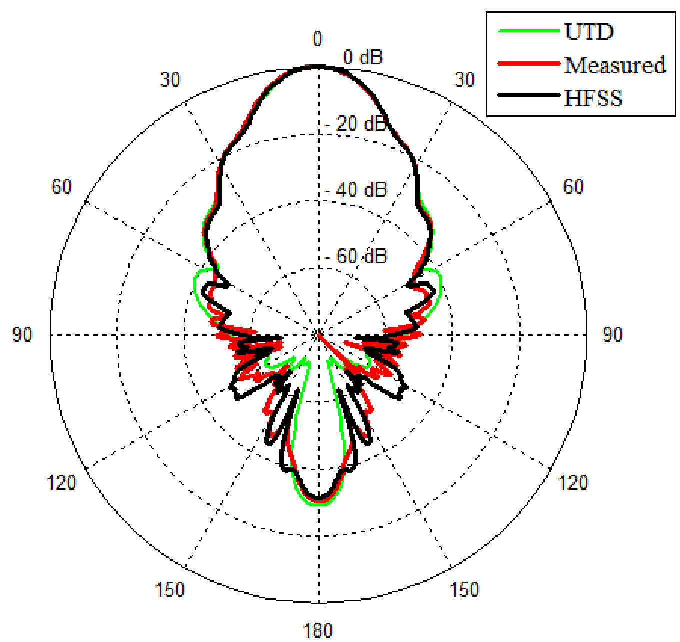

Fig. 3.5. Far-Zone H-Plane Amplitude Patterns of an X-Band Conical Horn Antenna at 10.3 GHz ($L = 7.148\lambda$, $2\alpha_0 = 35°$).

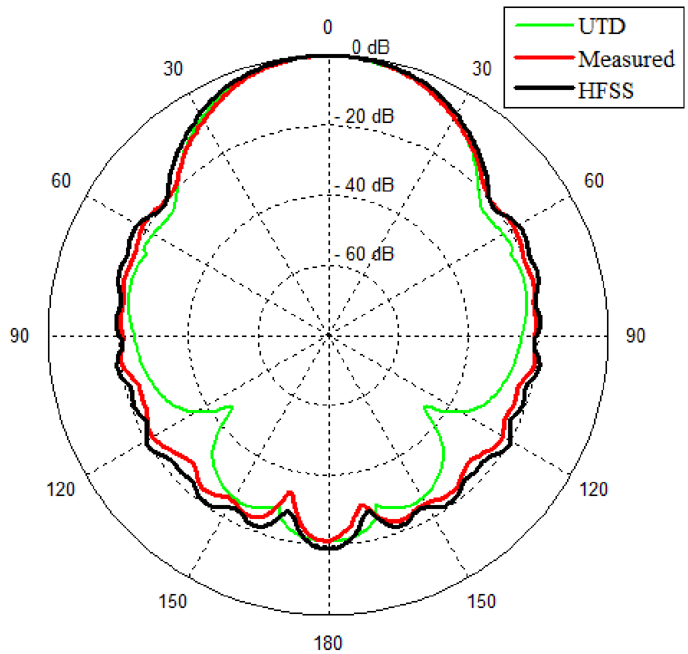

Fig. 3.6. Far-Zone E-Plane Amplitude Patterns of a C-Band Conical Horn Antenna at 4.9 GHz ($L = 3.724\lambda$, $2\alpha_0 = 23°$).

For both antennas, the amplitude patterns in the E-plane is more broad than those in the H-plane. Also the diffraction in the back region for the X-band horn is less than that of the C-band horn because of its higher directivity. The more directivity the horn has, like the X-band horn, the less diffraction will exist in the back region especially at and near the antenna axis.

3.3.2. *Conical Horn Antennas Mounted on Square and Circular Ground Planes*

Models for the circular and square ground planes, with a conical horn antenna mounted at the center, have been constructed. The width of the square ground plane and diameter of the circular ground plane are 25.2 in. for the C-band. For the X-band antenna, the width

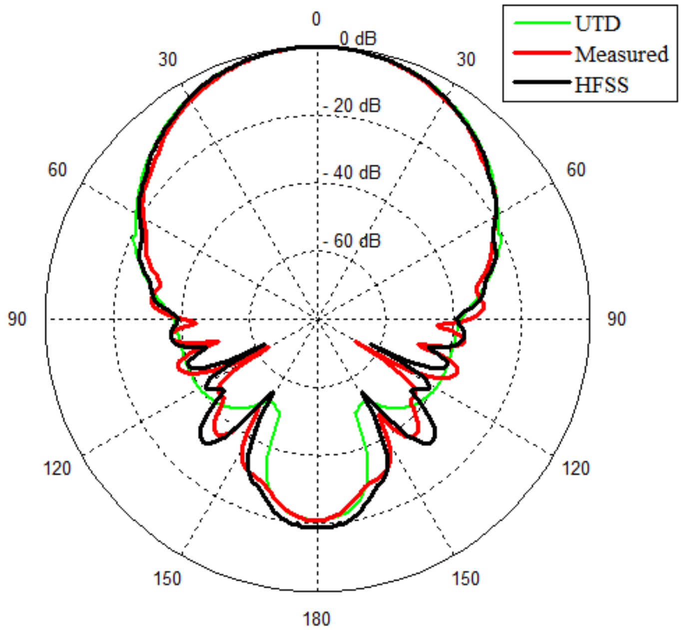

Fig. 3.7. Far-Zone H-Plane Amplitude Patterns of a C-Band Conical Horn Antenna at 4.9 GHz ($L = 3.724\lambda$, $2\alpha_0 = 23°$).

of the square ground plane and diameter of the circular ground plane are 12.2 in.. The ground planes are made of aluminum. Validity of the radiation pattern analysis over the main beam, the near and far sidelobes, and back lobe presented above has been verified by calculating the far-zone E- and H-plane amplitude patterns of commercial X- and C-band conical horns. The frequencies at which the measurements were preformed are 4.9 GHz and 10.3 GHz. The diameters of the horn apertures are 5.36 in. and 3.708 in. of the X-band and C-band, respectively. The diameters of the waveguides (used for the measurements and HFSS simulations) are 0.9 in. and 1.918 in. of the X-band and C-band, respectively. Analytical and measured data are compared with simulated data based on Ansoft's High Frequency Structure Simulator (HFSS).

(a) (b)

Fig. 3.8. Photographs of (a) C-Band, and (b) X-Band Conical Horns.

Figs. 3.9 and 3.10 display, respectively, the far-zone E-plane amplitude patterns of the X-band and C-band horn antennas mounted on the square and circular ground planes. Very good agreement between theory, experiment and simulation is indicated; the total fields consist of the GO (3.7), and first-order diffracted fields (3.90) and (3.91). In addition, the fields associated with the equivalent currents of (3.73) and (3.75) are included for the circular ground planes.

The far-zone H-plane amplitude patterns of the X-band and C-band horn antennas mounted on the square and circular ground planes are, respectively, shown in figs. 3.11 and 3.12. The results of experiments and HFSS simulations show a good agreement with the theoretical calculations. The total analytical fields consist of the GO (3.8), first-order diffracted (3.92) and (3.93), and slope diffracted fields (3.95). In the backlobe region of the H-plane pattern of antennas mounted on the square ground planes, the contributions from the E-plane edge diffractions are included because the E-plane edge diffraction has a significant effect (more than that of the H-plane edge slope diffraction), as shown in Fig. 3.13. In addition, the fields associated with the equivalent currents of (3.74) and (3.76) are included for the circular ground planes.

The H-plane electric field component of the incident field vanishes along the ground plane edge (grazing incidence). Thus, only diffraction by the E-plane edges contributes significantly to the E- and H-plane diffraction patterns. To obtain the far-zone E-plane amplitude pattern, only the diffraction from the midpoints of the E-plane edge contributes to the amplitude pattern. For the far-zone H-plane amplitude pattern, diffraction accruing at all points along the E-plane edge, non-normal and normal incidence of the incident GO fields at the edge, must be taken into consideration.

The discrepancies between the theoretical and measured results in the backward region of the far-zone E- and H-plane amplitude patterns can be attributed to the inability to accurately model the structure feeding the horn as well as the structure used to support the antenna during the measurement. These discrepancies are more significant for the horns in free space as shown in the previous section.

As mentioned, the amplitude patterns in the E-plane are broader than those in the H-plane. Also the diffraction in the back region for the X-band horn is less than that of the C-band horn because of the directivity.

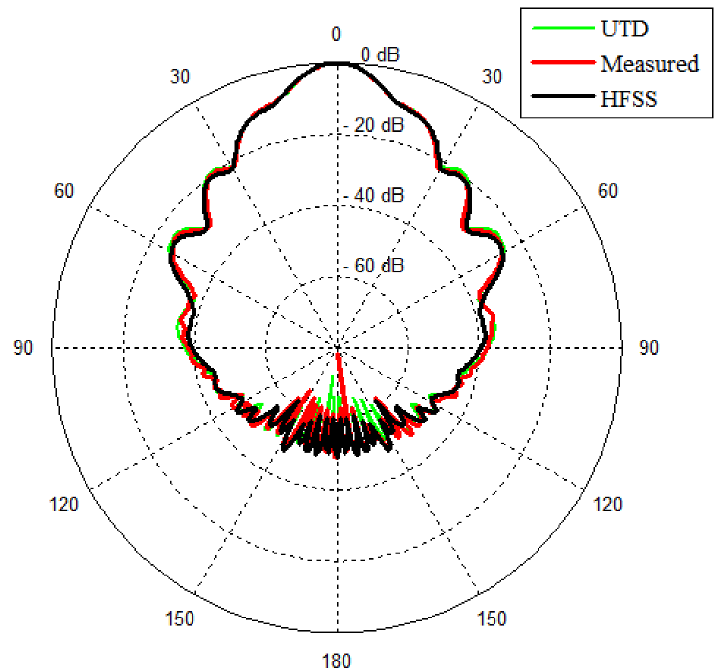

(a) X-Band Conical Horn Antenna at 10.3 GHz.

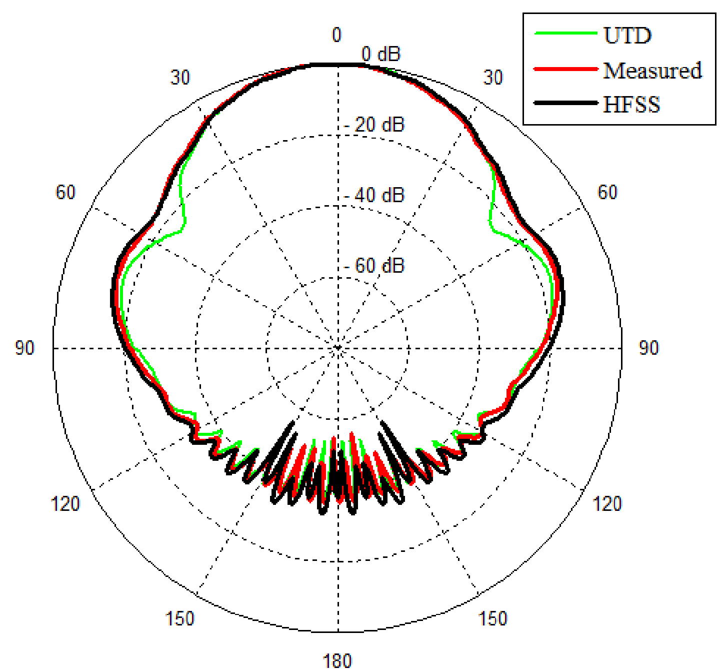

(b) C-Band Conical Horn Antenna at 4.9 GHz.

Fig. 3.9. Far-Zone E-Plane Amplitude Patterns of Conical Horn Antennas Mounted on Square Ground Planes.

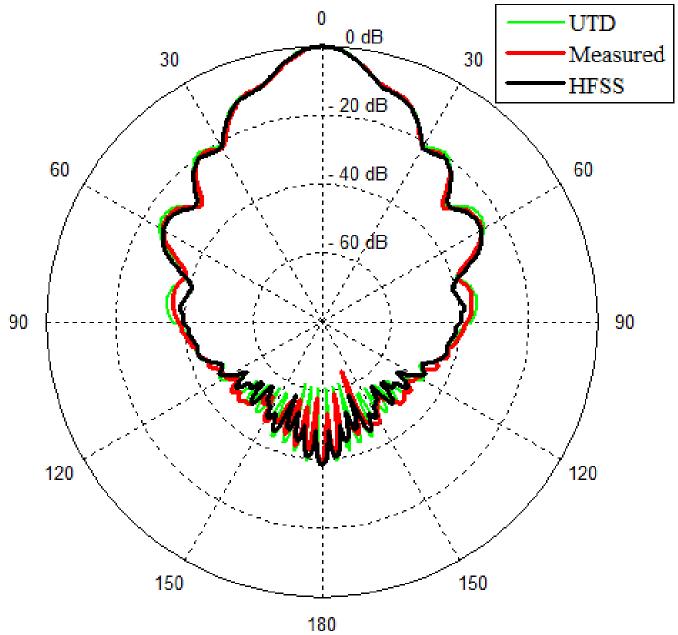

(a) X-Band Conical Horn Antenna at 10.3 GHz.

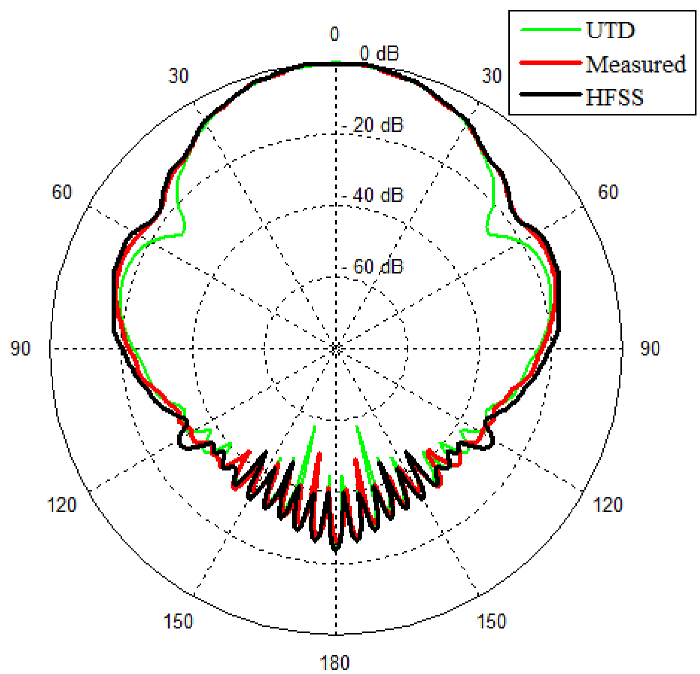

(b) C-Band Conical Horn Antenna at 4.9 GHz.

Fig. 3.10. Far-Zone E-Plane Amplitude Patterns of Conical Horn Antennas Mounted on Circular Ground Planes.

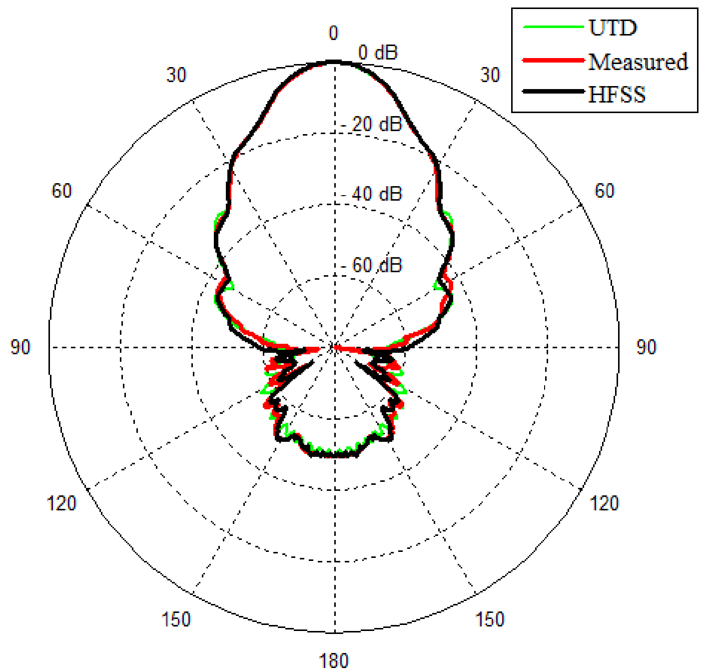

(a) X-Band Conical Horn Antenna at 10.3 GHz.

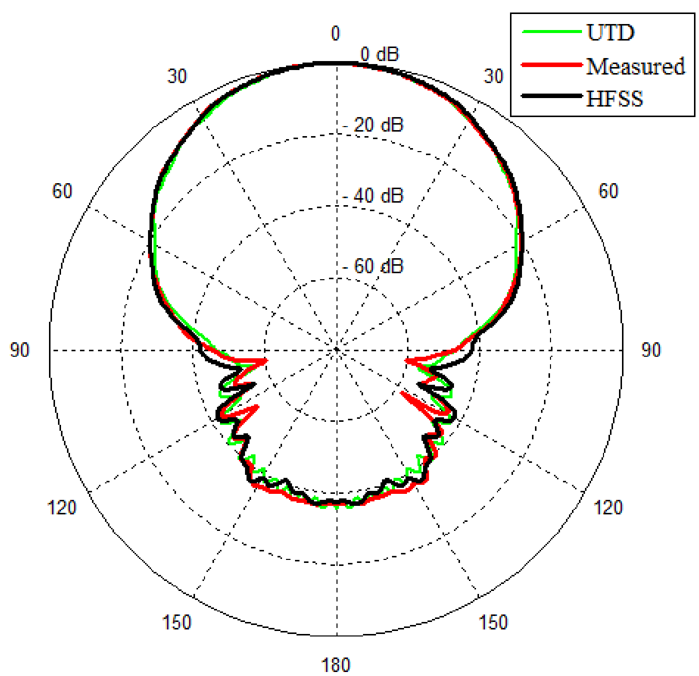

(b) C-Band Conical Horn Antenna at 4.9 GHz.

Fig. 3.11. Far-Zone H-Plane Amplitude Patterns of Conical Horn Antennas Mounted on Square Ground Planes.

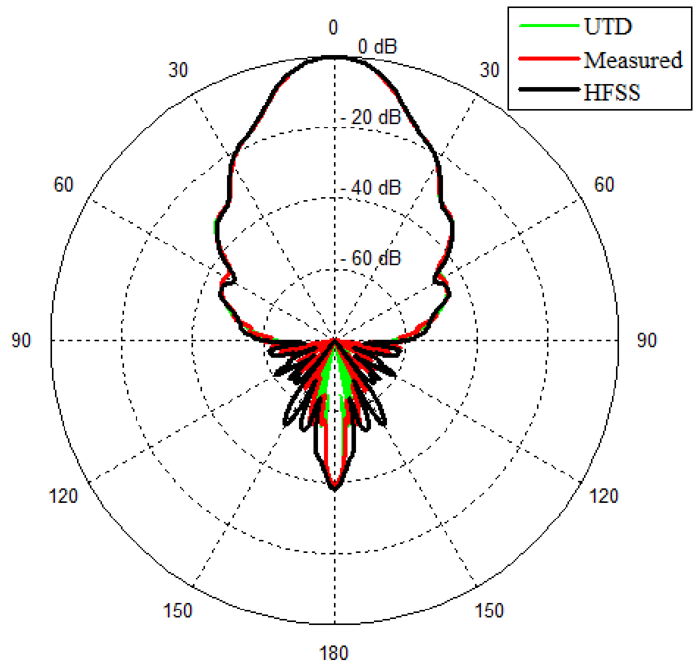

(a) X-Band Conical Horn Antenna at 10.3 GHz.

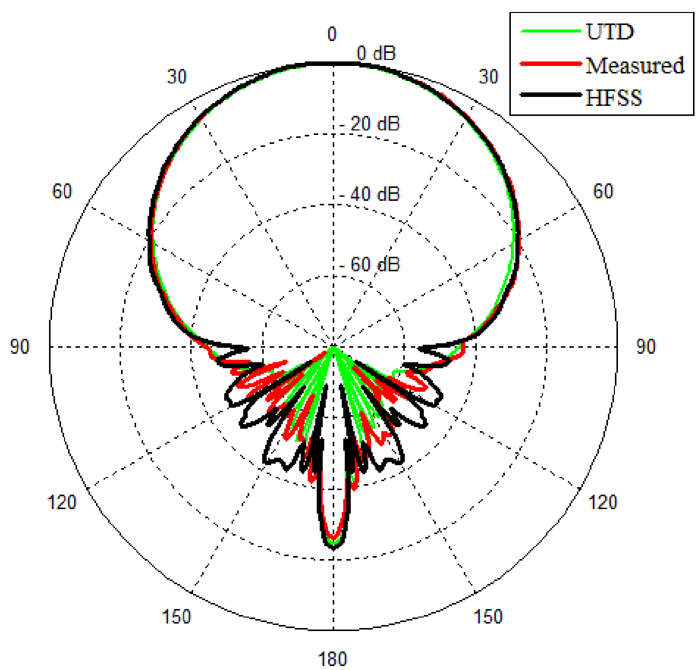

(b) C-Band Conical Horn Antenna at 4.9 GHz.

Fig. 3.12. Far-Zone H-Plane Amplitude Patterns of Conical Horn Antennas Mounted on Circular Ground Planes.

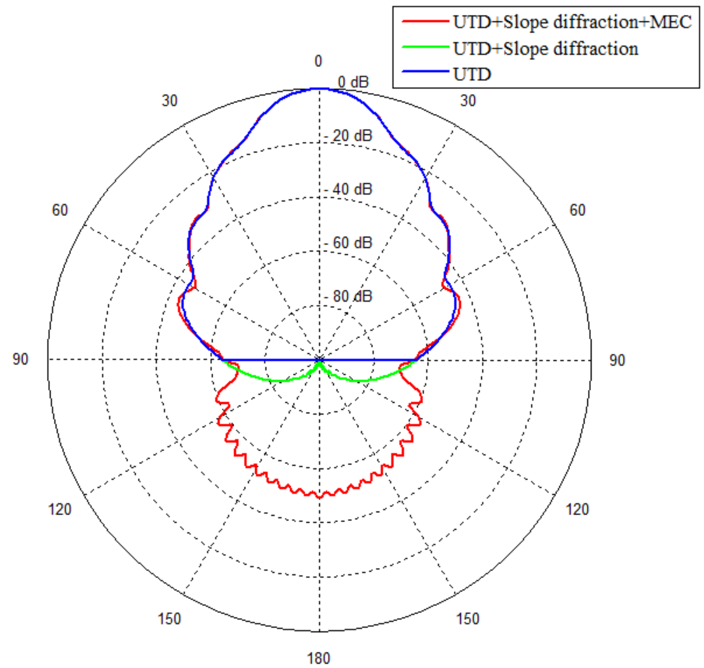

(a) X-Band Conical Horn Antenna at 10.3 GHz.

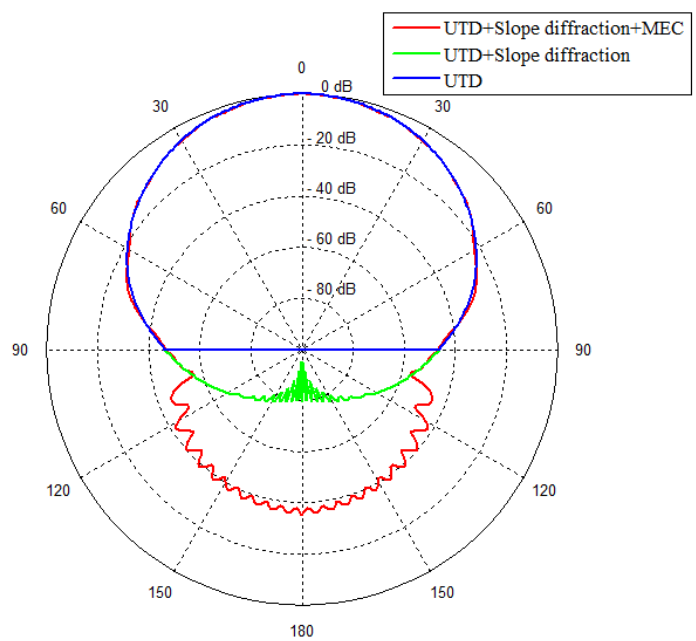

(b) C-Band Conical Horn Antenna at 4.9 GHz.

Fig. 3.13. Far-Zone H-Plane Amplitude Patterns of a Conical Horn Antenna Mounted a Square Ground Plane: UTD, Slope Diffraction, and MEC.

The ripples in the amplitude patterns, especially in the backlobe region, are attributed to the edge diffractions. The ripples shown in the patterns are due to the constructive and destructive interference of the diffractions from the diametrically opposite diffraction points. In the E-plane, these ripples are more significant because the incident electric field at the point of diffraction is more intense in this plane than in the H plane for the X-band horn. However, for the C-band horn, the edge diffractions have less impact on the amplitude patterns in the forward region because of the broadness and strength of the geometrical optics fields in the region.

Although the side of the square is equal to the diameter of the circular, it is very clear from the patterns of Figs. 3.9-3.12 that the E- and H-plane amplitude patterns of the circular ground plane are greater than those of the square ground plane at and near the antenna axis ($\theta = 180°$). This is due to the ring radiator which contributes about an additional 10-13 dB.

3.3.3. *Circular Waveguides Mounted on Square and Circular Ground Planes*

The circular and square ground planes with the circular waveguide mounted at the center have been constructed. The aperture antenna has been excited by the TE_{11}-mode circular waveguide. The width of the square ground plane and diameter of the circular ground plane are 12 in.. The ground planes are made of aluminum. Validity of the radiation pattern analysis over the main beam and the near and far sidelobes presented above has been verified by calculating the far-zone E- and H-plane amplitude patterns of the aperture antennas. The frequency at which the measurements were performed was 10 GHz. The diameter of the aperture is 0.938 in.. Numerical and measured data are compared with simulated data based on Ansoft's High Frequency Structure Simulator (HFSS).

Figs. 3.14 and 3.15 show the far-zone E-plane amplitude patterns of antennas mounted on the square and circular ground planes, respectively. The agreement between the theoretical analysis, experimental, and HFSS-simulated results is very good. The total fields consist of the GO (3.48), and first-order diffracted fields (3.90) and (3.91). In addition, the fields associated with the equivalent currents of (3.73) and (3.75) are included for the circular ground planes.

The far-zone H-plane amplitude patterns of antennas mounted on the square and circular ground planes, respectively, are shown in Figs. 3.16 and 3.17. Very good agreement between theory, experiment and simulation is observed; the total fields consist of the GO (3.49), first-order diffracted (3.92) and (3.93), slope diffracted fields (3.95).

In the backlobe region of the H-plane pattern of antennas mounted on the square ground planes, the contributions from the E-plane edge diffractions are included because the E-plane edge diffraction has a significant effect - more than that of the H-plane edge slope diffraction. Also, the fields associated with the equivalent currents of (3.74) and (3.76) are included for the circular ground planes.

Comparing to the conical horn antenna in the previous section, the amplitude patterns in the E and H planes of the circular waveguide are broader because the circular waveguide has a low directivity.

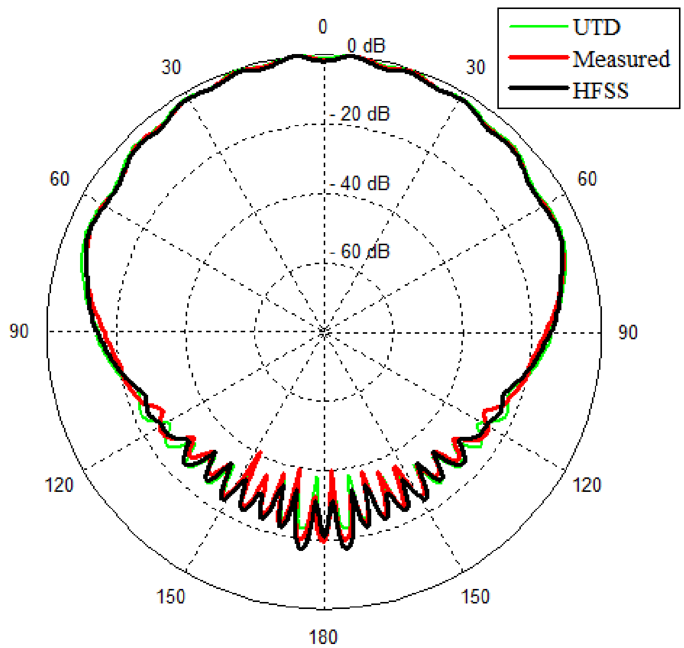

Fig. 3.14. Far-Zone E-Plane Amplitude Patterns of a Circular Waveguide Mounted on a Circular Ground Plane at 10 GHz ($a = 0.397\lambda$, $2d = 10.16\lambda$).

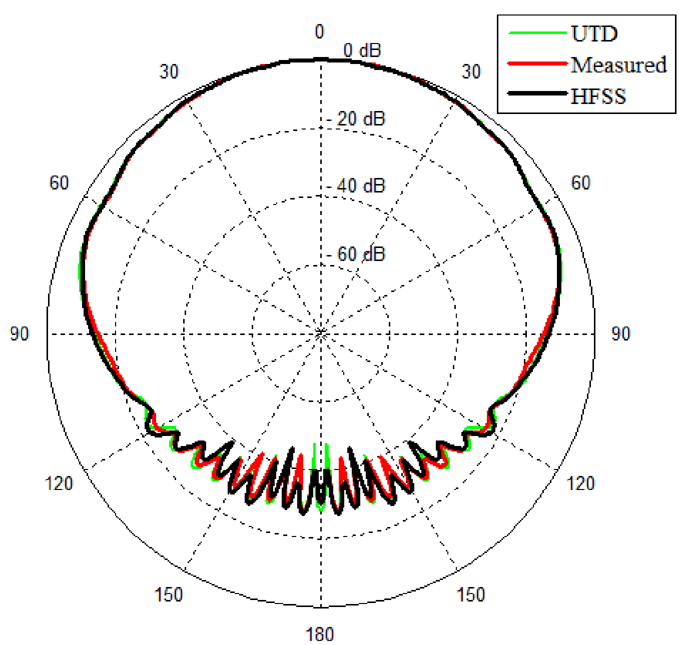

Fig. 3.15. Far-Zone E-Plane Amplitude Patterns of a Circular Waveguide Mounted on a Square Ground Plane at 10 GHz ($a = 0.397\lambda$, $2d = 10.16\lambda$).

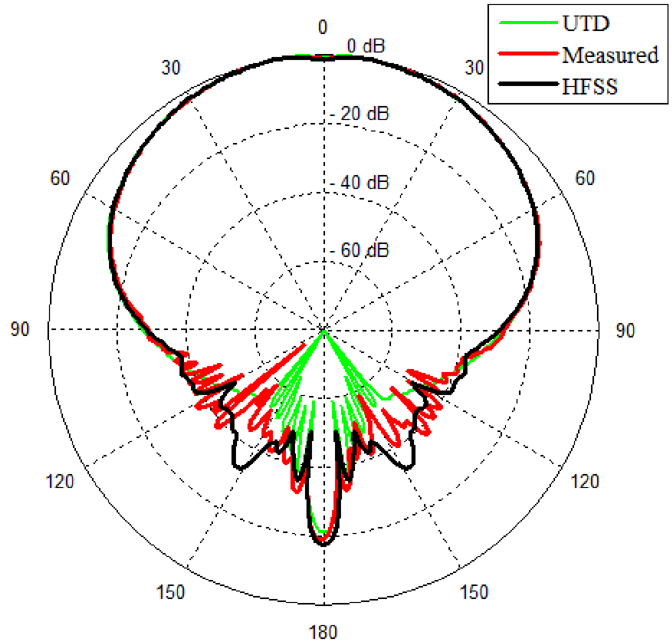

Fig. 3.16. Far-Zone H-Plane Amplitude Patterns of a Circular Waveguide Mounted on a Circular Ground Plane at 10 GHz ($a = 0.397\lambda$, $2d = 10.16\lambda$).

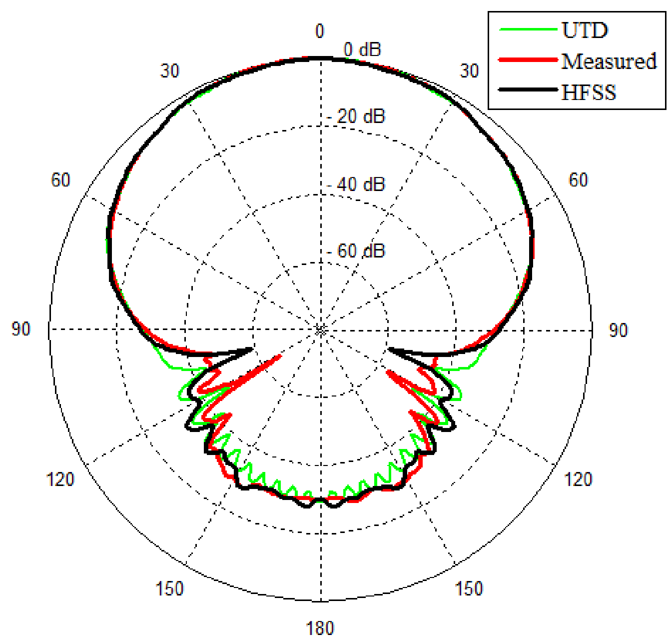

Fig. 3.17. Far-Zone H-Plane Amplitude Patterns of a Circular Waveguide Mounted on a Square Ground Plane at 10 GHz ($a = 0.397\lambda$, $2d = 10.16\lambda$).

CHAPTER 4

COATED APERTURE ANTENNAS

In this part of the work, the impact of finite coated ground plane edge diffractions on the amplitude patterns of circular aperture antennas is investigated. A model based upon the uniform theory of diffraction for an impedance wedge and the geometrical optics method is presented to calculate the amplitude patterns of a circular aperture antenna mounted on square and circular finite ground planes that are coated with a lossy dielectric on one face. The diffracted fields and the geometrical optics fields for a dielectric-covered PEC plane are vectorially combined to determine far-zone amplitude patterns in the E and H planes. The model is validated by comparisons with experimental results and those simulated by Ansoft's High Frequency Structure Simulator (HFSS).

4.1. Introduction

Aperture antennas are most commonly used at microwave frequencies in many applications, both aerospace and ground based. They are very practical for space applications where they can be conveniently integrated into the surface of the spacecraft or aircraft without affecting its aerodynamic profile, which is very critical in high-speed applications. Their openings can usually be covered with a dielectric material to protect them from environmental conditions [1], [2]. An investigation of the effect of finite coated ground planes on aperture antenna performance will aid in understanding the full-scale antenna when it is placed in more complex structures.

The uniform theory of diffraction, extended for impedance wedges, is utilized with the geometrical optics method to calculate the amplitude patterns of a circular waveguide antenna mounted on square and circular finite ground planes which are coated with a lossy dielectric on one face. A modal technique is used to calculate the electric field distribution over the antenna aperture. After the field distribution over the antenna aperture is obtained, the GO field can be easily calculated while considering the dialectic cover by using the spectral domain method. Then, UTD is employed to account for the diffracted fields from the coated ground plane edges.

A very detailed modeling of the radiation mechanism of the circular aperture antennas mounted on finite coated square and circular ground planes is developed based on geometrical optics and diffraction theory. Depending on the shape and geometry of the scatterer, UTD may provide many different mechanisms, including first-order UTD diffraction, (higher-order) slope diffraction, and equivalent currents, to increase the accuracy of the diffracted-field calculations. Far-zone amplitude patterns in both the E and H planes are calculated for circular waveguide antennas, and the calculated results are compared with measurements and HFSS simulations over a dynamic range of 80 dB.

4.1.1. *Dielectric-Covered Aperture Antennas*

It is generally necessary to cover aperture antennas for different purposes. For example, aperture antennas in aircrafts and spacecrafts are covered by a dielectric material to protect them from environmental conditions. For the space shuttles, antennas are covered by a dielectric material as a protective heat shield. Also, the electromagnetic properties of the coating may be used to obtain certain radiation performance and to increase the design parameters of the antenna. However, since the coatings have a relative permittivity greater than unity, or have a complex relative permittivity, such a coating can be expected to impact the radiation characteristics and performance of the antenna. Therefore, the effects of a dielectric cover has investigated and received much attention in the last several decades [33], [34]. Many researchers investigated the coating impact on slot antennas on conducting circular [35-42] and elliptic [43-48] cylinders loaded and/or coated by dielectric and plasma. The spectral domain method was applied to aperture antennas mounted on infinite ground planes [11], and on infinite dielectric-covered ground planes [49]. This method, previously developed to determine the radiated fields from an aperture in a coated cylinder [50], is extended to obtain the solution for the radiated fields by an aperture in a coated ground plane. In particular, the radiation structure considered is an infinite perfectly conducting plane with a circular aperture excited by a specified tangential electric field distribution. The entire plane is generally covered by a dielectric layer of complex permittivity, complex permeability, and thickness t as depicted in Fig. 4.1.

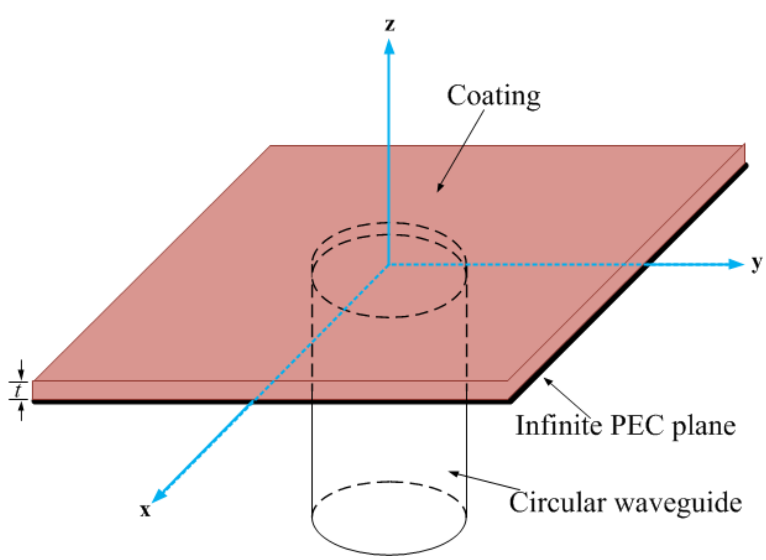

Fig. 4.1. Circular Aperture Antenna Mounted on a Coated Perfectly Conducting Plane.

The fields, radiated by a coated aperture on a perfectly conducting plane due to the field distribution over the circular aperture, are obtained by solving a two-region boundary-value problem [49]. The first region is $0 \le z \le t$ and the second region is $t \le z \le \infty$, as shown in Fig. 4.2. The spectral domain method is used to solve for the far-zone radiated fields. The axial z components of both the E and H fields satisfy the scalar wave equation in each region, namely $\nabla^2 u + \beta_c^2 u = 0$ where u can represent any of the axial components of either the electric or magnetic fields in either region and β_c is the cutoff phase factor. The coating and the free-space regions above it are denoted as "Region I" and "Region II," respectively, in Fig. 4.2. In region I the propagation is taken as $e^{\pm\gamma_1 z}$; γ_1 is the propagation factor in the coating. In region II, the phase is represented by $e^{-j\beta_2 z}$; β_2 is the phase factor in the region external to the coating. Double Fourier transforms are used to express the axial field solution over mode space. Then, Maxwell's equations and the assumed propagation are used to find the transverse fields. In general, by applying the tangential boundary conditions at the surfaces $z = 0$ and $z = t$, the fields radiated by a coated aperture are given by [49]

$$E_\theta(r,\theta,\phi) = f(\theta)(\overline{E}_x \cos\phi + \overline{E}_y \sin\phi) \tag{4.1}$$

$$E_\phi(r,\theta,\phi) = g(\theta)(-\overline{E}_x \sin\phi + \overline{E}_y \cos\phi)\cos\theta \tag{4.2}$$

where $\overline{E}_x$ and $\overline{E}_y$ are the double Fourier transforms of the x and y components, respectively, of the electric field over the aperture, and

$$f(\theta) = \frac{e^{jkt\cos\theta}}{\cos\psi + jZ_h \sin\psi} \tag{4.3}$$

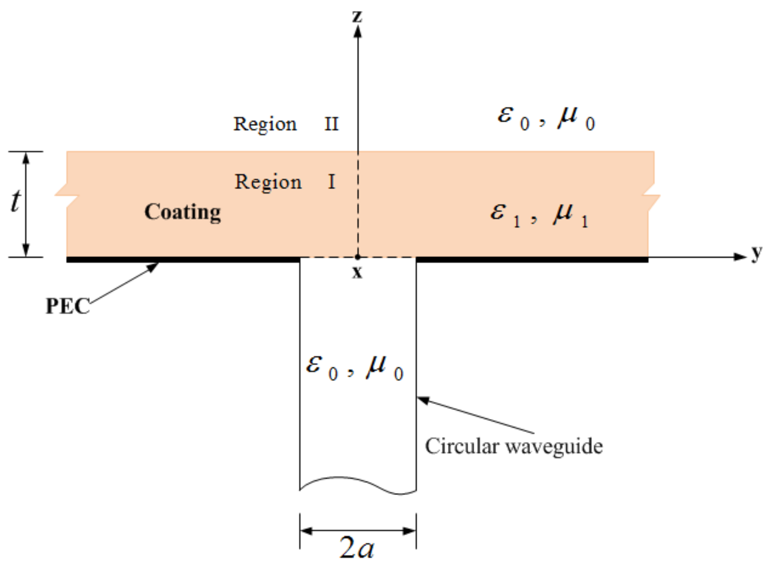

Fig. 4.2. Two-Dimensional Geometry of a Circular Aperture Antenna Mounted on a Coated Perfectly Conducting Plane.

$$g(\theta) = \frac{e^{jkt\cos\theta}}{\cos\psi + jZ_e \sin\psi} \tag{4.4}$$

with

$$\psi = kt\sqrt{\mu_r\varepsilon_r - sin^2\theta} \tag{4.5}$$

$$Z_h = \frac{\sqrt{\mu_r\varepsilon_r - \sin^2\theta}}{\varepsilon_r\cos\theta} \tag{4.6}$$

$$Z_e = \frac{\mu_r\cos\theta}{\sqrt{\mu_r\varepsilon_r - \sin^2\theta}} \tag{4.7}$$

where k is the free space wave number, ε_r is the complex relative permittivity, and μ_r is the complex relative permeability.

For the same aperture excitation, the far-zone fields radiated by a coated aperture, mounted on an infinite ground plane, are related to those of an uncoated by simple multiplicative functions which depend only on the parameters of the dielectric coating, the coating thickness, and the off-axis angle (θ).

$$E_\theta(r,\theta,\phi) = f(\theta)\cdot E^0_\theta(r,\theta,\phi) \tag{4.8}$$

$$E_\phi(r,\theta,\phi) = g(\theta)\cdot E^0_\phi(r,\theta,\phi) \tag{4.9}$$

where E_θ, E_ϕ are the electric field components of the covered aperture and E^0_θ, E^0_ϕ are the electric field components of an uncovered aperture, respectively, given by (3.48) and (3.49).

When the permittivity of the dielectric layer equals the permittivity of free space, or when the thickness of the dielectric coating t is zero, (4.8) and (4.9) reduce to those for the uncoated case.

The antenna under consideration consists of a circular waveguide, opening onto a finite, perfectly electric conducting flat ground plane coated with a dielectric material of thickness t and complex permittivity and permeability as shown in Fig. 4.2. The circular waveguide dominant TE_{11} mode is assumed over the circular aperture, and the higher-order reflected modes are taken to be negligible. It is also assumed that no higher-order waveguide modes are excited at the aperture. The medium inside the waveguide and external to the structure is assumed to be free space. The fields within the circular waveguide are uniquely defined by a discrete TE vector potential with one unknown, the reflection coefficient. Standing waves represent the fields inside the dielectric coating, and these waves are described by integral transforms of TE and TM potentials, each containing two unknown coefficients. In addition, each potential exterior to the dielectric coating has one unknown coefficient. To solve for the these unknowns, the boundary conditions at the aperture and at the outer surface of the dielectric coating are used.

4.1.2. *Impedance Surface Boundary Conditions (ISBCs)*

The increasing application of lossy/lossless dielectric materials increases the need for suitable methods to characterize the response of these materials, including the scattering effects of edge/wedges and discontinuities. The approximate impedance boundary conditions are widely used in scattering, edge/wedge diffraction, and propagation problems to simulate impact of the material properties and the surface geometry. The approximate impedance boundary conditions are an effective approach to model the surface impedance. The impedance surfaces play an important role in the modelling of metallic and nonmetallic objects. This approach is good for conductors and lossy materials where there is some penetration of the field. The electromagnetic scattering from a wedge with impedance faces is one of the most important canonical problems in the geometrical theory of diffraction analysis. The boundary conditions can be used when the fields outside the material body are required. If the fields inside the body are required, the boundary conditions are unapplicable.

The impedance surface boundary conditions, introduced by *Leontovich* in 1940's [51], are widely used to simulate the material properties of a scatterer, and they can be very helpful in simplifying the analytical and numerical solutions of scattering problems. The surface impedance concept was used in 1938 in an attempt to simplify the analysis of propagation of electromagnetic (radio) waves over the surface of the earth [52]. Using the exact boundary conditions of the earth's surface results in complicated analytical and numerical analyses. Consequently, approximate boundary conditions are applied to simplify the problem. Since then, the use of impedance surface boundary conditions has resulted in new methods of computation.

The geometry of the actual scattering object can be locally approximated by canonical shapes, whereas its electromagnetic properties can be accounted for by adopting suitable approximate impedance surface boundary conditions [52]. ISBC's constitute a very useful approximation for approaching scattering problems, since they allow evaluating the material effects while avoiding the calculation of the fields within the material itself.

To better understand the concept of impedance surface boundary conditions, the perfect conductors are reviewed first. In a perfect electric conductor, the tangential components of the electric and normal components of the magnetic field vectors are zero. So there are no surface currents over the PEC surface, and the surface impedance is zero. Because the field penetration is zero, the perfect conductor is entirely excluded from computation [52]. However, its impact must be taken into account by imposing boundary conditions (surface impedance) at the PEC ground plane. Reflections from the ground plane are properly taken into account by the boundary conditions to accurately calculate the field in the space near the conductor. However, for a non-perfect electric conductor, some of the electromagnetic field will penetrate inside the conductor due to the skin effect. Therefore, the longitudinal electric field component will vanish. This condition produces a non-zero surface impedance associated with the skin-effect phenomenon. Because of the continuity properties of the electromagnetic field across the conductor's surface, the ratio of the tangential electric and tangential magnetic fields at the interface is assumed to be equal to the wave impedance in the conductor.

Based on the impedance surface boundary condition, the tangential electric and magnetic field vectors can be related by a constant impedance which is related only to the properties and configurations of the coating and is independent of the source illumination. At the surface interface, the tangential electric and magnetic field vectors are mutually perpendicular and related by the impedance of the surface [52]. Similar to the circuit theory where the ratio between voltage and current is denoted by the term *impedance*, the approximate boundary conditions have received the name surface impedance boundary conditions. In a vector equation, the impedance surface boundary condition can by written as

$$\overline{E} - (\hat{n} \cdot \overline{E})\hat{n} = Z\hat{n} \times \overline{H} = \eta Z_0(\hat{n} \times \overline{H}) \tag{4.10}$$

where $\overline{E}$ is the electric field vector, $\overline{H}$ is the magnetic field vector, and $\hat{n}$ is the outward unit normal to the surface. Z is the surface impedance, and η is the normalized impedance relative to the intrinsic impedance Z_0 of free space.

Since these approximate boundary conditions relate the electric and magnetic fields outside the scatterer, the scattered fields can be evaluated without involving the internal fields. Thus, the problem of analysis is considerably simplified by involving only the external fields imposed at the outer surface to simulate the material properties of the body. Then a two-media problem is converted into a one-media problem.

The normalized equivalent surface impedance may be obtained from a simple transmission line model [53-54], where the short-circuited transmission-line approximation is used to account for the coating impedance. By considering the coating as a section of a transmission line of length t and characteristic impedance η, terminated with the impedance η_L, the input impedance, corresponding to the normalized equivalent surface impedance of an obliquely incident plane wave, is

$$\eta_{eq} = \eta \frac{\eta_L + j\eta \tan(k_1 t \sin\varphi_t)}{\eta + j\eta_L \tan(k_1 t \sin\varphi_t)} \tag{4.11}$$

for a coated perfect electric conductor ($\eta_L = 0$), (4.11) reduces to

$$\eta_{eq} = j\eta \tan(k_1 t \sin\varphi_t) \tag{4.12}$$

where η is the characteristic impedance of the coating material $\sqrt{\mu_1\varepsilon_0/\mu_0\varepsilon_1}$, and k_1 is the phase constant $\omega\sqrt{\mu_1\varepsilon_1}$. For lossy materials, the permittivity ε_1 and permeability μ_1 may be complex.

The angle of reflection φ_t can be determined, given the angle of incidence φ_i and the constitutive parameters, by [54]

$$\sin\varphi_t = \sqrt{1 - \frac{\mu_0\varepsilon_0}{\mu_1\varepsilon_1}\cos^2\varphi_i} \tag{4.13}$$

4.2. Geometrical Theory of Diffraction for an Edge on an Impedance Surface

The subject of non-specular electromagnetic scattering by impedance structures has been an area of great interest in recent years where the scattering of electromagnetic waves by impedance wedges has many practical applications. The scattering properties of a structure are a function of both its geometrical and materials properties. The solution of scattering problems in Chapter 3 is applicable only to the PEC wedge. However, in many applications, the wedges are not perfect metallic. Therefore, investigation of the reflection, transmission, and diffraction properties of impedance wedges is important. Among the various structures studied, the impedance wedge has received considerable attention. Unlike reflection, diffraction contributes to wave propagation within the shadow zone. To study the scattering properties of impedance wedges, *Leontovich* developed a boundary condition known as the impedance or *Leontovich* boundary condition, which greatly simplifies the analysis. Although the impedance boundary conditions provide an approximate relationship between the electric and magnetic field on the surface of the scatterer, it is a very useful approximation because they provide and simplify the analytical and numerical solution of many practical problems which otherwise could not be solved.

The GTD/UTD [18], [22] has been widely and successfully employed in terms of solving a wide variety of perfectly conducting electromagnetic problems involving diffraction at edges in perfectly conducting surfaces. Its extension to the case of non-perfectly conducting surfaces may provide a significant improvement to the applicability of ray methods. With the impedance wedge's diffraction coefficients it is possible to solve the scattering problem of a wide variety of new problems for which the impedance surface boundary conditions can be applied. The uniform GTD formulation was rigorously derived by asymptotically evaluating the exact solution given by Maliuzhinets [55], who used the method of Sommerfeld. A uniform high-frequency solution to the diffraction by a wedge with arbitrary uniform isotropic impedance faces is provided by this method. The wedge face is illuminated by a plane wave normally incident on the edge of the wedge. The impedance wedge UTD formula is achieved by introducing suitable multiplying factors. Although these factors involve a special function which is difficult to calculate for a general exterior ($n\pi$) wedge angle, more numerically tractable expressions are available when n is a rational number. In particular, this function can be very easily calculated for the four important cases $n = 1/2, 1, 2, 3/2$.

The Maliuzhinets method basically consists of expressing the total field as a spectrum of plane waves over a Sommerfeld contour, represented as an integral with an unknown spectral function. The unknown spectral function is then determined using the boundary conditions. Next, the integral equation is transformed into a first-order functional difference equation whose solution gives the unknown spectral function. When the spectral function is obtained, the diffracted field can be asymptotically evaluated. This solution yields the GO fields as well as the diffracted fields and surface waves, if they exist. However, the diffraction coefficient obtained from this solution is only applicable to two-dimensional structures and for practical applications it is necessary to derive coefficients applicable to three dimensions. This requires the solution of the impedance wedge problem with a plane wave excitation at skew angles. So far, the exact solution to this problem has only been obtained for a few wedge angles. In particular, solutions are possible only for wedges with angles of 0 (half plane) [56], $\frac{\pi}{2}$ (with one face perfectly conducting) [57], π and $\frac{3\pi}{2}$ (with one face perfectly conducting) [48], [59].

The main difficulty in obtaining the skew incidence solution for the diffraction by an impedance wedge is the lack of techniques to solve the resulting four coupled functional difference equations. For the specific wedges mentioned above, the resulting four difference equations can be decoupled yielding the solution given by the references. However, the coupling of the four difference equations for other wedge angles is not yet solved. An approximate solution for an impedance wedge, illuminated at skew incidence, has been developed using Maliuzhinets method [56]. In this solution, the exact diffraction coefficients are recovered for the impedance half plane, illuminated at skew incidence, and for the impedance wedge illuminated at normal incidence.

4.2.1. *Diffracted Fields*

The calculation of the diffracted fields for material wedges is considerably more complex than for PEC surfaces. For non perfect surfaces, the boundary conditions couple the magnetic and electric fields. The two dimensional (2-D) geometry of the wedge scattering problem is depicted in Fig. 4.3. The impedance wedge has its edge along the z-axis of a cylindrical coordinate system (ρ, ϕ, z). The top face is 0 face and the bottom face is n face. The exterior wedge angle is denoted by $n\pi$, and the angles of incident and of diffraction, measured with respect to the 0 face, are denoted by ϕ_0 and ϕ, respectively. The ISB and RSB refer to the Incident Shadow Boundary and Reflected Shadow Boundary, respectively. The surface impedance at $\phi = 0$ and $\phi = n\pi$ faces are denoted by Z_0 and Z_n, respectively. The surface impedances are usually complex numbers whose real parts must be nonnegative because of energy considerations. A time harmonic dependence $\exp(i\omega t)$ is assumed and suppressed in the following.

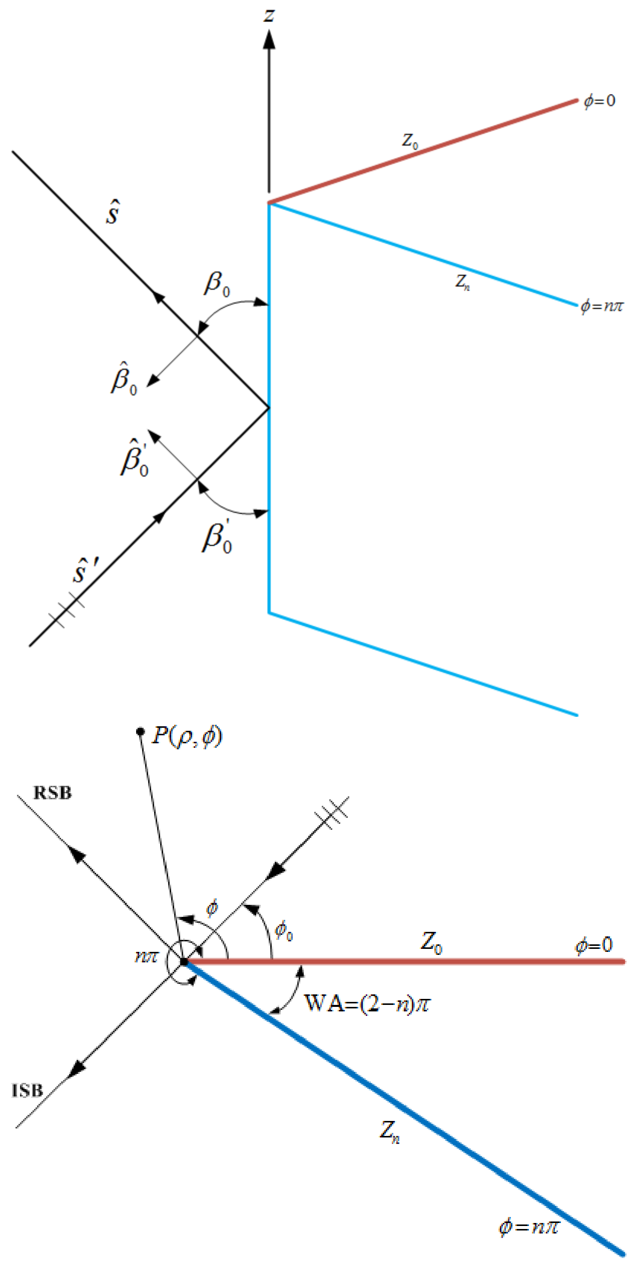

Fig. 4.3. Geometry for the Diffraction by a Wedge with Impendence Faces.

The longitudinal components of the normal incident field can be expressed as

$$E_z^i \quad \text{or} \quad H_z^i = e^{jk\cos(\phi-\phi_0)} \tag{4.14}$$

where k is the wave number of free space.

According to Maxwell equations, two groups of boundary conditions for corresponding faces of the third kind are obtained; for TE wave

$$\frac{1}{\rho}\frac{\partial H_z}{\partial \phi} \mp jk\sin\theta^h_{0,n}H_z = 0 \qquad\qquad \phi = 0, n\pi \tag{4.15}$$

and for TM wave

$$\frac{1}{\rho}\frac{\partial E_z}{\partial \phi} \mp jk\sin\theta^e_{0,n}E_z = 0 \qquad\qquad \phi = 0, n\pi \tag{4.16}$$

$$\sin\theta^h_{0,n} = \frac{Z_{0,n}}{Z} \qquad\qquad \sin\theta^e_{0,n} = \frac{Z}{Z_{0,n}} \tag{4.17}$$

where Z is the free space impedance, "$-$" and 0 in 4.15 and 4.16 correspond to $\phi = 0$ while "$+$" and n correspond to $\phi = n\pi$. The surface impedance for each of the wedge faces is used to determine the Brewster angle, $\theta_{0,n}$, for that surface, where the Brewster angle is the angle at which no reflection is present. The Brewster angle is polarization dependent; for soft polarization

$$\theta_0 = \sin^{-1}\left(1/\eta_0\right) \qquad\qquad \theta_n = \sin^{-1}\left(1/\eta_n\right) \tag{4.18}$$

and for hard polarization

$$\theta_0 = \sin^{-1}(\eta_0) \qquad\qquad \theta_n = \sin^{-1}(\eta_n) \tag{4.19}$$

where $\eta_0 = \frac{Z_0}{Z}$ and $\eta_n = \frac{Z_n}{Z}$

In this study, the Brewster angle of the coated face is complex because the coating has a complex surface impedance.

Throughout this work, superscripts e and h have been suppressed. The TM and TE cases are treated together, and the expressions presented later on apply to both cases provided that the proper value for $\theta_{e,h}$ is used based on 4.18 and 4.19.

According to the Sommerfeld-Maliuzhinets method, the exact solution for the total fields, in the region surrounding the wedge at observation point $P(\rho,\phi)$, can be expressed in plane wave spectral integral form as [11], [55]

$$U_t(\rho,\phi) = \frac{1}{2n\pi j}\int_\gamma \frac{\psi(\alpha+\frac{n\pi}{2}-\phi)}{\psi(\frac{n\pi}{2}-\phi_0)} \cdot \frac{\sin\frac{\phi_0}{n}}{\cos\frac{\alpha-\phi}{n}-\cos\frac{\phi_0}{n}} \quad e^{jk\rho\cos\alpha} d\alpha \tag{4.20}$$

the $\gamma = \gamma_1 + \gamma_2$ is the Sommerfeld integral path shown in Fig. 4.4, $\psi(\alpha) = \psi(\alpha,\theta_0,\theta_n,n)$ is the auxiliary Maliuzhinest function. This function depends explicitly on the integration variable α and implicitly on the parameters $\theta_0,\theta_n,$and n, and it is defined as [55]:

$$\psi(\alpha) = \psi_n\left(\alpha+\frac{n\pi}{2}+\frac{\pi}{2}-\theta_0\right)\cdot\psi_n\left(\alpha-\frac{n\pi}{2}-\frac{\pi}{2}+\theta_n\right)\cdot \\ \psi_n\left(\alpha+\frac{n\pi}{2}-\frac{\pi}{2}+\theta_0\right)\cdot\psi_n\left(\alpha-\frac{n\pi}{2}+\frac{\pi}{2}-\theta_n\right) \tag{4.21}$$

$\psi_n(\alpha)$ is the Maliuzhinets function given by [55]:

$$\psi_n(\alpha) = exp\left[-\frac{1}{2}\int_0^\infty \frac{\cosh(\alpha s)-1}{s\cosh(\frac{\pi}{2}s)\sinh(n\pi s)}\ ds\right] \tag{4.22}$$

The exact solution for the total field in (4.20) is not practically convenient as it stands, and the integral of (4.20) is difficult to evaluate efficiently. To construct a more useful form of the integral, the exact solution is transformed to an integral along the Steepest Descent Paths ($SDPs$) through the saddle points at $(\pm\pi)$, which account for the diffracted fields by the edge, and the residue contributions of the real and complex poles, which account,

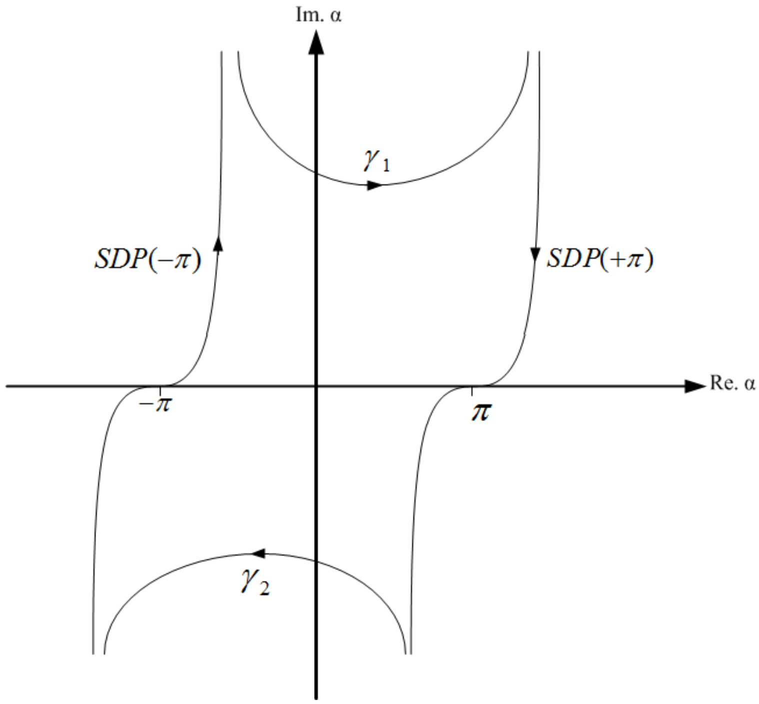

Fig. 4.4. Sommerfeld Contour in the Complex α Plane [11], [56].

respectively, for the geometrical optics fields and the surface wave fields. After deformation of it to the steepest descent path, the total field can be written [11]

$$U_t(\rho,\phi) = 2\pi j \sum \text{Res.} - \frac{j}{2n\pi} \int_{SDPs} \frac{\psi(\alpha + \frac{n\pi}{2} - \phi)}{\psi(\frac{n\pi}{2} - \phi_0)} \cdot \frac{\sin\frac{\phi_0}{n}}{\cos\frac{\alpha-\phi}{n} - \cos\frac{\phi_0}{n}} \; e^{jk\rho\cos\alpha} d\alpha \tag{4.23}$$

$$U_t(\rho,\phi) = U_i + \sum U_r^{\pm} + \sum U_s^{\pm} - \frac{j}{2n\pi} \int_{SDPs} \frac{\psi(\alpha + \frac{n\pi}{2} - \phi)}{\psi(\frac{n\pi}{2} - \phi_0)} \frac{\sin\frac{\phi_0}{n}}{\cos\frac{\alpha-\phi}{n} - \cos\frac{\phi_0}{n}} \; e^{jk\rho\cos\alpha} d\alpha \tag{4.24}$$

where $SDPs$ is the path $SPD(+\pi) + SDP(-\pi)$

The last term in (4.24) is the diffracted field U_d while the remaining terms are pole residue terms giving the geometrical optics incident field U_i, the geometrical optics reflected field from the wedge faces U_r^+, U_r^-, and surface waves U_s^+, U_s^-, traveling away from the edge along each wedge face. The residues are those of the poles $\alpha = \alpha_p$ such that

$$-\pi < \mathrm{Re}(\alpha) - \cos^{-1}\left(\frac{1}{\cosh(\mathrm{Im}(\alpha))}\right) sign(\mathrm{Im}(\alpha)) < \pi \tag{4.25}$$

The poles responsible for surface waves are, in general, complex, but those producing the incident and reflected fields are real. Of the latter, the only ones satisfying (4.24) are

$$\alpha_i = \phi_0 - \phi \quad \alpha_r^+ = -\phi_0 - \phi + n\pi \quad \alpha_r^- = \phi_0 - \phi - n\pi \tag{4.26}$$

The incident field U_i is determined from α_i in the illuminated region, whereas α_r^+ and α_r^- give rise to the fields reflected from the 0 and $n\pi$ faces of the wedge, respectively.

The surface waves in (4.24) are evaluated by identifying the surface wave poles. These poles accrue at

$$\alpha_s^0 = \phi + \pi + \theta_0 \qquad \alpha_s^n = \phi_0 - \pi - n\pi - \theta_n \tag{4.27}$$

The surface wave contribution depends on the complex Brewster angles $\theta_{0,n}$ of the surfaces of the wedge. These angles are complex if $\eta_{0,n}$ are complex or real with $|\eta_{0,n}| > 1$.

When $k\rho$ is large enough, the uniform diffracted solution can be obtained by the modified Pauli-Chemmow steepest descent method, which considers the effects of the four poles nearest the steepest descent paths. These poles yield four Fresnel transition functions providing continuity across the shadow boundaries [11].

$$
\begin{aligned}
&U_d(\rho,\phi) = \frac{e^{-jk\rho}}{\sqrt{\rho}}\left[-\frac{e^{-j\pi/4}}{2n\sqrt{2\pi k}}\right] \\
&\cdot\left[\frac{\psi(-\pi+\frac{n\pi}{2}-\phi)}{\psi(\frac{n\pi}{2}-\phi_0)}\cdot\frac{\sin\frac{\phi_0}{n}+\sin\frac{\theta_0}{n}}{\sin\frac{\phi+\pi}{n}+\sin\frac{\theta_0}{n}}\cot\left(\frac{\pi+\beta^-}{2n}\right)F[k\rho(1+\cos(\beta^- - 2n\pi N_-^+))]\right. \\
&+\frac{\psi(+\pi+\frac{n\pi}{2}-\phi)}{\psi(\frac{n\pi}{2}-\phi_0)}\cdot\frac{\sin\frac{\phi_0}{n}+\sin\frac{\theta_0}{n}}{\sin\frac{\phi-\pi}{n}+\sin\frac{\theta_0}{n}}\cot\left(\frac{\pi-\beta^-}{2n}\right)F[k\rho(1+\cos(\beta^- - 2n\pi N_-^-))] \\
&+\frac{\psi(-\pi+\frac{n\pi}{2}-\phi)}{\psi(\frac{n\pi}{2}-\phi_0)}\cdot\frac{\sin\frac{\phi_0}{n}+\sin\frac{\theta_0}{n}}{\sin\frac{\phi+\pi}{n}+\sin\frac{\theta_0}{n}}\cot\left(\frac{\pi+\beta^+}{2n}\right)F[k\rho(1+\cos(\beta^+ - 2n\pi N_+^+))] \\
&\quad\left.+\frac{\psi(+\pi+\frac{n\pi}{2}-\phi)}{\psi(\frac{n\pi}{2}-\phi_0)}\cdot\frac{\sin\frac{\phi_0}{n}+\sin\frac{\theta_0}{n}}{\sin\frac{\phi-\pi}{n}+\sin\frac{\theta_0}{n}}\cot\left(\frac{\pi-\beta^+}{2n}\right)F[k\rho(1+\cos(\beta^+ - 2n\pi N_+^-))]\right]
\end{aligned}
\tag{4.28}
$$

where $F(x)$ is the Fresnel integral, and the N's are the positive or negative integer or zero which most nearly satisfies:

$$2\pi n N_-^+ - \beta^- = \pi \tag{4.29}$$

$$2\pi n N_-^- - \beta^- = -\pi \tag{4.30}$$

$$2\pi n N_+^+ - \beta^+ = \pi \tag{4.31}$$

$$2\pi n N_+^- - \beta^+ = -\pi \tag{4.32}$$

The diffraction coefficients in (4.28) have the same structure as those of the UTD in its original formulation for a perfectly conducting wedge. The preceding UTD solution predicts vanishing diffraction coefficients for grazing incidence because it retains only the first term of an asymptotic expansion. Therefore, the diffracted fields do not contribute to the total field, leading to large discontinuities in the plate plane. To correctly compensate for these discontinuities in the pattern, the high-order nonvanishing terms of an asymptotic expansion need to be retained. To derive a high-frequency expression for the diffracted field, which is uniformly valid at any incident aspect and for any impedance boundary condition, more accurate asymptotic evaluation as in [60] is employed. For the half plane, it is given by

$$\begin{aligned} U_d(\rho,\phi) = {} & \frac{e^{-jk\rho}}{\sqrt{\rho}} \frac{e^{-j\pi/4}}{\sqrt{2\pi k}} \\ & \cdot \frac{\psi_2(\frac{5\pi}{2}-\phi+\theta_0)\psi_2(-\frac{\pi}{2}-\theta_0)\psi_2(\frac{\pi}{2}+\phi+\theta_2)\psi_2(\frac{3\pi}{2}-\theta_2)}{\psi_2(\frac{5\pi}{2}-\phi-\theta_0)\psi_2(-\frac{\pi}{2}+\theta_0)\psi_2(\frac{\pi}{2}+\phi-\theta_2)\psi_2(\frac{3\pi}{2}+\theta_2)} \\ & \cdot \frac{\sin\frac{\theta_0-3\pi}{4}\sin\frac{\theta_2-\pi}{4}}{\sin\frac{\theta_0-\phi}{4}\sin\frac{\theta_2+\phi-2\pi}{4}} \cdot \frac{\sin\phi}{1+\cos\theta_2} \\ & \quad \cdot (1+\sin(\theta_2)[f_2(\frac{3\pi}{2}-\theta_0)+f_2(\frac{\pi}{2}+\theta_0)+f_2(-\frac{\pi}{2}-\theta_2)+f_2(-\frac{3\pi}{2}+\theta_2)+\frac{1}{2\cos\frac{\phi}{2}}]) \\ & \cdot \frac{F[2kL\cos^2(\frac{\phi}{2})]-F[2kL\sin^2(\frac{\theta_2}{2})]}{\cos^2(\frac{\phi}{2})-\sin^2(\frac{\theta_2}{2})} \end{aligned} \tag{4.33}$$

where all parameters are defined in [60].

4.2.2. *Surface Waves*

The surface waves propagate along the surface of the wedge, and they are exponentially decaying away from the face of the wedge. Although they decay rapidly along the wedge face, their contributions can be more dominant than other scattering mechanisms near the wedge surface.

The surface waves are determined by the residues of complex poles of the auxiliary Maliuzhinets function enclosed between the steepest descent paths. The location of the surface wave poles depend on the properties of the wedge material and hence the surface wave only exists for certain impedances. They exist only over a specified angular region given by [11]:

$$-\pi < \left[\alpha_r - \cos^{-1}\left(\frac{1}{\cosh(\alpha_i)}\right) sign(\alpha_i)\right] < \pi \tag{4.34}$$

where $\alpha = \alpha_r + j\alpha_i$; the surface wave poles are located at

$$\alpha_0 = \phi + \pi + \theta_0 \tag{4.35}$$

$$\alpha_n = \phi - n\pi - \pi - \theta_n \tag{4.36}$$

for the 0 and n faces, respectively. The capacitive surfaces support the surface wave only for the soft polarization. For inductive surfaces, the surface wave exists only for the hard polarization.

In this work, the n face is perfectly conducing. Therefore, this face can not support surface waves. As a surface wave pole moves outside the steepest descent paths, its contribution vanishes. After calculating the complex pole residue, the expressions for the surface waves that exist on both faces of a general impedance wedge are [11]:

$$\begin{aligned} U_{sw}^0 = {} & \frac{2\sin\frac{\pi}{2n}}{\psi(\frac{n\pi}{2} - \phi_0)} \frac{\sin\frac{\phi_0}{n}}{\cos(\frac{\pi+\theta_0}{n}) - \cos(\frac{\phi_0}{n})} e^{-jk\rho\cos(\phi+\theta_0)} \\ & \cdot \psi_n\left(n\pi - \frac{\pi}{2}\right) \psi_n\left(\frac{\pi}{2} + n\pi + 2\theta_0\right) \psi_n\left(\frac{3\pi}{2} + \theta_0 - \theta_n\right) \psi_n\left(\frac{\pi}{2} + \theta_0 + \theta_n\right) \end{aligned} \tag{4.37}$$

$$\begin{aligned} U_{sw}^n = {} & \frac{-2\sin\frac{\pi}{2n}}{\psi(\frac{n\pi}{2} - \phi_0)} \frac{\sin\frac{\phi_0}{n}}{\cos(\frac{\pi+\theta_0}{n}) - \cos(\frac{\phi_0}{n})} e^{-jk\rho\cos(\phi-n\pi-\theta_n)} \\ & \cdot \psi_n\left(n\pi - \frac{\pi}{2}\right) \psi_n\left(\frac{\pi}{2} + n\pi + 2\theta_n\right) \psi_n\left(\frac{3\pi}{2} + \theta_n - \theta_0\right) \psi_n\left(\frac{\pi}{2} + \theta_0 + \theta_n\right) \end{aligned} \tag{4.38}$$

Discontinuities at the surface wave boundaries occur because the surface waves exist only over a limited angular region close to the wedge faces. To provide proper continuity in the total field across the surface wave boundaries, the surface wave transition field needs to be considered. As the uniform theory of diffraction compensates the geometrical optics discontinuities at the shadow boundaries, the surface wave transition field corrects for the surface wave discontinuities. The method of Felsen-Marcuvitz is used to determine the complex surface wave pole contribution in the steepest decent integral, which is given by [11]

$$U^0_{swtr} = \frac{e^{-jk\rho}}{\rho}\left[\frac{-\sqrt{\frac{j}{\pi}}\sin(\frac{\pi}{2n})}{\psi(\frac{n\pi}{2}-\phi_0)}\right]\frac{\sin(\frac{\phi_0}{n})}{\cos(\frac{\pi+\theta_0}{n})-\cos(\frac{\phi_0}{n})}\frac{\left[F[k\rho(1-\cos(\phi+\theta_0))]-1\right]}{\sqrt{k(\cos(\phi+\theta_0)-1)}}$$
$$\psi_n\left(n\pi-\frac{\pi}{2}\right)\psi_n\left(\frac{\pi}{2}+n\pi+2\theta_0\right)\psi_n\left(\frac{3\pi}{2}+\theta_0-\theta_n\right)\psi_n\left(\frac{\pi}{2}+\theta_0+\theta_n\right) \quad (4.39)$$

$$U^n_{swtr} = \frac{e^{-jk\rho}}{\rho}\left[\frac{-\sqrt{\frac{j}{\pi}}\sin(\frac{\pi}{2n})}{\psi(\frac{n\pi}{2}-\phi_0)}\right]\frac{\sin(\frac{\phi_0}{n})}{\cos(\frac{n\pi+\pi+\theta_n}{n})-\cos(\frac{\phi_0}{n})}\frac{\left[F[k\rho(1-\cos(\phi-n\pi-\theta_n))]-1\right]}{\sqrt{k(\cos(\phi-n\pi-\theta_n)-1)}}$$
$$\psi_n\left(n\pi-\frac{\pi}{2}\right)\psi_n\left(\frac{\pi}{2}+n\pi+2\theta_0\right)\psi_n\left(\frac{3\pi}{2}+\theta_n-\theta_0\right)\psi_n\left(\frac{\pi}{2}+\theta_0+\theta_n\right) \quad (4.40)$$

where $F(x)$ is the Fresnel integral with complex argument.

When the observation angles are outside the surface wave boundaries, the surface wave and surface wave transition terms vanish and only the geometrical optics and diffracted fields are considered to calculate the total field. The surface wave transition terms must be included if the surface wave pole is close to the steepest descent paths even if the surface wave does not contribute.

For circular edges, the GTD does not provide a valid diffracted field at the axial caustics. The reason is that the first-order stationary phase evaluation of the integral expression, representing the diffracted field, yields the GTD result at point observations away from caustics. Therefore, a caustic correction is needed for angles at and near the axis of the antenna. Using the method of equivalent currents and wedge diffraction coefficients, the caustic problem can be corrected [5]. In this method, equivalent magnetic and electric currents are created along the edge of the ground plane. Then, radiation integrals are used to obtain the fields due to these currents which correct the diffracted fields at and near the symmetry axis of the antenna.

For the square ground plane, the edge diffractions do not significantly contribute to the H-plane radiation pattern in the backlobe region. However, the edge diffractions in the E-plane are much more intense and contribute more significantly to the overall pattern, above and below the ground plane. Therefore, one needs to include the contributions from the E-plane edge diffractions using the method of equivalent currents [5]. By using the equivalent currents concept, it is possible to evaluate the diffracted field outside the Keller cone directions.

4.3. Validation

To experimentally determine effects of ground plane edge diffractions on radiation patterns of coated circular aperture antennas, a circular aperture antenna was measured in the ElectroMagnetic Anechoic Chamber (EMAC) facility at Arizona State University. Validity of the analysis is established by satisfactory agreement between the predicted and measured data and those simulated by Ansofts High Frequency Structure Simulator (HFSS). Good agreement is observed for all cases considered.

4.3.1. *Circular Waveguide Mounted on Square and Circular Coated Ground Planes*

A model for the circular and square dielectric-covered ground planes with the circular waveguide mounted at the center has been constructed. The aperture antenna is assumed to be excited by the TE_{11}-mode circular waveguide. The width of the coated square ground plane and the diameter of the coated circular ground plane are 12 in.. The relative permittivity (ε_r) and the loss tangent $(\tan\delta)$ of the coating material are, respectively, 2.9 and 0.02 at 10 GHz. The thickness of the dielectric layer, made from polycarbonate (Lexan), is 0.099 in. and the normalized surface impedance is $0.7480 + j0.4894$ calculated using (4.12). The validity of the radiation pattern formulation over the main beam and the near and far sidelobes has been verified by calculating the far-zone E- and H-plane amplitude patterns of the aperture. The frequency at which the measurements were performed is 10 GHz. The diameter of the aperture is 0.938 in.. Measurements and numerical data based on diffraction techniques were also compared with the HFSS simulations.

Figs. 4.5 and 4.6 exhibit, respectively, the far-zone E- and H-plane amplitude patterns of a circular aperture mounted on circular dielectric-covered ground planes. For the square dielectric-covered ground planes, the amplitude patterns of the E and H planes are, respectively, shown in Figs. 4.7 and 4.8. Because the amplitude patterns of interest are in the principle planes, the most significant diffractions come from two diffraction points which are diametrically opposite to each other and along the principle planes [5]. Good agreement between GO/GTD/UTD calculations, experiments, and HFSS simulations is indicated. As shown in the figures, the amplitude patterns in the E-plane are broader than that in the H-plane. The ripples in the amplitude patterns, especially in the backlobe region, are attributed to the impedance edge diffractions. The ripples shown in the patterns are due of the constructive and destructive interference of the diffractions from the diametrically opposite diffraction points. In the E-plane, these ripples are more significant because the incident electric field at the point of diffraction is more intense in this plane than in the H-plane.

Although the side of the square is equal to the diameter of the circular, it is very clear from the patterns of Figs. 4.5 - 4.8 that the E- and H-plane amplitude patterns of the circular coated ground plane are greater than those of the square coated ground plane at and near the antenna axis ($\theta = 180^0$). These are due to the ring radiator which contributes about an additional 8-10 dB.

The radiation amplitude in the back region of the aperture antenna mounted on coated ground planes depends significantly on the size and geometry of the ground plane. Fig. 4.9 indicates, as expected, that the amplitude pattern level at $\theta = 180^\circ$ decreases monotonically with increasing the ground plane size for both geometries, circular and square. Because of the ring radiator of the circular ground plane, its amplitude in the back lobe is more than that for the square ground plane. As the size increases, the edge diffractions do not introduce any noticeable ripples in the forward region, and the diffraction level in the back region becomes very comparable to the noise level in the detection system. The periodicity of the

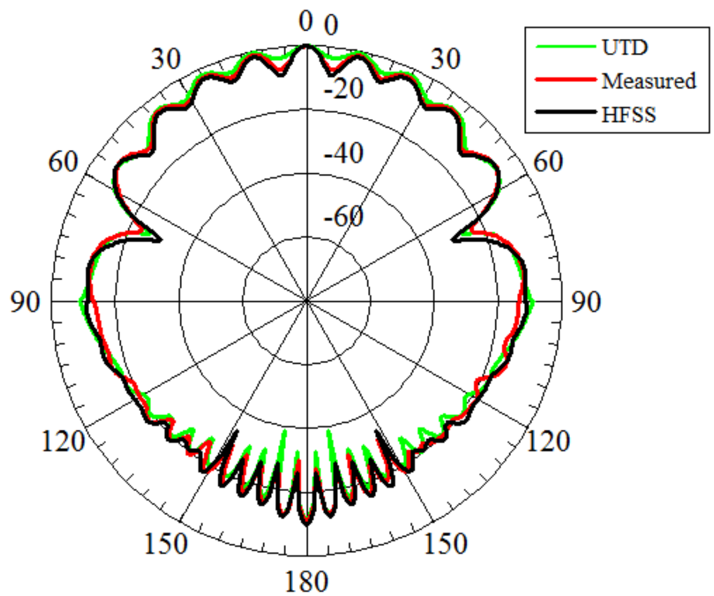

Fig. 4.5. Far-Zone E-Plane Amplitude Patterns of a Circular Waveguide Antenna Mounted on a Coated Circular Ground Plane at 10 GHz ($a = 0.397\lambda$, $2d = 10.16\lambda$).

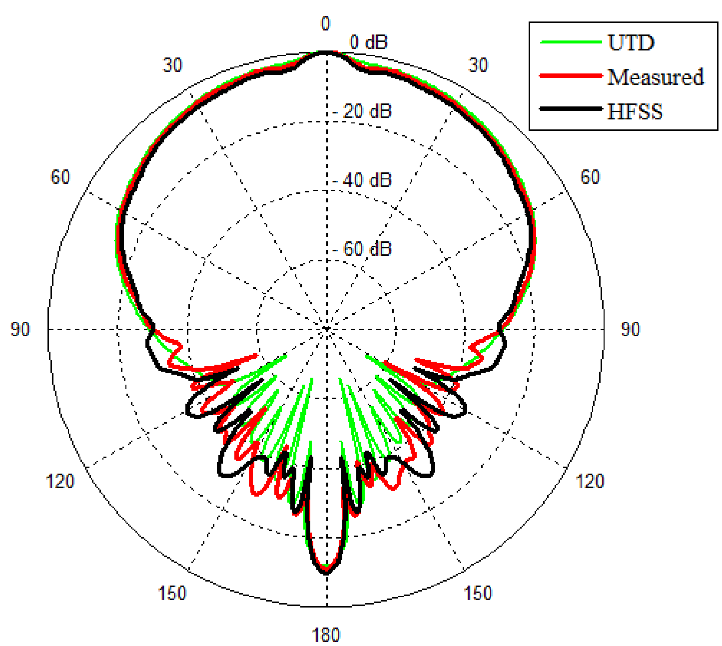

Fig. 4.6. Far-Zone H-Plane Amplitude Patterns of a Circular Waveguide Antenna Mounted on a Coated Circular Ground Plane at 10 GHz ($a = 0.397\lambda$, $2d = 10.16\lambda$).

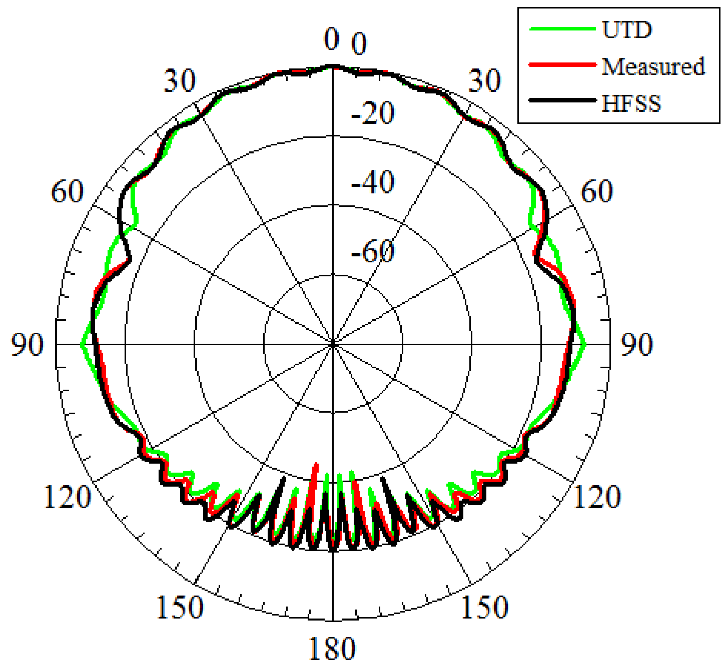

Fig. 4.7. Far-Zone E-Plane Amplitude Patterns of a Circular Waveguide Antenna Mounted on a Coated Square Ground Plane at 10 GHz ($a = 0.397\lambda$, $2d = 10.16\lambda$).

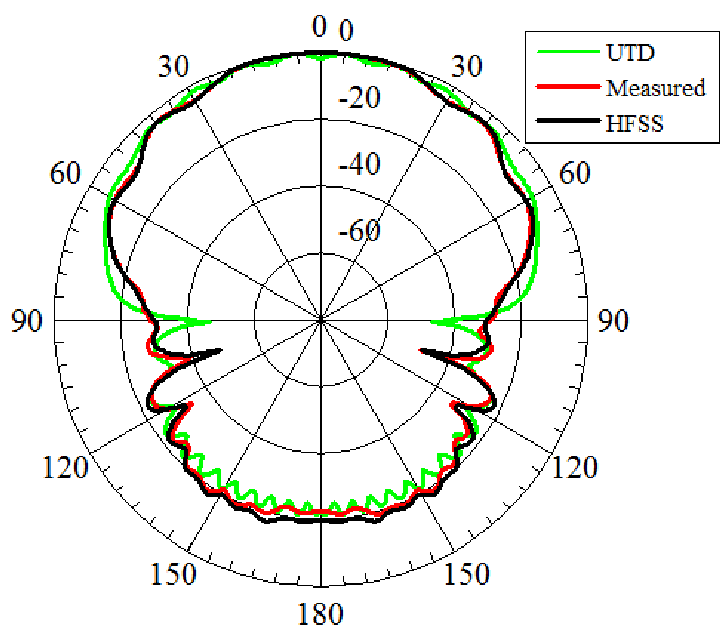

Fig. 4.8. Far-Zone H-plane Amplitude Patterns of a Circular Waveguide Antenna Mounted on a Coated Square Ground Plane at 10 GHz ($a = 0.397\lambda$, $2d = 10.16\lambda$).

ripples in the patterns depends upon the size of the ground plane, while the amplitude of the ripples depends upon the strength of the edge excitation.

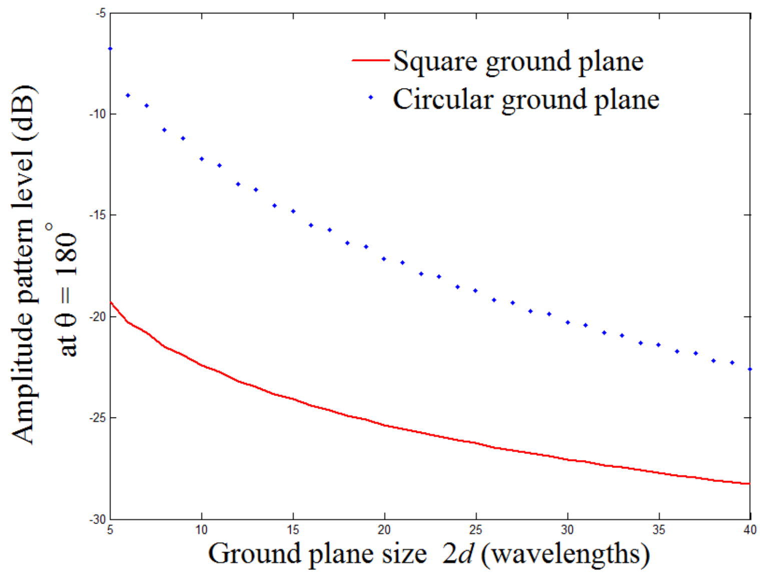

Fig. 4.9. Impact of the Ground Plane Size on the Amplitude Pattern Level at $\theta = 180°$.

The amplitude pattern level at $\theta = 180°$ for different coating thickness is also displayed in Fig. 4.10 for circular and square coated ground planes. It is apparent that the back lobe radiation at $\theta = 180°$ is stronger for thinner coatings. As shown in Fig. 4.11, by increasing the relative permittivity of the coating, the amplitude level of the diffracted field at $\theta = 180°$ decreases for both geometries. Based on the simulated data, increasing either the thickness or relative permittivity of the dielectric coating leads to less radiation in the back lobe region.

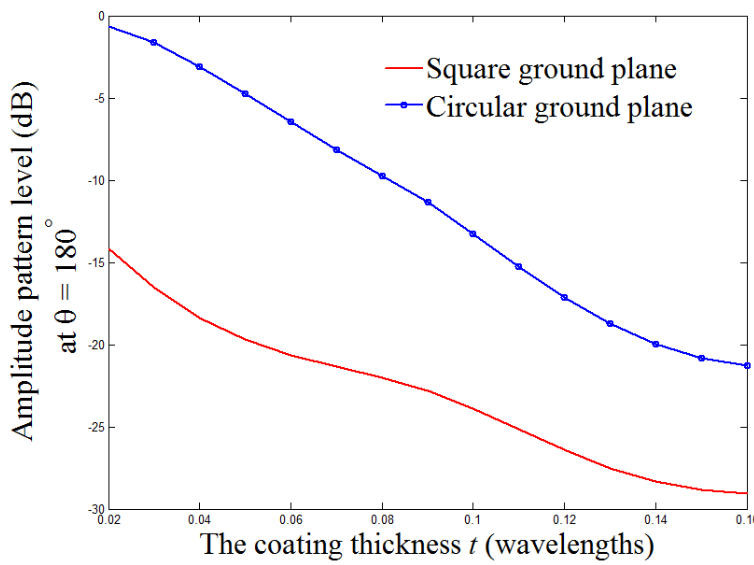

Fig. 4.10. Amplitude Pattern Level at $\theta = 180^\circ$ Due to the Coating Thickness.

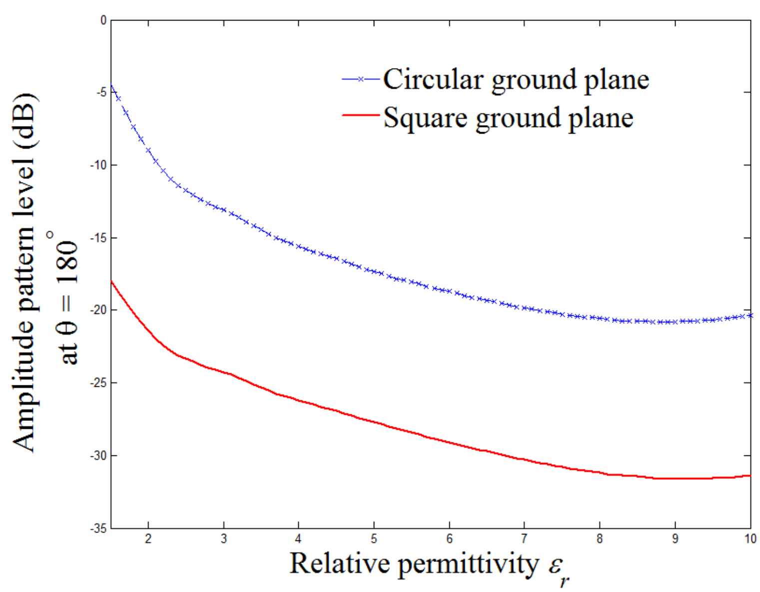

Fig. 4.11. Amplitude Pattern Level at $\theta = 180^\circ$ Due to the Relative Permittivity of the Dielectric Layer.

CHAPTER 5

MALIUZHINETS FUNCTION AND ITS PROPERTIES

The Maliuzhinets function (MF) has been used for the diffraction of waves by a wedge with different face surface impedances. For a wedge with an arbitrary angle, the Maliuzhinets function is cumbersome to compute, which is a major limitation of the application of rigorous theory of diffraction in the electromagnetic scattering by an impedance wedge. In this chapter, an exact closed-form solution is obtained to evaluate a known integral representation of the MF. The *tanh-sinh quadrature* rule is employed to successfully calculate the integral in the Maliuzhinets function, and the highly accurate numerical computation for $\Psi_n(z)$ is obtained over the entire complex z plane and for all n. For special wedge angles, the exact formulation is numerically verified by comparing it with the results obtained by numerical integration of the Maliuzhinets function.

5.1. Introduction

Maliuzhinets was the first who applied the Sommerfeld integral technique to the diffraction by an impedance wedge. In [55], Maliuzhinets derived a solution (in integral form) for the diffraction problem of waves by a wedge with different face impedances; therefore, the MF is pivotal in the theory of diffraction [11]. With increasing interest in how the material properties of a wedge impact its scattering, the diffraction coefficients for imperfectly conducting wedges have to be applied and MFs have to be computed. Because of its complexity, it is desirable (if not essential) to be able to compute the Maliuzhinets function in a simple and computationally efficient manner. However, for only two special cases, $n = 0.5$ and $n = 1.5$, the MF can be represented in a simple closed-form [55]. Also, the integral in the MF for $n = 1$ and $n = 2$ can be simplified [55].

Because of the significance of the scattering from the impedance $(n=1)$ and $(n=2)$ planes for many applications, the half- and full-plane Maliuzhinets functions $[\Psi_1(z), \Psi_2(z)]$ have been paid attention to and studied extensively [61]. Both functions are related to each other, so $\Psi_1(z)$ can be expressed in terms of $\Psi_2(z)$ as follows:

$$\Psi_2(z) = \sqrt{\frac{\sqrt{2}\cos(\frac{z}{2})+1}{\sqrt{2}+1}}\frac{1}{\sqrt[8]{\cos z}}\ \exp\Big[-\frac{1}{4\pi}\int_0^z \frac{s}{\cos s}\ ds\Big] \tag{5.1}$$

$$\Psi_1(z) = \sqrt[4]{\cos z}\ \exp\Big[\frac{1}{2\pi}\int_0^z \frac{s}{\cos s}\ ds\Big] \tag{5.2}$$

Comparing (5.2) with (5.1), $\Psi_1(z)$ can be expressed, in terms of $\Psi_2(z)$, as

$$\Psi_1(z) = \frac{\sqrt{2}\cos\frac{z}{2}+1}{\sqrt{2}+1}\frac{1}{\Psi_2^2(z)} \tag{5.3}$$

The Maliuzhinets functions above can be represented exactly if the integral of $\int_0^z \frac{s}{\cos(s)}\ ds$ is analytically evaluated. In [61] the exact closed forms of the Maliuzhinets functions in terms of the dilogarithem function, for the two cases of $n=2$ and $n=1$, have been evaluated and they are, respectively, given by

$$\Psi_2(z) = \frac{e^{\frac{c}{2\pi}}}{\sqrt[8]{\cos z}}\sqrt{\frac{\sqrt{2}\cos(\frac{z}{2})+1}{\sqrt{2}+1}}\Big[-j\tan\Big(\frac{z}{2}+\frac{\pi}{4}\Big)\Big]^{-\frac{z}{4\pi}}\exp\left(-j\frac{Li_2(-je^{jz})-Li_2(je^{jz})}{4\pi}\right) \tag{5.4}$$

$$\Psi_1(z) = e^{-\frac{c}{\pi}}\sqrt[4]{\cos z}\Big[-j\tan\Big(\frac{z}{2}+\frac{\pi}{4}\Big)\Big]^{-\frac{z}{2\pi}}\exp\left(-j\frac{Li_2(-je^{jz})-Li_2(je^{jz})}{2\pi}\right) \tag{5.5}$$

where $Li_2(z)$ is the dilogarithm function defined as $Li_2(z) = \sum_{k=1}^{\infty}\frac{z^k}{k^2}$ and $C \approx 0.916$ is the Catalan constant. Based on the comparisons between these formulations of (5.4) and (5.5) and the numerical solutions of (5.1) and (5.2) for the MFs, the accuracy of the closed-form expressions is verified and the discrepancies are negligible ($< 10^{-14}$).

In [62], approximate formulas for the Maliuzhinets function of a real argument are derived using the modified Chepyshev polynomials for different wedge angles. The coefficients of the Chepyshev polynomials are tabulated in [62]. Although the expressions are only derived for real arguments, they may still be accurate for a restricted range of complex arguments with small imaginary parts. An empirical formula for arbitrary wedge angles is also obtained using the same technique.

Volakis and Senior [63] derived a simple approximation for the half-plane Maliuzhinets function $\left[\Psi_2(z)\right]$ which is used only in the strip $0 \leq \mathrm{Re}(z) \leq \pi/2$ and $\mathrm{Im}(z) \geq 0$. $\Psi_2(z)$ can be evaluated throughout the entire complex plane using the recurrence relations that relate $\Psi_2(z)$ to its value at the corresponding point within the strip. For $0 \leq \mathrm{Re}(z) \leq \pi/2$ and $\mathrm{Im}(z) \leq 4.6$, $\Psi_2(z)$ is expressed as

$$\Psi_2(z) \cong 1 - 0.0139\ z^2 \tag{5.6}$$

and for $0 \leq \mathrm{Re}(z) \leq \pi/2$ and $\mathrm{Im}(z) \geq 4.6$, it is represented by

$$\Psi_2(z) \cong 1.05302\ \sqrt{\cos[0.25(z - j\ln 2)]}\ \exp\left(\frac{jz}{2\pi} e^{jz}\right) \tag{5.7}$$

In [64], approximate analytical expressions were derived for exterior wedge angles ($1 \leq n \leq 2$). For small arguments $0 \leq \mathrm{Re}(z) \leq \pi/2$ and $\mathrm{Im}(z) \leq 4$, $\Psi_n(z)$ is approximated by

$$\Psi_n(z) \cong 1 - z^2 \left(\frac{\delta}{\Phi^2}\right) \tag{5.8}$$

with

$$\delta = 0.04626 + 0.054\Phi - 0.0078\Phi^2 \tag{5.9}$$

$$\Phi = \frac{n\pi}{2} \tag{5.10}$$

For the large argument, $0 \leq \mathrm{Re}(z) \leq \pi/2$ and $\mathrm{Im}(z) \geq 4$, it is given by

$$\Psi_n(z) \cong \sqrt{\cos\left(\frac{z}{2n}\right)} \exp\left(-\frac{\gamma}{\pi}\right) \tag{5.11}$$

where

$$\gamma = 2.556343\Phi - 3.259678\Phi^2 + 1.659306\Phi^3 - 0.3883548\Phi^4 + 0.03473964\Phi^5 \tag{5.12}$$

Andrey Osipov [65] has used the simplest approximation using a single cosine function to evaluate the Maliuzhinets function, which is given by

$$\Psi_n(z) = \left[\cos\left(\frac{vz}{2+v}\right)\right]^{\frac{2+v}{4}} \tag{5.13}$$

where $v = 1/n$

This expression is only valid for $0.5 \leq n \leq 2$. The error of the approximation is less than 6% over the entire complex plane ($z - plane$).

Although several researchers have constructed approximate solutions of the Maliuzhinets function for certain wedge angles and/or restricted real or complex values of the argument (z), an accurate and efficient numerical computation of the MF over the entire complex z plane for an arbitrary wedge angle is desirable. The objective of this work is to obtain such a closed-form expression for the Maliuzhinets function where the *tanh-sinh quadrature* transformation is used to calculate the integral in the MF. The sections that follow are devoted to briefly review the Maliuzhinets function and its properties, and then discuss the numerical technique used to compute the integral of the MF.

5.2. Maliuzhinets Function

The Maliuzhinets function is a meromorphic function of a complex argument defined by many equivalent forms [54], [55]. One of them is the product form given by

$$\Psi_n(z) = \prod_{l=1}^{\infty}\prod_{m=1}^{\infty}\left[1-\left(\frac{z}{n\pi(2l-1)+\frac{\pi}{2}(2m-1)}\right)^2\right]^{(-1)^{m+1}} \tag{5.14}$$

and the double-integral formula is given by

$$\Psi_n(z) = \exp\left[-j\frac{1}{4n\pi}\int_{-j\infty}^{+j\infty}\int_{0}^{z}\tan\left(\frac{v}{2n}\right)\frac{1}{\cos(v-u)}\,du\,dv\right] \tag{5.15}$$

Performing integration on z, an alternate expression for the MF is

$$\Psi_n(z) = \exp\left[-\frac{1}{2}\int_0^{\infty}\frac{\cosh(zs)-1}{s\cosh(\frac{\pi}{2}s)\sinh(n\pi s)}\,ds\right] \tag{5.16}$$

where $z = x + jy$ and n is the wedge parameter $(0 < n \leq 2)$. An exterior wedge has values of n in the range of $1 \leq n \leq 2$, while for an interior wedge $0 < n < 1$.

The last expression (5.16) converges if $|\operatorname{Re}(z)| < \frac{\pi}{2} + 2n$ and hence the MF is regular in this strip; it can be used to determine values outside the strip by suitable recurrence relations. Some of these relations of the MF are summarized in [55]. The MF is an even function of its argument and conjugating the MF is equivalent to the MF of the conjugate of the argument and represented by:

$$\Psi_n(z) = \Psi_n(-z) \tag{5.17}$$

$$\Psi_n(z)^* = \Psi_n(z^*) \tag{5.18}$$

By using the recurrence equations, the MF can be determined for any z outside the strip by

$$\frac{\Psi_n(z+n\pi)}{\Psi_n(z-n\pi)} = \cot\left(\frac{z}{2}+\frac{\pi}{4}\right) \tag{5.19}$$

$$\Psi_n(z) = \Psi_n^2(0.5\pi)\ \frac{\cos\left(\frac{z-0.5\pi}{2n}\right)}{\Psi_n(z-\pi)} \tag{5.20}$$

$$\Psi_n\left(z+\frac{n\pi}{2}\right)\Psi_n\left(z-\frac{n\pi}{2}\right) = \Psi_n^2\left(\frac{n\pi}{2}\right)\Psi_{\frac{n}{2}}(z) \tag{5.21}$$

Equation 5.16, together with the recurrence relations of (5.19)-(5.21), implies that the $\Psi_n(z)$ can be found for any complex value of z when it is known in the strip $0 \leq \mathrm{Re}(z) \leq \pi/2+n\pi$ and $\mathrm{Im}(z) \geq 0$.

There are four special wedge angles for which the MF can be expressed in a closed form or simplified integral form. These correspond to the interior 90° wedge ($n = 0.5$), the exterior 90° wedge ($n = 1.5$), the full-plane wedge ($n = 1$), and the half-plane wedge ($n = 2$) [55]. The explicit expressions for these special wedge angles are

$$\Psi_{0.5}(z) = \cos\left(\frac{z}{2}\right) \tag{5.22}$$

$$\Psi_{1.5}(z) = \frac{4\cos^2(\frac{z}{6})-1}{3\cos(\frac{z}{6})} \tag{5.23}$$

$$\Psi_1(z) = \exp\left[\frac{1}{4\pi}\int_0^z \frac{2s-\pi\sin s}{\cos s}\ ds\right] \tag{5.24}$$

$$\Psi_2(z) = \exp\left[\frac{1}{8\pi}\int_0^z \frac{-\pi\sin s+4\pi\cos\frac{\pi}{4}\sin\frac{s}{2}-2s}{\cos s}\ ds\right] \tag{5.25}$$

For some practical cases, the $|\mathrm{Im}(z)|$ is very large. Therefore the asymptotic formula of the MF is given by

$$\Psi_n(z) = \frac{1}{\sqrt{2}}\Psi_n\left(\frac{\pi}{2}\right)\exp\left(-j\frac{z}{4n}\ \mathrm{sign}(\mathrm{Im}(z))\right) \qquad |\mathrm{Im}(z)| >> 1 \tag{5.26}$$

In addition to the MF, there is another special monomorphic function referred to as the Auxiliary Maliuzhinets Function (AMF), which is applied to calculate the diffraction from the impedance wedge [11], [54]. MF and AMF are related to each other where the Auxiliary Maliuzhinets function can be written as a product of four Maliuzhinets functions with different arguments as follows:

$$\Psi(z) = \Psi_n\big(z + \frac{n\pi}{2} + \frac{\pi}{2} - \theta_0\big)\Psi_n\big(z + \frac{n\pi}{2} - \frac{\pi}{2} + \theta_0\big)$$
$$\Psi_n\big(z - \frac{n\pi}{2} - \frac{\pi}{2} - \theta_n\big)\Psi_n\big(z - \frac{n\pi}{2} + \frac{\pi}{2} + \theta_n\big) \tag{5.27}$$

where θ_0 and θ_n are the surface impedance Brewster angles of the 0 and n face, respectively.

In the practical cases of ideal boundaries, the AMF expression can be simplified. For a perfectly conducting wedge and hard polarization, the Brewster angles vanish ($\theta_0 = \theta_n = 0$). Then (5.27) reduces to

$$\Psi(z) = \frac{1}{2}\Psi_n^4\left(\frac{\pi}{2}\right)\cos\left(\frac{z}{n}\right) \tag{5.28}$$

In the case of soft polarization, a perfectly conducting wedge implies $\theta_0 = \theta_n = \pi/2 - j\infty$, and the asymptotic formula of the AMF is given by

$$\Psi(z) = \frac{1}{4}\Psi_n^4\left(\frac{\pi}{2}\right)\exp\left(\frac{1}{2n}\big(|\mathrm{Im}(\theta_0)| + |\mathrm{Im}(\theta_n)|\big)\right) \tag{5.29}$$

In our work, for the soft polarization, the imaginary part of the argument of the MF or AMF goes to infinity. Therefore the previous asymptotic formulas need to be used.

Figs. 5.1 and 5.2 show the 3-D plots of the magnitude and phase of $\Psi_n(z)$ with $n = 1.65$ and varied values of the real x and imaginary y parts of the complex argument $z = x + jy$.

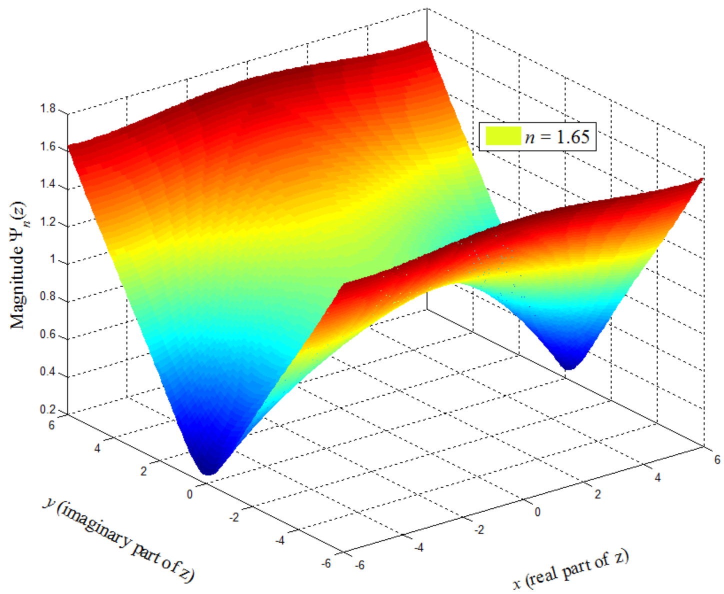

Fig. 5.1. Three-Dimensional Plot of the Magnitude of $\Psi_{1.65}(z)$ with Varied Values of x and y $(-6 \le x, y \le 6)$.

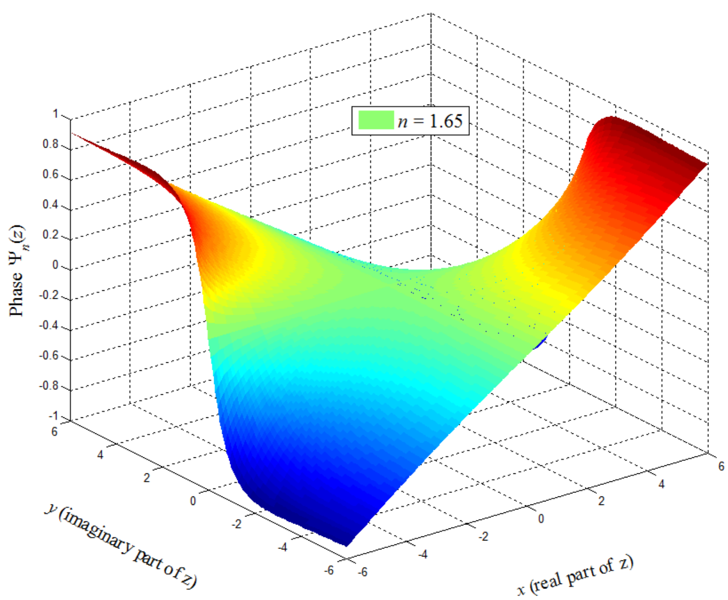

Fig. 5.2. Three-Dimensional Plot of the Phase of $\Psi_{1.65}(z)$ with Varied Values of x and y $(-6 \le x, y \le 6)$.

5.3. Tanh-Sinh Quadrature Rule

The *tanh-sinh quadratic* scheme is based on the Euler-Maclaurin formula, where an integral with a bell-shaped integrand, vanishing at the end points, can be approximated with high accuracy by using the trapezoidal rule with an equal mesh size. Consider the evaluation of the following integral

$$I = \int_{-1}^{1} f(t)\ dt \tag{5.30}$$

By changing variables $[t = g(x)]$ and then using the standard *trapezoidal rule* when the integrand is defined on the interval $(-\infty, \infty)$, the definite integral is approximated by [66]

$$\int_{-1}^{1} f(t)\ dt = \int_{-\infty}^{\infty} f\left[g(x)\right]\ g'(x)\ dx \approx h \sum_{m=-N}^{N} f\left[g(mh)\right]\ g'(mh) \tag{5.31}$$

where $g(x)$ is any continuous increasing function mapping $(-1,1)$ into $(-\infty,\infty)$, $h > 0$ is the grid spacing, and N is chosen sufficiently large that $\left|f\left[g(mh)\right]\ g'(mh)\right| < \varepsilon$ for $|m| > N$. With a suitable choice of $g(x)$, the $g'(x)$ factor will decrease rapidly as $x \longrightarrow \pm\infty$. If $g'(x)$ has zeros in the region of the singularities of $g(x)$, these singularities are cancelled out from the new integrand $[f[g(x)] \cdot g'(x)]$. To satisfy this condition, the *tanh-sinh quadrature* (*doubly-exponential*) transformation [67] is used

$$g(x) = \tanh\left[\frac{\pi}{2}\sinh(x)\right] \tag{5.32}$$

with

$$g'(x) = \frac{\pi \cosh(x)}{2\cosh^2\left[\frac{\pi}{2}\sinh(x)\right]} \tag{5.33}$$

It is obvious that $g(x)$ has the property that $g(x) \longrightarrow \pm 1$ as $x \longrightarrow \pm\infty$, as shown in Fig. 5.3. This property is useful to shrink the integrand to a certain region of space. Therefore, more accurate and efficient evaluation will be obtained.

Before the *tanh-sinh quadrature* rule is applied, the Maliuzhinets function needs to be transformed to an integral of the appropriate form in order to use this technique.

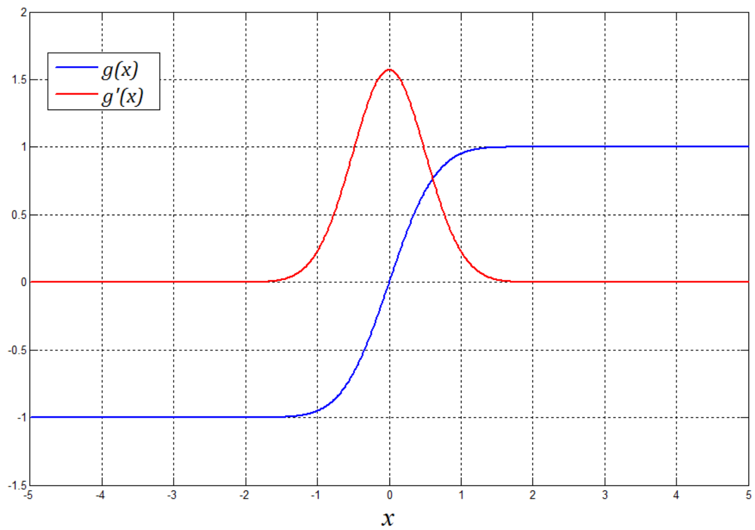

Fig. 5.3. $g(x)$ and its Derivative.

By mapping the integral from $(0,\infty)$ into $(0,1)$ in (5.16) and by using the symmetry property, the Maliuzhinets function is given by

$$\Psi_n(z) = \exp\left(-\frac{1}{4}\int_{-1}^{1} f(n,z,s)\, ds\right) \tag{5.34}$$

where

$$f(n,z,s) = \frac{\cosh(zs)-1}{s\cosh(\frac{\pi}{2}s)\sinh(n\pi s)} + \frac{\cosh(\frac{z}{s})-1}{s\cosh(\frac{\pi}{2s})\sinh(\frac{n\pi}{s})} \tag{5.35}$$

Now the solution of the Maliuzhinets function is obtained using (5.34) and the closed-form formula of the integral as follows:

$$\int_{-1}^{1} f(n,z,s)\,ds \approx h \sum_{m=-N}^{N} f\Big(n,z,\tanh\Big[\frac{\pi}{2}\sinh(mh)\Big]\Big) \cdot \frac{\pi\cosh(mh)}{2\cosh^2\big[\frac{\pi}{2}\sinh(mh)\big]} \tag{5.36}$$

$$\Psi_n(z) \approx \exp\left(-\frac{h}{4} \sum_{m=-N}^{N} f\Big(n,z,\tanh\Big[\frac{\pi}{2}\sinh(mh)\Big]\Big) \cdot \frac{\pi\cosh(mh)}{2\cosh^2\big[\frac{\pi}{2}\sinh(mh)\big]} \right) \tag{5.37}$$

The number of points in (5.37) is essentially infinite so that the summation has to be truncated at appropriate upper values of m. In this case N represents the maximum number of points at which $f[x,z,g(x)]$ of (5.37) is evaluated.

To verify the obtained closed-form expression of (5.37) for the MF, $\Psi_n(z)$ is plotted in Figs. 5.4-5.6, as a function of the imaginary part y of the argument, for three real part x values of z ($x = 0.5$, 1, and 1.5). The values of the MF of $n = 0.5, 1.5$ for the complex variable z were calculated and compared with the exact solution given by (5.22) and (5.23), respectively. For $n = 1$, the calculated values of the MF, based on the closed-form expression, were compared with the numerical solution of (5.24). For all the cases examined, excellent agreement between the closed-form expression of (5.37) and numerical solution is indicated with high accuracy.

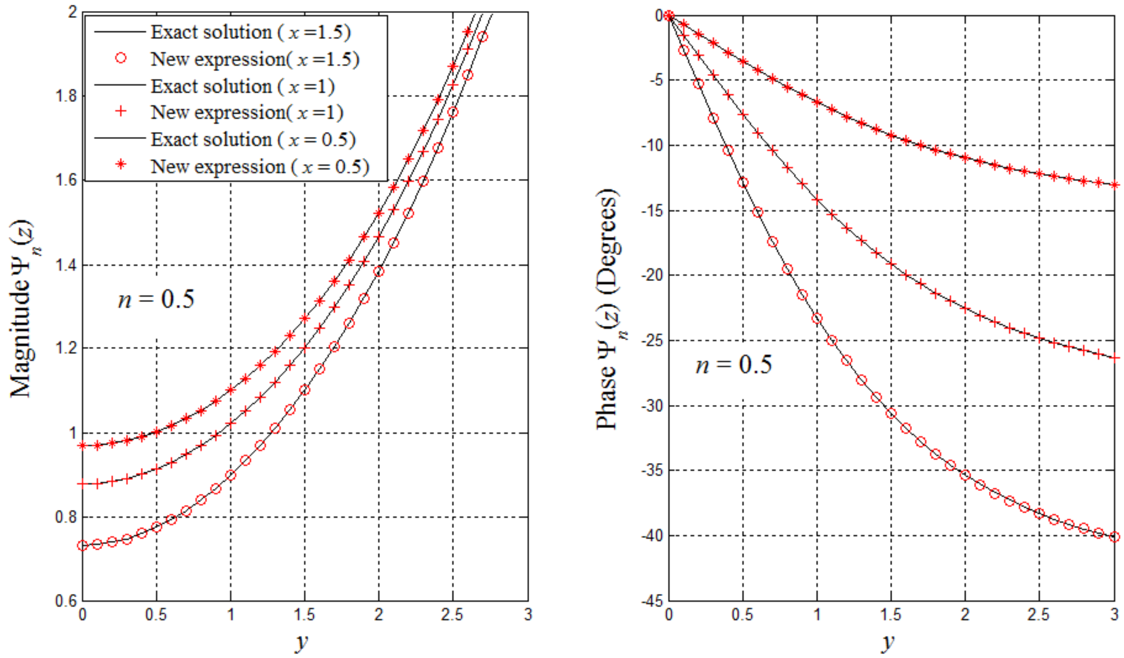

Fig. 5.4. Comparison of the Magnitude and Phase of $\Psi_{0.5}(z)$ with the Exact Values for Fixed Values of x While the Imaginary Part of z is Varied.

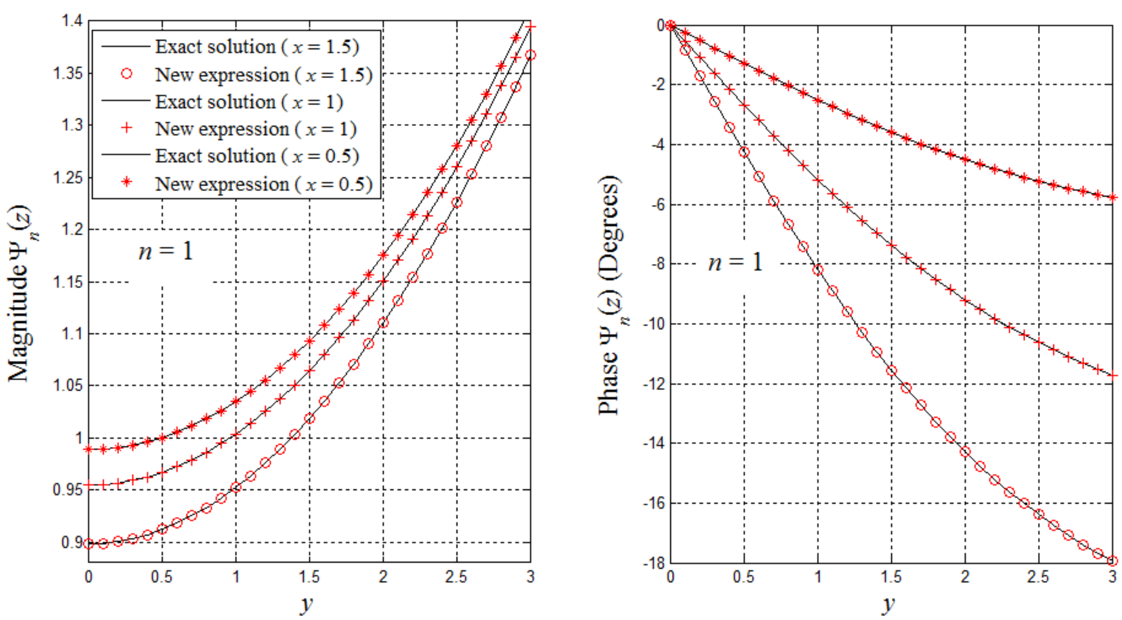

Fig. 5.5. Comparison of the Magnitude and Phase of $\Psi_1(z)$ with the Numerical Integration for Fixed Values of x While the Imaginary Part of z is Varied.

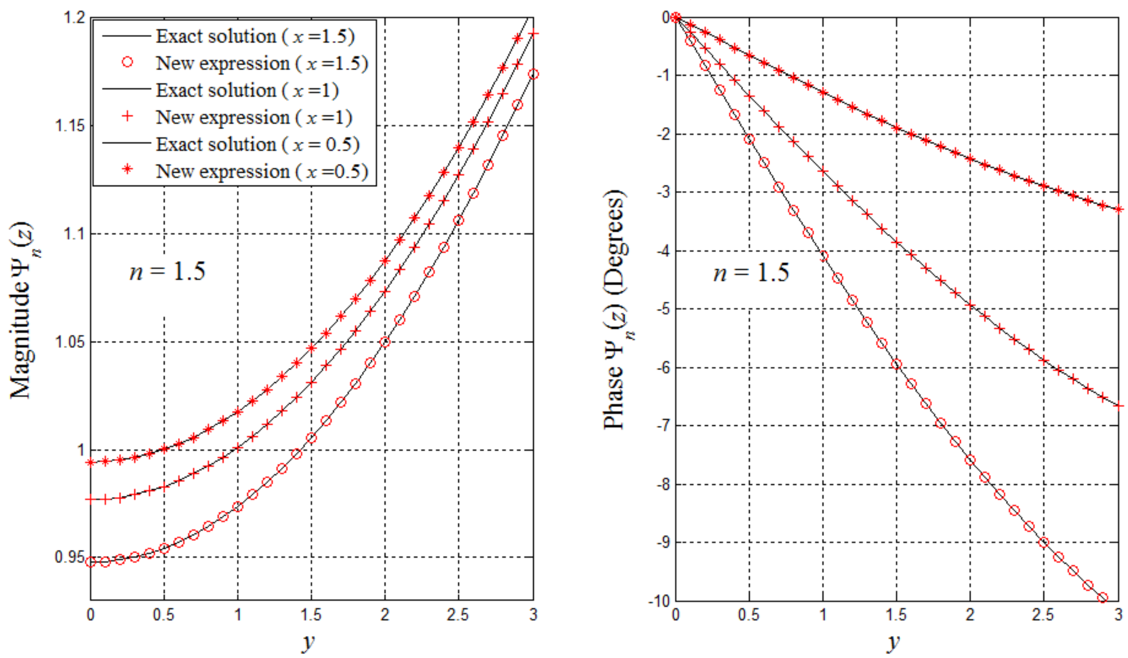

Fig. 5.6. Comparison of the Magnitude and Phase of $\Psi_{1.5}(z)$ with the Exact Values for Fixed Values of x While the Imaginary Part of z is Varied.

CHAPTER 6

CONCLUSIONS AND RECOMMENDATIONS

6.1. Conclusions

In this work, new expressions for the loss factor and gain of conical horn antennas have been developed based on the spherical aperture phase distribution of the fields over the horn aperture. The gain of a conical horn antenna, using the spherical instead of the quadratic aperture phase distribution, is:

- Mainly the same for large axial length horns $(L > 60\lambda)$ or small peak aperture phase errors $(S < 0.4\lambda)$.
- Considerably higher, by as much as 0.84 dB, for intermediate axial length horns $(10\lambda < L < 20\lambda)$ and intermediate peak aperture phase errors $(0.4\lambda < S < 0.9\lambda)$.
- Higher for large values of the peak aperture phase errors $(S > 0.9\lambda)$.

Also, improved formulas for the design of optimum gain horn antennas are proposed. These formulas do not approximate the path length term, and thus they give more accurate horn dimensions for a given optimum gain. The new formulas are highly useful for the design of conical horns because they reduce the computational time significantly. Based on the design equations, the optimum axial lengths and diameters (in wavelengths) obtained by using spherical aperture phase distributions are in good agreement with those obtained using quadratic aperture phase distributions when the optimum gain is equal to or larger than 20 dB. However, the spherical and quadratic aperture phase distributions result in different optimum axial lengths when the gain is less than about 20 dB.

The aperture edge of a conical horn antenna without a ground plane, is a factor that impacts the radiation patterns in the diffraction zone. This effect has been examined both analytically and experimentally. Two commercial conical horns were chosen for this investigation. The study indicates that the aperture edge does not affect significantly the pattern at the forward region. Its main impact appears in the far side lobes and back lobe. It was also shown that to correct the axial caustic, UTD equivalent currents can be used with good agreement between experiment, simulation, and theory for a range of angles. In the diffraction modeling of the horn using the UTD, the feeding and supporting structures were not taken into account due to their complex geometries. However, these structures significantly distort the pattern, especially in the back region. Including these structures in the UTD modeling is not an easy task, and they create more computational problems and deficiencies which cannot easily be simulated with UTD. However, very good agreement was attained between the measurements and HFSS simulations which incorporated these complex structures. This demonstrates that the back feeding and supporting structures are responsible for the deviations between the measurements and UTD results.

For X- and C-band conical horn and circular waveguide antennas mounted on finite PEC ground planes, the edges of the finite ground planes influence the amplitude patterns. Two ground planes, square and circular, were selected to be examined. The study indicates that the ground plane edge diffractions do impact the main forward lobe pattern, especially in the E plane. Its primary impact appears in the far side lobes and back lobe region. The aperture integration method, augmented by the UTD diffraction, for the prediction of aperture antenna radiation was implemented. The UTD edge diffractions are included for the finite ground plane in both the E- and H-plane predictions. In the E plane, single edge diffractions plus the direct GO field contribute to the total field. In the H plane, the total field consists of the direct GO field, single edge diffractions, slope diffracted field, and E-plane edge equivalent current field. In addition, the contributions of the electric and magnetic equivalent currents must be included for the circular ground plane to correct the caustic created by the diffracted fields at and near the axis of the antenna. The numerical results obtained are compared with measured data and those simulated by Ansofts High Frequency Structure Simulator (HFSS). The measured and simulated results indicate that the theoretical predictions, for both circular and square ground planes, are in very good agreement. This work demonstrates that the finite edge effect must be included in the calculation to obtain very accurate results of the radiation patterns, especially for extended dynamic ranges.

For aperture antennas mounted on finite coated square and circular PEC ground planes, good agreement is obtained between the analytical, experimental, and HFSS-simulated amplitude patterns in the E and H planes. All these results are indicators that the extended uniform theory of diffraction is a useful tool to calculate the amplitude patterns of a circular aperture antenna mounted on coated ground planes, square and circular. In addition, the contributions of the electric and magnetic equivalent currents must be included for the circular coated ground plane to correct the caustics created by the diffracted fields at and near the axis of the antenna.

The radiation amplitude in the back region of the aperture antenna mounted on coated ground planes depends significantly on the size of the ground plane where the amplitude pattern level at $\theta = 180^\circ$ decreases monotonically with increasing the ground plane size for both geometries, circular and square. Based on the simulated data, by increasing either the thickness or relative permittivity of the dielectric coating, the amplitude level of the diffracted field at $\theta = 180^\circ$ decreases for both geometries.

For uncoated and coated cases, the H-plane electric field component of the incident field vanishes along the ground plane edge (grazing incidence). Thus, only diffraction by the E-plane edges contributes significantly to the E- and H-plane diffraction patterns. To obtain the far-zone E-plane amplitude pattern, only the diffraction from the midpoints of the E-plane edge contributes to the amplitude pattern. For the far-zone H-plane amplitude pattern, diffraction accruing at all points along the E-plane edge, non-normal and normal incidence of the incident GO fields at the edge, must be taken into consideration. The discrepancies between the theoretical and measured results in the backward region of the far-zone E- and H-plane amplitude patterns can be attributed to the inability of the diffraction techniques to accurately model the structure feeding the aperture antennas as well as the supporting structure.

Although the side of the square is equal to the diameter of the circular, the E- and H-plane amplitude patterns of the circular ground plane are greater than those of the square ground plane at and near the antenna axis $(\theta = 180^\circ)$ due to the ring radiator.

Finally, an exact closed-form solution of the Maliuzhinets Function (MF) is obtained. The $tanh - sinh\ quadrature$ rule is employed to successfully calculate the integral in the Maliuzhinets function, and the highly accurate numerical computation for MF is obtained over the entire complex z plane and for all n.

6.2. Recommendations

The work in this dissertation has focused on circular aperture antennas. The study methodology is general and can be applied to other antenna configurations, such as rectangular aperture antennas, probe-excited circular or rectangular cavity-backed slot antennas, either uncoated or coated.

This study may easily be extended to find the radiation characteristics (radiation patterns, edge diffractions, and mutual coupling) for aperture arrays mounted on finite uncoated or coated ground planes.

This research project is limited in its investigation to a single dielectric coating. In many applications, multilayer dielectric covers are used as superstrates to increase the antenna directivity, either for a single element or an array. Therefore, multilayer dielectric diffractions must be introduced to predict the radiation characteristics of the antenna such as amplitude patterns.

The results produced by the analytical model here are predicated assuming that the aperture antenna is excited by a single TE_{11} mode. In practice, circular horn antennas with high efficiency and low cross polarization can be realized by introducing multiple modes. Also, for rectangular horn antennas, a circularly-polarized elliptical-shaped beam can be generated if the antenna is designed to support only the TE_{10} and TE_{01} modes. Extending the theory to account for multi-mode excitation would be a straight-forward task, although more complicated and advanced computations are needed.

To a large extent, improving system performance and satisfying system requirements need microstrip antennas with low profile, weight, and cost. In addition, they need to be easily integrable into arrays or with microwave integrated circuits. Microstrip antennas satisfies above all aspects can be conformed to any shape. All of these aspects drive the development of microstrip antenna systems. Therefore, microstrip antennas have found many applications in both the military and the civil sectors, such as aircraft, radar, communications, navigation, landing systems, missile radar, telemetry, satellite communication, direct broadcast TV, remote sensing radar, radiometer, ship communication, land vehicles, mobile satellite telephone, mobile radio, and biomedical systems. There are several microstrip configurations like the square, rectangular, circular, elliptical, triangular, rectangular dipole, circular ring, and ring sector. In general, each one has different radiation characteristics and uses. Because patch antennas consist of a substrate and a finite ground plane, the impact of these factors, represented by impedance surfaces, surface waves, and edge diffractions, can be examined using the uniform theory of diffraction of the impedance wedge. In addition, by optimizing the coating thickness and the relative permittivity of the substrate, the edge diffractions, especially in the back region, can be reduced.

REFERENCES

[1] C. A. Balanis, *"Antenna Theory: Analysis and Design,"* 3^{rd} edition, NJ: John Wiley & Sons, 2005.

[2] A. P. King, "The radiation characteristics of conical horn antennas," *Proc. of the IRE*, vol. 38, no. 3, pp. 249 – 251, 1950.

[3] J. L. Volakis, *"Antenna Engineering Handbook,"* 4^{th} edition, NY: McGraw-Hill, 2007.

[4] J. D. Kraus and R. J. Marhefka, *"Antennas for all Applications,"* 3^{rd} edition, NY: McGraw-Hill, 2002.

[5] C. Y. Tan and K. T. Selvan, "An improved approximate formula for conical horn," *Microwave and Optical Technology Letters*, vol. 49, no. 33, pp. 971 – 973, 2007

[6] E. I. Muehldorf, "The phase center of horn antennas," *IEEE Trans. Antennas Propagat.*, vol. 18, no. 6, pp. 753 – 760, 1970.

[7] K. Lui, C. A. Balanis, C. R. Birtcher, and G. C. Barber, "Analysis of pyramidal horn antennas using moment methods," *IEEE Trans. Antennas Propagat.*, vol. 41, no. 10, pp. 1379 – 1389, 1993.

[8] K. B. Baltzis, "Theoretical establishment and evaluation of a novel optimal pyramidal horn design criterion," *Progress In Electromagnetics Research*, vol. 108, pp. 361 – 383, 2010.

[9] M. J. Maybell and P. S. Simon, "Pyramidal horn gain calculation with improved accuracy," *IEEE Trans. Antennas Propagat.*, vol. 41, no. 7, pp. 884 – 889, 1993.

[10] R. F. Harrington, *"Time-Harmonic Electromagnetic Fields,"* 1^{st} edition, NY: McGraw-Hill, NY, 1961.

[11] C. A. Balanis, *"Advanced Engineering Electromagnetics,"* 2^{nd} edition, NJ: John Wiley & Sons, 2012.

[12] A. C. Durgun and M. Kuzuoḡlu, “Computation of physical optics integral by Levin’s integration algorithm,” *Progress in Electromagnetics Research M.*, vol. 6, pp. 59 – 74, 2009.

[13] D. Levin, “Procedures for computing one- and two-dimensinal integrals of functions with rapid irregular oscillations,” *Mathematics of Computation.*, vol. 38, no. 158, pp. 531 – 538, 1982.

[14] D. Levin, “Analysis of a collocation method for integrating rapily oscillatory functions,” *J. Comput. Appl. Math.*, vol. 78, pp. 131–138, 1996.

[15] A. W. Love, *“Electromagnetic Horn Antennas,”* NY: IEEE Press, 1976.

[16] Y. T. Lo and S.W. Lee, *“Antenna Handbook: Theory, Applications, and Design,”* NY: IEEE Press, 1988.

[17] J. B. Keller, “Diffraction by an aperture,” *J. Appl. Phys.*, vol. 28, no. 4, pp. 426 – 444, 1957.

[18] J. B. Keller, “Geometrical theory of diffraction,” *J. Opt. Soc. Amer.*, vol. 52, no. 2, pp. 116 – 130, 1962.

[19] R. G. Kouyoumjian, “Asympotic high-frequency methods,” *Proceedings of the IEEE*, vol. 53, pp. 864 – 876, 1965.

[20] P. H. Pathak and R. G. Kouyoumjian, “The dyadic diffraction coefficient for a perfectly conducting wedge,” Technical Report 2183-4 (AFCRL-69-0546), Ohio State University ElectroScince Lab., 1970.

[21] P. H. Pathak and R. G. Kouyoumjian, “An analysis of the radiation from apertures on curved surfaces by the geometrical theory of diffraction,” *Proceedings of the IEEE*, vol. 62, no. 11, pp. 1438 – 1447, 1974.

[22] R. G. Kouyoumjian and P. H. Pathak, “A uniform geometrical theory of diffraction for an edge in a perfectly conducting surface,” *Proceedings of the IEEE*, vol. 62, no. 11, pp. 1448 – 1461, 1974.

[23] G. L. James, *"Geometrical Theory of Diffraction for Electromagnetic Waves,"* 3rd edition, London: Peter Peregrinus Ltd., 1986.

[24] M. Abramowitz and I. A. Stegun, *"Handbook of Mathematical Functions: with Formulas, Graphs, and Mathematical Tables"* 1st edition, NY: Dover Publications, 1965.

[25] H. M. Ibrahim and D. T. Stephenson, "Radiation patterns of a $\lambda/4$ monopole mounted on thick finite square and circular ground planes," *INT. J. Electronics*, vol. 64, no. 3, pp. 345 - 358, 1988.

[26] J. Huang, "The finite ground plane effect on the microstrip antenna radiation patterns," *IEEE Trans. Antennas Propagat.*, vol. 31, no. 4, pp. 649-653, 1983.

[27] A. G. Derneryd, "Linearly polarized microstrip antennas," *IEEE Trans. Antennas Propagat.*, vol. AP-24, no. 6, pp. 846 - 850, 1976.

[28] A. G. Derneryd and A. G. Land "Extended analysis of rectangular microstrip resonator antenna," *IEEE Trans. Antennas Propagat.*, vol. AP-27, no. 6, pp. 846 - 849, 1979.

[29] C. A. Balanis, "Radiation from conical surfaces used for high-speed spacecraft," *Radio Science.*, vol. 7, no. 2, pp. 339 - 343, 1972.

[30] M. S. Narasimhan and M. S. Sheshadri, "GTD analysis of the radiation patterns of conical horns," *Proceedings of the IEEE*, vol. 26, no. 6, pp. 774 – 778, 1978.

[31] M. S. Narasimhan and K. S. Rao, "GTD analysis of the near-field patterns of conical and corrugated conical horns," *Proceedings of the IEEE*, vol. 27, no. 5, pp. 705 – 708, 1979.

[32] C. Ryan and L. Peters, "Evaluation of edge-diffracted fields including equivalent currents for the caustic regions," *IEEE Trans. Antennas Propagat.*, vol. 17, no. 3, pp. 292 - 298, 1969.

[33] A. k. Bhattacharyya and D. L. Sengupta, *"Radar Cross Section Analysis and Control"* 3rd edition, MA: Artech House, 1991.

[34] M. D. Deshpande and P. D. Prabhakar, “Analysis of dielectric covered infinite array of rectangular microstrip antennas,” *IEEE Trans. Antennas Propagat.*, vol. 35, no. 6, pp. 732 - 736, 1987.

[35] L. Shafai, “Radiation from an axial slot antenna coated with a homogeneous material,” *Canadian J. Phys.*, vol. 50, pp. 23 – 27, 1972.

[36] X. B. Wu and W. Ren, “Axial slot antenna on an anisotropic dielectric-coated circular cylinder,” *IEE Proceeding Microwave Antennas Propagation*, vol. 141, no. 6, pp. 527 – 530, 1994.

[37] J. H. Richmond and M. C. Gilreath, “Flush-mounted dielectric-loaded axial slot on circular cylinder,” *IEEE Trans. Antennas Propagat.*, vol. AP-23, no. 3, pp. 348 – 351, 1975.

[38] T. M. Smith and K. E. Golden, “Radiation patterns from a slotted cylinder surrounded by a plasma sheath,” *IEEE Trans. Antennas Propagat.*, pp. 775 – 780, 1965.

[39] J. Chalupa, “Asymptotic surface field of slot antenna on coated cylindrical conductor,” *IEEE Trans. Antennas Propagat.*, vol. 25, no. 24, pp. 1657 – 1659, 1989.

[40] H. A. Ragheb and E. E. Hassan, “Radiation characteristic of slots on conducting circular cylinder covered by eccentric dielectric cylinder,” *IEE Proceeding Microwave Antenna Propagation*, vol. 142, no. 2, pp. 168 – 172, 1995.

[41] O. Aydin and A. Hizal, “Radiation characteristics of slot excited cylindrical antenna coated by layered anisotropic material,” *IEEE, MELECON ’96, 8th Mediterranean*, vol. 3, pp. 1404 – 1406, 1996.

[42] M. A. Mushref, “TM Radiation from an eccentric dielectric coated cylinder with two axial slots,” *Journal of Electromagnetic Waves and Applications*, vol. 19, no. 5, pp. 577 – 590, 2005.

[43] T. Hinata and H. Hosono, “Scattering of electromagnetic waves by an axially slotted conducting elliptic cylinder,” *MMET’96 Proceedings, Ukraine*, pp. 28 – 31, 1996.

[44] M. I. Hussein and A. K. Hamid, "Radiation by axial slot elliptical antenna coated by a lossy dielectric material," *IEEE International Symposium on Electromagnetic Compatibility, EMC'03, Istanbul*, pp. 146 – 149, 2003.

[45] J. H. Richmond, "Axial slot antenna on dielectric-coated elliptic cylinder," *IEEE Trans. Antennas Propagat.*, vol. 37, no. 10, pp. 1235 – 1241, 1989.

[46] M. Hussein, A. Sebak, and M. Hamid, "Scattering and coupling properties of a slotted elliptic cylinder," *IEEE Transaction on Electromagnetic Compatibility*, vol. 36, no. 1, pp. 76 – 81, 1994.

[47] H. A. Ragheb, A. Sebak, and L. Shafai, "Radiation by axial slots on a dielectric-coated nonconfocal conducting elliptic cylinder," *IEE Proc. Microwave Antennas Propagation*, vol. 143, no 2, pp. 124 – 130, 1996.

[48] M. I. Hussein and A. K. Hamid, "Radiation characteristics of JV axial slot antenna on a lossy dielectric-coated elliptic cylinder," *Can. J. Phys.*, 82, pp. 141 – 149, 2004.

[49] MC. M. Knop and G. I. Cohn, "Radiation from an aperture in a coated plane," *Radio Sci. J. Res.*, vol. 68D, no. 4, pp. 363 - 378, 1964.

[50] J. R. Wait and W. E. Mientka, "Calculated patterns of slotted elliptic-cylinder antennas," *Appl Sci. Res.*, vol. 7, no. 1, pp. 449 - 462, 1959.

[51] M. A. Leontovich, "Approximate boundary conditions for the electromagnetic field on the surface of a good conductor, *Investigation of Propagation of Radio Waves*, Part III," *Academy of Sciences*, pp. 5 - 12, Moscow, 1948.

[52] T. B. A. Senior and J. L. Volakis, "Approximate boundary conditions in electromagnetics," *IEEE Press*, U.K., 1995.

[53] R. E. Collin, *"Foundations for Microwave Engineering"* 2^{nd} edition, NY: McGraw-Hill, 1992.

[54] T. Griesser, High-frequency electromagnetic scattering from imperfectly conducting structures, Ph.D. dissertation, Arizona State University, Tempe, 1988.

[55] G. D. Maliuzhinets, “Excitation, reflection, and emission of surface waves from a wedge with given faces impedances,” *Sov. Phys. Doke.*, vol. 3, pp. 752 – 755, 1958.

[56] J. L. Volakis, “A uniform geometrical theory of diffraction for an imperfectly conducting half-plane,” *IEEE Trans. Antennas Propagat.*, vol. 34, no. 2, pp. 172 - 180, 1986.

[57] T. B. A. Senior and J. L. Volakis, “Scattering by an imperfect right-angled wedge,” *IEEE Trans. Antennas Propagat.*, vol. 34, no. 5, pp. 681 - 689, 1986.

[58] R. G. Rojas, “Electromagnetic diffraction of an obliquely incident plane wave field by a wedge with impedance faces,” *IEEE Trans. Antennas Propagat.*, vol. 36, no. 7, pp. 956 - 970, 1988.

[59] T. B. A. Senior, “Solution for a class of imperfect wedge problems for skew incidence,” *Rad. Soc.*, vol. 21, pp. 185-191, 1986.

[60] R. Tiberio, G. Pelosi, and G. Manara, “A uniform GTD formulation for the diffraction by a wedge with impedance faces,” *IEEE Trans. Antennas Propagat.*, vol. 33, no. 8, pp. 867 - 873, 1985.

[61] S. Koh and Y. Lee, “Exact evaluation of the Maliuzhinets half-plane function,” *IEEE Trans. Antennas Propagat.*, vol. 55, no. 2, pp. 483 - 485, 2007.

[62] K. Hongo and E. Nakajima, “Polynomial approximation of Maliuzhinets’ function,” *IEEE Trans. Antennas Propagat.*, vol. 34, no. 7, pp. 942 – 947, 1986.

[63] J. Volakis and T. Senior, “Simple expressions for a function occuring in diffraction theory,” *IEEE Trans. Antennas Propagat.*, vol. 33, no. 6, pp. 678 – 680, 1985.

[64] M. Herman, J. Volakis, and T. Senior, “Analytic expressions for a function occuring in diffraction theory,” *IEEE Trans. Antennas Propagat.*, vol. 35, no. 9, pp. 1083 - 1086, 1987.

[65] Andrey V. Osipov, “A simple approximation of the Maliuzhinets function for describing wedge diffraction,” *IEEE Trans. Antennas Propagat.*, vol. 53, no. 8, pp. 2773 - 2776, 2005.

[66] V. Aihie and G. Evans, "The tanh transformation for double integrals with singularities-a progressive rule," *J. Comp. Appl. Maths.*, vol. 24, pp. 349 – 354, 1988.

[67] M. Mori, "Quadrature formulas obtained by variable transformation and the DE-rule," *J. Comp. Appl. Maths.*, vol. 12, pp. 119 – 130, 1985.